

# **Fourier Transform Heterodyne Spectroscopy of Liquid Interfaces**

A thesis presented

by

**Doo Soo Chung**

to

The Department of Chemical Physics

in partial fulfillment of the requirements

for the degree of

Doctor of Philosophy

in the subject of

Chemical Physics

Harvard University

Cambridge, Massachusetts

January, 1991

## Abstract

This thesis describes the application of a novel Fourier transform heterodyne spectroscopy technique with an ultrahigh resolution of  $200 \mu\text{Hz}$  to the study of capillary waves at liquid-vapor interfaces. The apparatus uses a frequency-shifted local oscillator to separate signals from counter-propagating capillary waves of identical frequency. The main beam and local oscillator are aligned in such a way as to select capillary waves of a given, continuously adjustable frequency.

This capability to separate counter-propagating waves was used to study the spectral asymmetry of light scattered from capillary waves at a nonequilibrium water surface in the presence of a temperature gradient. The observed asymmetries agree, in sign and order of magnitude, with the one predicted by linearized fluctuating hydrodynamics. This apparatus was also used to measure the spatial damping coefficients of capillary waves at a clean water surface and a water surface covered with a monolayer of pentadecanoic acid. For these measurements a double-beam heterodyne technique, which requires no calibration or deconvolution of instrumental functions, was used. The spatial damping coefficient of a clean water is in good agreement with the hydrodynamics theory. A sharp maximum in the spatial damping was observed at the end of the coexistence region of two phases of the pentadecanoic acid monolayer.

# Contents

<b>Abstract</b>	<b>i</b>
<b>Table of Contents</b>	<b>ii</b>
<b>1 Introduction</b>	<b>1</b>
1.1 Light-beating spectroscopy	1
1.2 Spectral asymmetry of nonequilibrium interfacial fluctuations	3
1.3 Viscoelastic properties of fluid interfaces	3
1.4 Organization of this thesis	5
<b>2 Fourier Transform Heterodyne Spectroscopy</b>	<b>7</b>
2.1 Optical correlations and hydrodynamic fluctuations	7
2.1.1 Measurement of light intensity	7
2.1.2 Measurement of the frequency spectrum	9
2.1.3 Light scattering and spectral resolution	11
2.1.4 Heterodyne detection	14
2.2 Surface light scattering technique	18
2.3 Experimental limits of Fourier transform heterodyne spectroscopy	24
2.3.1 Instrumental resolution	24
2.3.2 Free spectral range	29
2.4 Applications of Fourier transform heterodyne spectroscopy	30
2.4.1 Separation of counter-propagating capillary waves	30
2.4.2 Epitaxial crystal-growth speed measurements	34
<b>3 Viscoelastic Properties and Hydrodynamic Fluctuations of Fluid</b>	

<b>Interfaces</b>	<b>40</b>
3.1 Rheology of interfaces	41
3.2 Interfacial boundary conditions	44
3.3 Interfacial waves	49
3.4 Power spectrum of interfacial waves	53
3.5 Appendix	61
3.5.1 Viscoelasticity; a combination of elasticity and viscosity	61
3.5.2 Viscoelastic moduli of an interface	63
<b>4 Spectral Asymmetry of the Light Scattered from a Nonequilibrium Liquid Interface</b>	<b>66</b>
4.1 Basic considerations	67
4.2 Fluctuating hydrodynamic theory	69
4.3 Experimental	76
4.4 Results and discussion	83
<b>5 Damping of Capillary Waves</b>	<b>87</b>
5.1 Damping measurements of capillary waves	88
5.2 Spatial damping of induced waves	90
5.2.1 Basic considerations	90
5.2.2 Double-beam heterodyne measurements of spatial damping	94
5.2.3 Static light scattering measurements of spatial damping	98
5.3 Experimental	99
5.4 Results and Discussion	106
5.4.1 Clean water surface	106
5.4.2 Monolayer-covered water surface	108
<b>Bibliography</b>	<b>115</b>
<b>Acknowledgments</b>	<b>122</b>

# Chapter I

## Introduction

### §1.1 Light-beating spectroscopy

In many experiments one is interested in the difference of a certain physical quantity from a reference value. For an accurate measurement it is essential to have a stable reference. When it is not possible to measure a certain quantity directly or to have a reliable reference one may still be able to perform accurate *differential* measurements. For example if one is interested in measuring the small frequency shift of an electromagnetic wave due to a scattering process, one must either measure, to a very high degree of accuracy, the frequencies of each of the incident and scattered waves to determine the frequency difference, or one can measure directly the beat frequency of the two waves. In the second method the frequencies of the two waves are automatically compared. In addition, differential measurements do not require as high a relative accuracy as absolute measurements, and the stability of the reference (the incident electromagnetic wave) is unimportant.

Radio frequency technology is a notable example of a field where the advantages of differential measurements have been extensively applied. In optics, a beating technique was first demonstrated in the classic Zeeman splitting experiment of Forrester *et al.* in 1955 using a mercury lamp as a light source [Forrester, Gudmundsen *et al.* 1955]. With the advent of lasers, light-beating spectroscopy has become an important tool to measure optical

lineshapes and frequency shifts with a resolution on the order of several hertz [Cummins and Swinney 1970]. The technique was first used for the study of the output of lasers by monitoring intermode beats [Forrester 1961]. Today beating spectroscopy is an invaluable tool in many fields including quasi-elastic light scattering studies of macromolecules and critical phenomena of fluids [Benedek 1968], surface wave light scattering studies of the viscoelastic properties of fluid interfaces [Loudon 1984], and velocimetry of fluids [Yeh and Cummins 1964; Chu 1974]. Since this thesis deals with light scattering from interfacial fluctuations in fluids, we will start by reviewing previous work in this area.

The first attempts at measuring the capillary wave<sup>†</sup> spectra of methanol and isopropanol were made by Katyl and Ingard using a Fabry-Pérot interferometer as a scanning optical filter [Katyl and Ingard 1967]. Since the resolution of the interferometer was too low to resolve the capillary wave peaks, only a broadening of the incident light spectrum was observed. One year later Katyl and Ingard were able to observe the capillary wave peaks of methanol using light-beating spectroscopy [Katyl and Ingard 1968]. At the same time Bouchiat *et al.* measured the capillary wave spectra of ether and glycerine using a light-beating technique. They also determined the dispersion relation for capillary waves [Bouchiat and Meunier 1968; Bouchiat, Meunier *et al.* 1968]. From then on light-beating spectroscopy has been widely used to study capillary waves on a great variety of fluid interfaces. Currently the main application of light-beating technique is the measurement of the viscoelastic properties of bulk fluids and interfaces. The technique is especially useful for the measurements of very low interfacial tension ( $10^{-3} - 10^{-6}$  dyne/cm) of, for example, oil/water interfaces where conventional mechanical methods do not work well [Pouchelon, Meunier *et al.* 1980ab].

---

<sup>†</sup> Capillary waves (ripples or riplons) are short-wavelength surface waves of liquids with the surface tension acting as the dominant restoring force [Landau and Lifshitz 1959].

## **§1.2 Spectral asymmetry of nonequilibrium interfacial fluctuations**

Microscopic fluctuations of macroscopic variables play an important role in many physical phenomena both in and out of equilibrium. For more than a century, equilibrium fluctuations in systems ranging from simple molecular fluids to complex biological solutions have been studied both theoretically and experimentally [Berne and Pecora 1976]. In the past two decades there has been much interest in nonequilibrium steady state fluctuations [Physics Today 1984; Groot and Mazur 1984]. For nonequilibrium bulk fluids, a number of theoretical predictions [Ronis, Procaccia *et al.* 1979; Zwan, Bedeaux *et al.* 1981; Kirkpatrick, Cohen *et al.* 1982; Fox 1982] were confirmed experimentally using laser light scattering. In particular, asymmetries in the spectra of the scattered light were found to be in agreement with theory [Beysens, Garrabos *et al.* 1980; Kiefte, Clouter *et al.* 1984; Law, Gammon *et al.* 1988]. On the other hand, little work has been done on interfaces out of equilibrium in spite of the large interest in interfacial phenomena. The main theoretical difficulty is the lack of translational symmetry across the interface.

Recently, it has been predicted that an asymmetry should also occur in the spectrum of the light scattered from capillary waves on a fluid interface in the presence of a small temperature gradient [Grant and Desai 1983; Desai and Grant 1986]. Experimental verification requires high resolution and separation of down-shifted and up-shifted capillary wave peaks [Mazur and Chung 1987]. Measurements confirming the existence of the predicted asymmetry [Chung, Lee *et al.* 1988; Chung, Lee *et al.* 1990] are presented in this thesis.

## **§1.3 Viscoelastic properties of fluid interfaces**

In spite of the microscopic nature of an interface, its properties can influence the macroscopic behavior of bulk phases. Many of the phenomena controlled by interfacial properties have important applications in industry and technology, for example, foam and

emulsion stability, thin liquid film and flow stability [Lucassen 1981]. Another example of the importance of interfacial properties is the wetting of liquid droplets on a solid surface, a phenomenon which is determined by the interfacial tensions of the solid/vapor, solid/liquid and liquid/vapor interfaces. This macroscopic behavior of a bulk liquid can be controlled by changing the interfacial tensions of the liquid with minute amounts of surfactants (surface active substances). A well-known example from antiquity [Tabor 1980] is that a rough sea can be calmed by pouring a small quantity of oil on the surface of the sea. This calming effect of oil was studied by Benjamin Franklin in the eighteenth century [Franklin 1774] and has aroused much scientific and public interest ever since. It was found that a thin layer of oil could smooth the surface of the sea by suppressing the generation and increasing the damping of the small (capillary) ripples. The viscoelastic properties of the interface, especially, gradients in interfacial tension, caused by variations in surfactant concentration due to local contractions and expansions during wave passage, are responsible for the smoothing effect of oil. This effect has been utilized in modern astronomy [Lemonick 1986]: ripples on a perfect 1-m parabolic mirror, obtained by slowly rotating a pool of liquid mercury, are suppressed by coating the mercury surface with oil. To quote a review paper on this phenomenon, it is rather surprising that ‘even today there is neither an adequate explanation [of how this increased damping of ripples affects the large waves on a sea] nor even a widespread appreciation among scientists of what has and has not been established’ [Scott 1978].

Recently, light-beating techniques have been applied to study the viscoelastic properties of fluid interfaces covered with surfactant monolayers [Earnshaw 1983; Earnshaw, McGivern et al. 1990; Earnshaw, McGivern et al. 1988; Thominet, Stenvot et al. 1988]. So far the success of such measurements has been limited by a number of technical problems. This thesis presents a *differential* approach to measuring the spatial damping of capillary waves that circumvents most of these problems.

## **§1.4 Organization of this thesis**

In this thesis two experiments on the light scattering from liquid interfaces are presented. Before the experimental part of this thesis, Fourier transform heterodyne spectroscopy (FTHS) and the hydrodynamic theory of liquid interfaces are described.

Chapter 2 describes FTHS in general. In the first section, pre-detection and post-detection filtering methods are compared. In particular, the advantage of heterodyne detection using a frequency-shifted local oscillator is discussed. Then the experimental setup of FTHS is described and the ultimate instrumental resolution of FTHS is considered. In the last section, separation of counter-propagating capillary waves and a measurement of the epitaxial crystal-growth speed of an amorphous/crystalline silicon interface are given as demonstration of the directional sensitivity and high resolution of our apparatus, respectively.

Chapter 3 considers the hydrodynamic theory of fluid interfaces. First, the ‘equivalent interface’ model is introduced to simplify the description of an interface, and the boundary conditions which are satisfied by fluids and the equivalent interface are explained. Then a derivation of interfacial waves and the dispersion equation is given. In the last section, the power spectrum of thermal interfacial fluctuation is discussed.

Chapter 4 details the application of FTHS for measuring the spectral asymmetry of the light scattered from a nonequilibrium liquid interface in the presence of a small temperature gradient. In the first two sections, the spectral asymmetry is calculated using a simple mean free path argument and then by the generalized Langevin formalism of fluctuating hydrodynamics. Finally the experimental measurement of the spectral asymmetry and the discrepancies between theory and experiment are discussed.

Chapter 5 describes a double-beam FTHS applied to study the effect of surfactants on the spatial damping of capillary waves. The experimental aspects of the double-beam FTHS and its advantages over single-beam FTHS are discussed. Spatial damping

coefficients of capillary waves are measured on a water/nitrogen interface of pure water and one covered with a monolayer of pentadecanoic acid. The coincidence of a maximum spatial damping coefficient with the phase transition of the surfactant monolayer is discussed.

## Chapter II

### Fourier Transform Heterodyne Spectroscopy

#### §2.1 Optical correlations and hydrodynamic fluctuations

From a smooth and sharp interface between two media with different indices of refraction, a light beam is reflected and refracted. If the interface is rough, the incident light is scattered; if the roughness is moreover time-dependent, the scattered light has a different frequency spectrum from the incident light. Therefore, one can obtain information on the dynamics of an interface by analyzing the spectrum of the light scattered from the interface [Chu 1974; Berne and Pecora 1976]. In this section we will discuss the relationship between the interfacial fluctuations and the scattered light.

##### §2.1.1 Measurement of light intensity

Consider a spatially coherent<sup>†</sup> light field described by a real electric field  $E^R(t)$  of the form<sup>‡</sup>

$$E^R(t) = \sum_m A_m^R(t) \cos[\psi_m(t) - \omega_m t], \quad (2.1)$$

where  $A_m^R(t)$  is a slowly varying real amplitude, and  $\psi_m(t)$  is the phase of the field for a

---

<sup>†</sup> The position dependence of the field is suppressed. The effect of spatial incoherence is discussed in the reference [Cummins and Swinney 1970].

<sup>‡</sup> Note that even though in general the light field should be described quantum mechanically, it is sufficient here to treat it classically [Cummins and Swinney 1970; Pike and Jakeman 1974].

positive angular frequency  $\omega_m$ .<sup>†</sup> The associated complex electric field  $E(t)$  is [Born and Wolf 1975]

$$E(t) = \sum_m A_m(t) e^{-i\omega_m t}, \quad (2.2)$$

where

$$A_m(t) = A_m^R(t) e^{i\psi_m(t)}. \quad (2.3)$$

The field in Eq. (2.1) is the real part of the complex field in Eq. (2.2),

$$E^R(t) = \text{Re}\{E(t)\}. \quad (2.4)$$

The instantaneous intensity of the field  $E^R(t)$  is then given by the magnitude of the Poynting vector

$$I(t) = c\epsilon E^R(t)^2, \quad (2.5)$$

with  $c$  the speed of light and  $\epsilon$  the permittivity of the medium. The intensity measured by a detector is a time-average over the detector response time  $\tau_d$

$$\overline{I(t)} \equiv \frac{1}{\tau_d} \int_{-\tau_d/2}^{\tau_d/2} I(t+\tau) d\tau. \quad (2.6)$$

In terms of the electric field,  $\overline{I(t)}$  is given by

$$\begin{aligned} \overline{I(t)} = c\epsilon \overline{E^R(t)^2} = \frac{c\epsilon}{4} \sum_{mn} \left\{ \overline{A_m(t)A_n(t)e^{-i(\omega_m+\omega_n)t}} \right. \\ \left. + \overline{A_m^*(t)A_n^*(t)e^{i(\omega_m+\omega_n)t}} + 2 \overline{A_m(t)A_n^*(t)e^{-i(\omega_m-\omega_n)t}} \right\}. \quad (2.7) \end{aligned}$$

If the detector response time is much longer than the period of the electric field, then

---

<sup>†</sup> Throughout this thesis we will use the frequency  $f$  and the corresponding angular frequency  $\omega = 2\pi f$  interchangeably depending on which quantity is more appropriate in the context.

$$\overline{e^{\pm i(\omega_m + \omega_n)t}} = \frac{\sin[(\omega_m + \omega_n)\tau_d/2]}{(\omega_m + \omega_n)\tau_d/2} e^{\pm i(\omega_m + \omega_n)t} \approx 0, \quad (2.8)$$

and the first and second terms in Eq. (2.7) can be neglected. Therefore, the average intensity is given in terms of the complex field by

$$\overline{I(t)} = \frac{c\mathcal{E}}{2} \overline{E^*(t)E(t)}. \quad (2.9)$$

Note the subtle difference between Eqs. (2.5) and (2.9). The latter is generally valid because detector response times far exceed the period of the optical field ( $\tau_d \geq 1 \times 10^{-9}$  s;  $2\pi\omega_m^{-1} \sim 1 \times 10^{-14}$  s).

### §2.1.2 Measurement of the frequency spectrum

Techniques for determining the frequency spectrum of scattered light fall into two categories [Brown 1983]: pre-detection and post-detection filtering (see Fig. 2.1). In the former case one first spectrally filters the incident light, for example with a spectrometer or an interferometer, and then measures the intensity transmitted by the filter. This yields the optical or first-order power spectrum of the scattered field  $E_s(t)$  [Born and Wolf 1975]

$$P^{(1)}(\omega) \equiv \lim_{T \rightarrow \infty} \frac{1}{2T} |E_s(\omega)|^2, \quad (2.10)$$

where  $T$  is the sampling time and

$$E_s(\omega) = \int_{-\infty}^{\infty} E_s(t) e^{i\omega t} dt, \quad (2.11)$$

is the Fourier amplitude of the electric field component with angular frequency  $\omega$ .

According to the Wiener-Khinchine theorem [Born and Wolf 1975] the first-order power spectrum  $P^{(1)}(\omega)$  is the Fourier transform of the first-order or *field* correlation function

$$P^{(1)}(\omega) = \int_{-\infty}^{\infty} G^{(1)}(\tau) e^{i\omega\tau} d\tau, \quad (2.12)$$

where the field correlation function is defined as

$$G^{(1)}(\tau) \equiv \lim_{T \rightarrow \infty} \frac{1}{2T} \int_{-T}^T E_s^*(t) E_s(t+\tau) dt = \langle E_s^*(0) E_s(\tau) \rangle. \quad (2.13)$$

In the above equation we have used the ergodic theorem to replace the time average by an ensemble average [Balescu 1975].

In post-detection filtering the total intensity is first detected and the detector signal  $j(t)$  is later filtered or processed to get the power spectrum of  $j(t)$

$$P_j(\omega) \equiv \lim_{T \rightarrow \infty} \frac{1}{2T} |j(\omega)|^2, \quad (2.14)$$

where  $j(\omega)$  is the Fourier transform of  $j(t)$ . Since the signal  $j(t)$  is a real quantity, one has

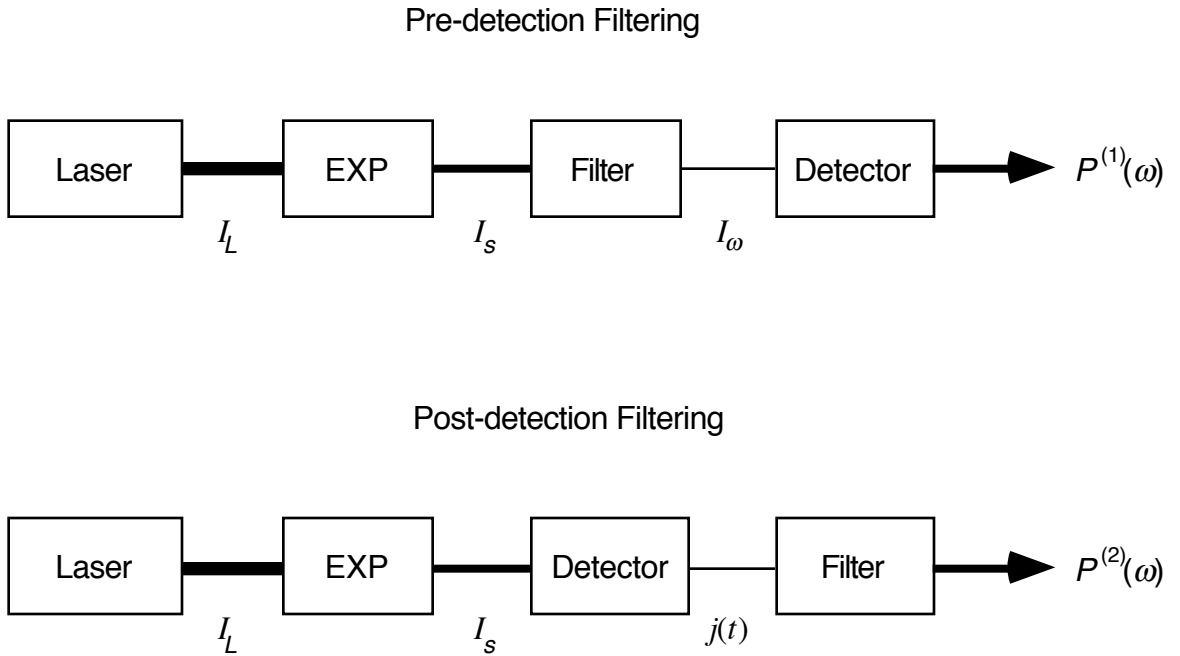


Fig. 2.1. Pre/Post-detection filtering.  $I_L$  and  $I_s$  are the intensities of the probing laser light and scattered signal, respectively;  $I_\omega$  is the output mean power at  $\omega$  with a bandwidth  $\Delta\omega$ ;  $j(t)$  is the detector current;  $P^{(1)}(\omega)$  and  $P^{(2)}(\omega)$  are the first- and second-order power spectrum, respectively.

$$P_j(\omega) = \lim_{T \rightarrow \infty} \frac{1}{2T} \int_{-\infty}^{\infty} j(t) e^{i\omega t} dt \int_{-\infty}^{\infty} j(t') e^{-i\omega t'} dt' = \int_{-\infty}^{\infty} \langle j(0)j(\tau) \rangle e^{i\omega\tau} d\tau. \quad (2.15)$$

which embodies the Wiener-Khintchine theorem. If the intensity of the light is large enough, the detector signal  $j(t)$  is continuous and proportional to the average intensity  $\overline{I(t)}$ . If shot noise resulting from the quantum mechanical aspect of the detection process is neglected, the detector signal correlation function  $\langle j(0)j(\tau) \rangle$  is then proportional to the *intensity* correlation function

$$G^{(2)}(\tau) \equiv \lim_{T \rightarrow \infty} \frac{1}{2T} \int_{-\tau}^{\tau} \overline{I(t) I(t+\tau)} dt = \langle \overline{I(0) I(\tau)} \rangle. \quad (2.16)$$

Using the Wiener-Khintchine theorem and defining a second-order power spectrum in analogy to Eq. (2.10) we get

$$P_j(\omega) \propto \int_{-\infty}^{\infty} G^{(2)}(\tau) e^{i\omega\tau} d\tau = \lim_{T \rightarrow \infty} \frac{1}{2T} |I(\omega)|^2 \equiv P^{(2)}(\omega). \quad (2.17)$$

In other words, the power spectrum of the detector signal is proportional to the second-order power spectrum of the light.

### §2.1.3 Light scattering and spectral resolution

To compare the two techniques mentioned above, let us now consider more explicitly the case of a laser light scattering experiment. The incident monochromatic laser field is of the form

$$E_L(t) = A_L e^{-i\omega_L t + i\psi(t)}, \quad (2.18)$$

with  $\omega_L$  the angular frequency of the light and  $\psi(t)$  a slowly varying random function representing fluctuations in the phase of the light. If fluctuations in a property  $H(\mathbf{r}, t)$  of the medium cause fluctuations in its electric susceptibility

$$\Delta\chi_{\mathbf{e}}(\mathbf{r},t) = \left( \frac{\partial\chi_e}{\partial H} \right) \Delta H(\mathbf{r},t), \quad (2.19)$$

then the light will be scattered. The scattered field can be written in the form

$$E_s(t) = h_{\mathbf{q}}(t) e^{-i\omega_L t + i\psi(t)}, \quad (2.20)$$

where  $h_{\mathbf{q}}(t)$  is a stochastic complex quantity proportional to the fluctuations in the electric susceptibility  $\Delta\chi_{\mathbf{e}\mathbf{q}}(t)$  [Chu 1974]

$$h_{\mathbf{q}}(t) \propto \Delta\chi_{\mathbf{e}\mathbf{q}}(t) = \left( \frac{\partial\chi_e}{\partial H} \right) \Delta H_{\mathbf{q}}(t), \quad (2.21)$$

with  $\Delta\chi_{\mathbf{e}\mathbf{q}}(t)$  and  $\Delta H_{\mathbf{q}}(t)$  the Fourier amplitudes of  $\Delta\chi_{\mathbf{e}}(\mathbf{r},t)$  and  $\Delta H(\mathbf{r},t)$  for a fluctuation of wavevector  $\mathbf{q}$ , respectively. In this thesis any quantity with a subscript ‘ $\mathbf{q}$ ’ denotes its Fourier amplitude of a complex Fourier series expansion. For a quantity  $B(\mathbf{r})$

$$B(\mathbf{r}) = \frac{1}{V} \sum_{\mathbf{q}} B_{\mathbf{q}} e^{i\mathbf{q}\cdot\mathbf{r}}, \quad (2.22)$$

where  $V$  the volume of the system and

$$B_{\mathbf{q}} \equiv \int_V B(\mathbf{r}) e^{-i\mathbf{q}\cdot\mathbf{r}} d\mathbf{r}, \quad (2.23)$$

is the Fourier amplitude. In the limit  $V \rightarrow \infty$ , we may write the Fourier transform pair [Bracewell 1965]

$$B(\mathbf{r}) = \int_{-\infty}^{\infty} B_{\mathbf{q}} e^{i\mathbf{q}\cdot\mathbf{r}} \frac{d\mathbf{q}}{(2\pi)^3}, \quad (2.24)$$

$$B_{\mathbf{q}} = \int_{-\infty}^{\infty} B(\mathbf{r}) e^{-i\mathbf{q}\cdot\mathbf{r}} d\mathbf{r}. \quad (2.25)$$

Substituting the expression for the scattered light Eqs. (2.20) and (2.21) into Eq. (2.13), one gets

$$G^{(1)}(\tau) = \langle E_s^*(0) E_s(\tau) \rangle \propto \langle \Delta H_{\mathbf{q}}^*(0) \Delta H_{\mathbf{q}}(\tau) \rangle \langle e^{-i\{\psi(0)-\psi(\tau)\}} \rangle e^{-i\omega_L \tau}, \quad (2.26)$$

where the correlation functions of  $\Delta H_{\mathbf{q}}(t)$  and  $e^{i\psi(t)}$  are separated since the laser source and the medium can be considered statistically independent of each other.<sup>†</sup> In pre-detection filtering the spectrum of the scattered light, which is the Fourier transform of  $G^{(1)}(\tau)$ , is therefore in part determined by the phase fluctuations in the incident field. This is equivalent to saying that whenever the spectral width of the incident field is larger than the width associated with the scattering process, the field correlation function of the scattered light and hence the optical power spectrum is dominated by the fluctuations in  $\psi(t)$ . Another limiting factor for the spectral resolution is the filtering process itself. To increase the frequency resolution, the passband width of the filter is narrowed and the signal intensity becomes correspondingly smaller. Thus the signal-to-noise ratio may limit the resolution even before the phase fluctuations play a role. In practice the limit of pre-detection filtering is on the order of a few MHz for interferometers [Demtröder 1982].

Let us next consider post-detection filtering. Scattered light is now detected directly and the temporal behavior of the signal, caused by the beating of various spectral components of the scattered light, is analyzed according to Eq. (2.15). This scheme is called self-beating or homodyne<sup>‡</sup> spectroscopy [Ford and Benedek 1965]. Substituting the expression of the scattered light Eqs. (2.20) and (2.21) into Eq. (2.16), one obtains the homodyne correlation function of the scattered light intensity  $I_s(t)$

---

<sup>†</sup> Consider a system having two independent parts, 1 and 2. Neglecting the interaction Hamiltonian between the two parts, we may write the Hamiltonian  $\mathcal{H}_t$  and the distribution function  $f_t$  of the entire system as

$$\mathcal{H}_t(\Gamma_1, \Gamma_2) = \mathcal{H}_1(\Gamma_1) + \mathcal{H}_2(\Gamma_2), \quad f_t(\Gamma_1, \Gamma_2) = f_1(\Gamma_1) f_2(\Gamma_2),$$

where  $\Gamma_1$  and  $\Gamma_2$  are the coordinates of the phase spaces for the two parts;  $f_1$  and  $f_2$  are the corresponding distribution functions. Thus the average of any product  $A(\Gamma_1)B(\Gamma_2)$  equals the product of the averages of  $A$  and  $B$ , since

$$\langle A(\Gamma_1)B(\Gamma_2) \rangle = \int A(\Gamma_1)B(\Gamma_2)f_t(\Gamma_1, \Gamma_2)d\Gamma_1d\Gamma_2 = \int A(\Gamma_1)f_1(\Gamma_1)d\Gamma_1 \int B(\Gamma_2)f_2(\Gamma_2)d\Gamma_2 = \langle A(\Gamma_1) \rangle \langle B(\Gamma_2) \rangle.$$

$$G_s^{(2)}(\tau) = \langle \overline{I_s(0)} \overline{I_s(\tau)} \rangle \propto \langle \overline{|\Delta H_{\mathbf{q}}(0)|^2} \overline{|\Delta H_{\mathbf{q}}(\tau)|^2} \rangle \quad (2.27)$$

which is independent of the phase of the incident light. If the fluctuation  $\Delta H_{\mathbf{q}}(t)$  is a Gaussian process [Mandel 1963], the homodyne correlation function is then related to the correlation function of  $\Delta H_{\mathbf{q}}(t)$  by

$$\langle \overline{|\Delta H_{\mathbf{q}}(0)|^2} \overline{|\Delta H_{\mathbf{q}}(\tau)|^2} \rangle = \langle \overline{|\Delta H_{\mathbf{q}}(0)|^2} \rangle^2 + \left| \langle \overline{\Delta H_{\mathbf{q}}(0)} \overline{\Delta H_{\mathbf{q}}(\tau)} \rangle \right|^2. \quad (2.28)$$

The first term on the right hand side gives rise to a delta function at zero frequency. When the correlation function  $\langle \overline{\Delta H_{\mathbf{q}}(0)} \overline{\Delta H_{\mathbf{q}}(\tau)} \rangle$  is a simple exponential, the homodyne correlation function  $G_s^{(2)}(\tau)$  is also a simple exponential and the power spectrum  $P_s^{(2)}(\omega)$ , which is the Fourier transform of  $G_s^{(2)}(\tau)$  (see Eq. 2.17), is a Lorentzian. For any other correlation function the power spectrum becomes very complex [Chu 1974].

Note that the phase fluctuations in the incident field cancel out in the second-order power spectrum of the scattered light. The ultimate resolution is determined neither by the spectral width of the incident light source nor by the passband width of a filter, but by the sampling time and the stability of the apparatus, which will be discussed in more detail in §2.3.

### §2.1.4 Heterodyne detection

Although the homodyne technique has a high resolution independent of the bandwidth of the light source, the intensity of the scattered light is often too small to overcome the detector noise. This problem can be solved, however, by combining the scattered light with a coherent local oscillator signal and detecting the beat between the two [Cummins and Swinney 1970]. In this heterodyne detection the mixing of the local

---

‡ There are some differences in the use of ‘homodyne’ and ‘heterodyne’ in the literature. Here, self-beating of the scattered light by itself is referred to as *homodyne* detection, while the mixing of scattered light signal with a separate local oscillator is called *heterodyne* detection.

oscillator allows one to increase the signal level sufficiently so that the detector noise is negligible [Jacobs 1988].

For a general description of the heterodyne detection scheme, consider a local oscillator field coherent with the incident laser field but frequency shifted by an amount  $\Delta\omega_{LO}^\dagger$

$$E_{LO}(t) = A_{LO} e^{-i(\omega_L + \Delta\omega_{LO})t + i\psi(t)}. \quad (2.29)$$

At the detector this field is combined with the scattered light,  $E_s$ , from Eq. (2.20). Following Eq. (2.9), the intensity at the detector is then given by

$$\begin{aligned} \overline{I(t)} &= \frac{c\mathcal{E}}{2} \overline{|E_s(t) + E_{LO}(t)|^2} \\ &= \overline{I_s(t)} + \overline{I_{LO}(t)} + \frac{c\mathcal{E}}{2} \left\{ \overline{E_s^*(t)E_{LO}(t)} + \overline{E_{LO}^*(t)E_s(t)} \right\}. \end{aligned} \quad (2.30)$$

The product  $\overline{I(0)} \overline{I(\tau)}$  has sixteen terms

$$\begin{aligned} \overline{I(0)} \overline{I(\tau)} &= \overline{I_s(0)} \overline{I_s(\tau)} + \overline{I_{LO}(0)} \overline{I_{LO}(\tau)} + \overline{I_s(0)} \overline{I_{LO}(\tau)} + \overline{I_{LO}(0)} \overline{I_s(\tau)} \\ &+ \frac{c^2\mathcal{E}^2}{4} \left\{ \overline{E_s^*(0)E_{LO}(0)} \overline{E_{LO}^*(\tau)E_s(\tau)} + \text{c.c.} \right\} \\ &+ \frac{c\mathcal{E}}{2} \left\{ \overline{I_s(0)} + \overline{I_{LO}(0)} \right\} \left\{ \overline{E_s^*(\tau)E_{LO}(\tau)} + \text{c.c.} \right\} \\ &+ \frac{c\mathcal{E}}{2} \left\{ \overline{E_s^*(0)E_{LO}(0)} + \text{c.c.} \right\} \left\{ \overline{I_s(\tau)} + \overline{I_{LO}(\tau)} \right\} \\ &+ \frac{c^2\mathcal{E}^2}{4} \left\{ \overline{E_s^*(0)E_{LO}(0)} \overline{E_s^*(\tau)E_{LO}(\tau)} + \text{c.c.} \right\}. \end{aligned} \quad (2.31)$$

If we take the ensemble average of  $\overline{I(0)} \overline{I(\tau)}$  to get the intensity correlation function appearing in Eq. (2.16), the ten terms containing factors of  $e^{-i\omega\tau}$  vanish since

---

<sup>†</sup> For the purpose of our experiments,  $\Delta\omega_{LO}$  is on the order of a few kHz.

$$\langle B(\tau)e^{-i\omega\tau} \rangle = \lim_{T \rightarrow \infty} \frac{1}{2T} \int_{-T}^T B(\tau)e^{-i\omega\tau} d\tau = 0, \quad (2.32)$$

for any slowly varying function  $B(\tau)$ . Furthermore, if  $\overline{A_{LO}}$  is constant in time, we get

$$G^{(2)}(\tau) = \langle \overline{I_s(0)} \overline{I_s(\tau)} \rangle + \overline{I_{LO}}^2 + 2 \overline{I_{LO}} \langle \overline{I_s(0)} \rangle + \frac{c^2 \mathcal{E}^2}{4} \left\{ \langle \overline{E_s^*(0)E_{LO}(0)} \overline{E_{LO}^*(\tau)E_s(\tau)} \rangle + \text{c.c.} \right\}, \quad (2.33)$$

where  $\overline{I_{LO}} = \frac{c\mathcal{E}}{2} \overline{|A_{LO}|^2}$  is the intensity of the local oscillator. If  $|A_{LO}| \gg |h_{\mathbf{q}}(t)|$ , and we neglect the time-independent second and third terms in (2.33), the intensity correlation function reduces to

$$G^{(2)}(\tau) = \frac{c^2 \mathcal{E}^2}{4} \left\{ \langle \overline{E_s^*(0)E_{LO}(0)} \overline{E_{LO}^*(\tau)E_s(\tau)} \rangle + \text{c.c.} \right\}. \quad (2.34)$$

Substituting Eq. (2.30) for the fields and Eq. (2.21) for  $h_{\mathbf{q}}(t)$ , one gets

$$G^{(2)}(\tau) \propto \overline{I_{LO}} \left\{ \langle \Delta H_{\mathbf{q}}^*(0) \Delta H_{\mathbf{q}}(\tau) \rangle e^{i\Delta\omega_{LO}\tau} + \text{c.c.} \right\}, \quad (2.35)$$

$$P^{(2)}(\omega) \propto \overline{I_{LO}} \left\{ P_{H_{\mathbf{q}}}(\omega - \Delta\omega_{LO}) + P_{H_{\mathbf{q}}}(-\omega - \Delta\omega_{LO}) \right\}, \quad (2.36)$$

where  $P_{H_{\mathbf{q}}}(\omega)$  is the power spectrum of the hydrodynamic fluctuations in  $H$  for a particular wavevector  $\mathbf{q}$ ,

$$P_{H_{\mathbf{q}}}(\omega) \equiv \lim_{T \rightarrow \infty} \frac{1}{2T} |\Delta H_{\mathbf{q}}(\omega)|^2 = \int_{-\infty}^{\infty} \langle \Delta H_{\mathbf{q}}^*(0) \Delta H_{\mathbf{q}}(\tau) \rangle e^{i\omega\tau} d\tau. \quad (2.37)$$

Combining Eqs. (2.17) and (2.36), we finally see that the power spectrum of the detector signal is related to the power spectrum of the hydrodynamic fluctuations of the quantity  $H$  by

$$P_f(\omega) \propto \overline{I_{LO}} \left\{ P_{H_{\mathbf{q}}}(\omega - \Delta\omega_{LO}) + P_{H_{\mathbf{q}}}(-\omega - \Delta\omega_{LO}) \right\}. \quad (2.38)$$

Note that 1) the phase fluctuations again cancel out in the intensity correlation function,

provided the scattered light and the local oscillator fields are coherent, 2) the signal level can be increased by increasing  $\overline{I_{LO}}$ , making detector noise negligible, and 3) the relation between  $P_j(\omega)$  and  $P_{Hq}(\omega)$  is much simpler than that for homodyne detection and does not require the fluctuation  $\Delta H_q$  to be a Gaussian process (cf. Eqs. 2.27 and 2.28).

If the local oscillator beam has the same frequency as the probing beam ( $\Delta\omega_{LO} = 0$ ), the power spectrum of the detector signal of Eq. (2.38) becomes

$$P_j(\omega) \propto \{P_{Hq}(\omega) + P_{Hq}(-\omega)\}, \quad (2.39)$$

which means that the power spectrum  $P_{Hq}(\omega)$  for positive and negative frequencies are superimposed. When heterodyne spectroscopy is used to study equilibrium interfacial fluctuations,  $P_{Hq}(\omega)$  is even in  $\omega$ . Hence the power spectrum of the detector signal is directly proportional to the power spectrum of  $\Delta H_q$

$$P_j(\omega) \propto 2P_{Hq}(\omega) . \quad (2.40)$$

For a system out of equilibrium, however, this does not hold, because  $P_{Hq}(\omega)$  and  $P_{Hq}(-\omega)$  are different [Grant and Desai 1983; Desai and Grant 1986] (see Fig. 2.2). Usually the power spectrum  $P_{Hq}(\omega)$  is bounded by a certain frequency range  $\omega_{max}$ , such that  $P_{Hq}(\omega) \approx 0$  for  $|\omega| > \omega_{max}$ . If the frequency shift  $\Delta\omega_{LO}$  of the local oscillator is larger than the frequency range  $\omega_{max}$ ,  $P_{Hq}(-\omega - \Delta\omega_{LO})$  can be neglected for  $\omega > 0$  and  $P_j(\omega)$  is proportional to the spectrum of the hydrodynamic fluctuations  $P_{Hq}(\omega)$  shifted by an amount  $\Delta\omega_{LO}$

$$\boxed{P_j(\omega) \propto P_{Hq}(\omega - \Delta\omega_{LO}) \text{ for } \omega > 0.} \quad (2.41)$$

This frequency-shifted spectrum is illustrated in Fig. 2.2.

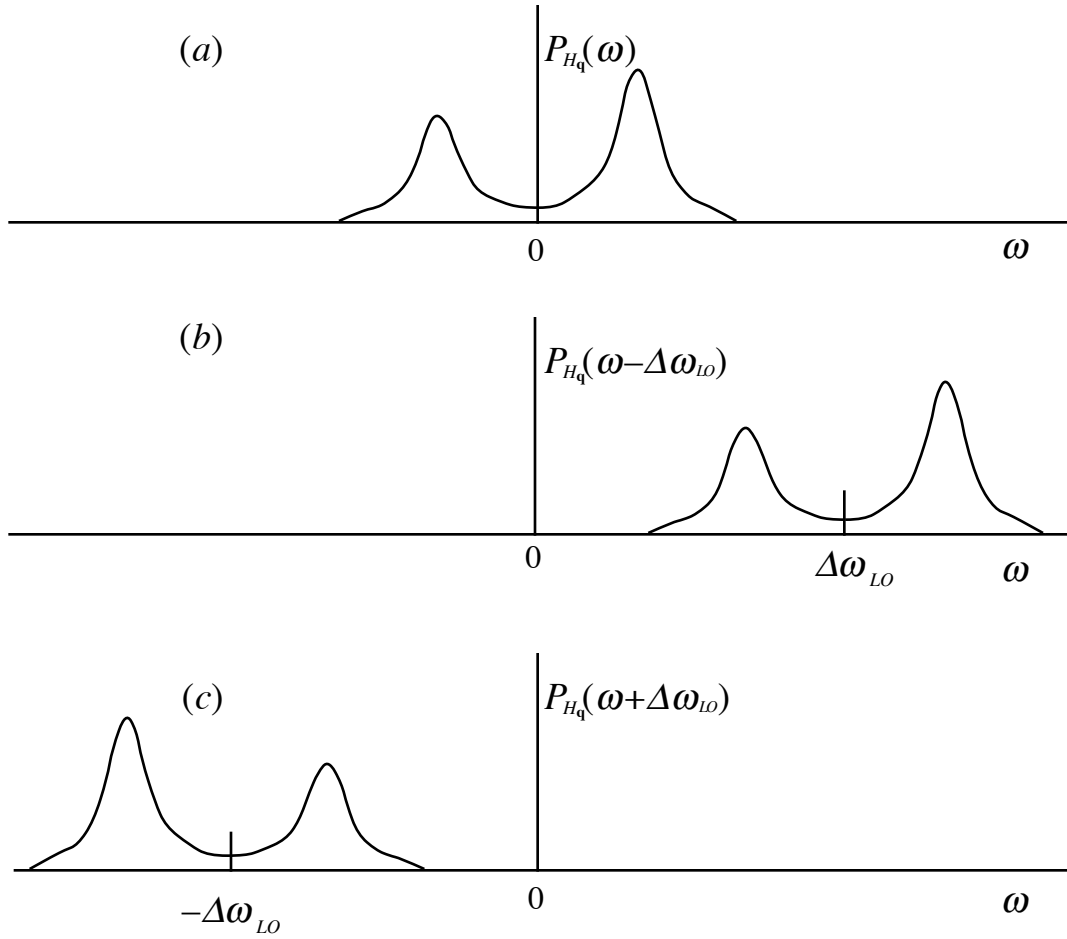


Fig. 2.2. Schematic representation of the power spectra of hydrodynamic fluctuations in a quantity  $H$ ; unshifted (a) and frequency-shifted (b and c), representing, respectively, the first and second terms in Eq. (2.38).

## §2.2 Surface light scattering technique

The general scheme of a heterodyne light scattering apparatus is shown in Fig. 2.3. Scattered laser light is combined with a local oscillator and the resulting beats are measured with a detector. The power spectrum of the beat signal can be shifted by changing the frequency of the local oscillator as in Eq. (2.41). We review here several techniques for the

generation and frequency shifting of the local oscillator, and for the measurement of the beat signal spectrum.

In early heterodyne experiments [Lastovka and Benedek 1966; Wu and Webb 1973] the local oscillator was supplied by stray light scattered by impurities in (or on optical elements such as a lens or window near) the scattering volume. This method does not call for any alignment of the local oscillator, but makes it hard to control the intensity of the local oscillator and match it to the scattered light intensity. Nowadays the most widely used technique for creating a local oscillator involves the use of a diffraction grating [Hård, Hamnerius *et al.* 1976; Shih 1984]. While this technique allows one to control the intensity, one is limited to a fixed scattering angle determined by the ruling of the grating, and one cannot readily shift the frequency of the local oscillator.

Alternatively, one can generate a separate local oscillator beam using a beamsplitter [Mazur and Chung 1987; Chung, Lee *et al.* 1988]. This allows one to control many properties of the local oscillator, such as its frequency, polarization, collimation, etc. There are several ways to recombine the local oscillator with the scattered light. One can either recombine the local oscillator with the scattered light using a second beamsplitter, or cross the local oscillator and probe beams at the interface. Recombining the two beams with a beamsplitter is generally time-consuming and difficult especially when the setup is floated by a pneumatic vibration isolation system. If a fiber optic directional coupler is used to combine the two beams, the alignment of the two beams is unnecessary, although residual table vibrations still limit the accuracy of the scattering angle.

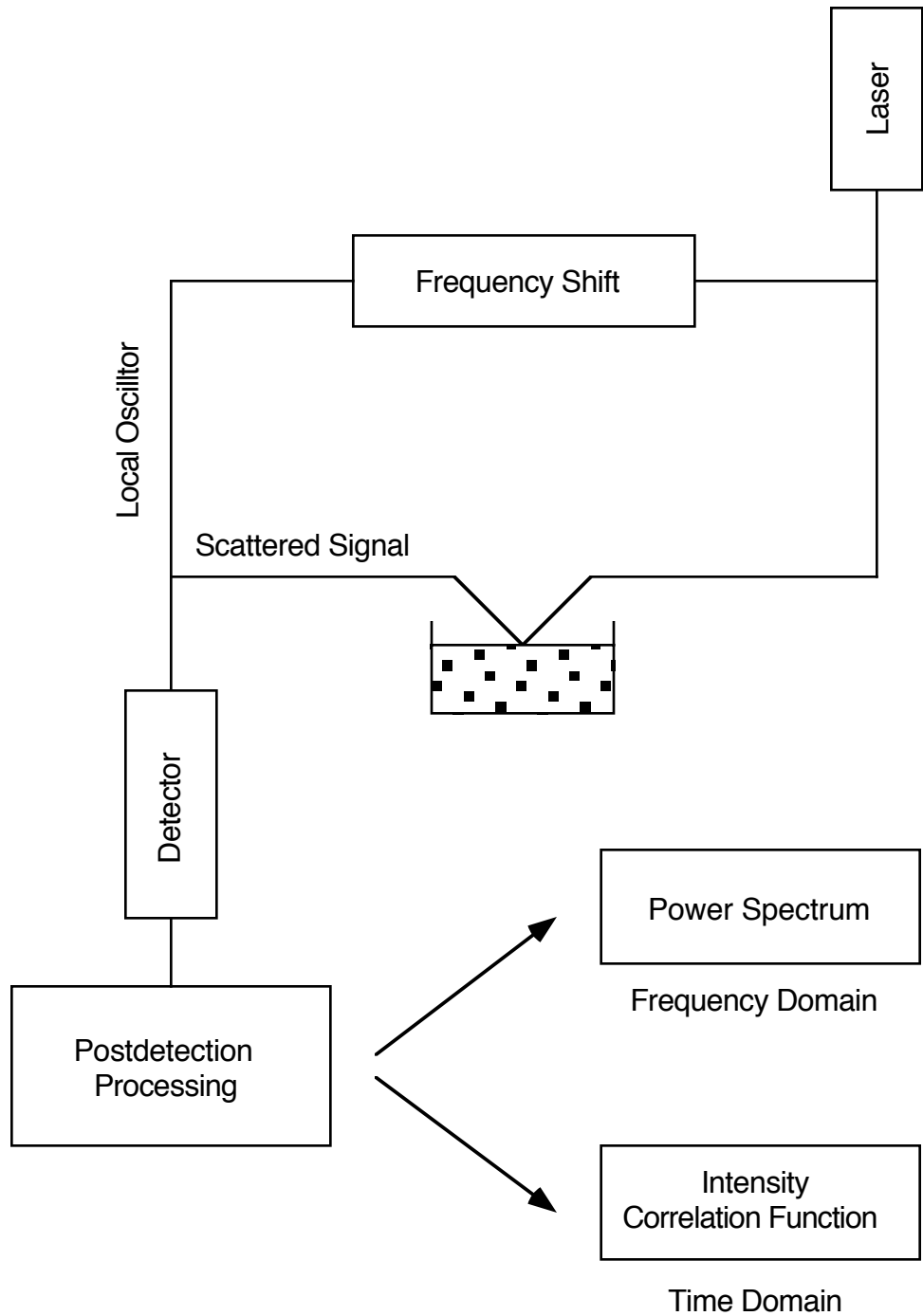


Fig. 2.3. Schematic diagram of a surface light scattering experiment.

If the local oscillator beam crosses the probe beam at the liquid interface at an angle  $\theta$ , it automatically overlaps with the light scattered at that angle. Since motion of the liquid interface changes the directions of both the scattered signal and local oscillator beams by the same amount without changing  $\theta$ , the alignment is insensitive to interfacial motion. Furthermore, since one no longer needs a pinhole to select a scattering angle, the detector viewing angle can be made large enough to cover any wandering of the beams resulting from interfacial motion. Fig. 2.4 shows several optical arrangements that can be used for small scattering angles. In each case crossing is achieved by focussing two parallel beams at the interface. The last arrangement, (*d*), involving an entirely separate local oscillator, allows one to continuously vary the scattering angle  $\theta$  by simple translation of a beamsplitter.

To obtain efficient mixing of the local oscillator and the scattered light, it is essential that the two are coherent at the detector. Thus the optical path length of the local oscillator is adjusted with a delay line to make it equal to the path length of the main beam. Also to ensure spatial coherence, the two beams are carefully overlapped at the detector. The two-parallel-beam arrangement shown in Fig. 2.4*d* ensures good spatial overlap, independent of any residual interfacial motion.

As shown in the previous section one needs to shift the frequency of the local oscillator to separate contributions from interfacial fluctuations travelling in opposite directions (see Eq. 2.41). This shifting of the local oscillator frequency has an additional advantage. Eq. (2.30) shows that the beat signal contains a large dc component,  $\overline{I_{LO}}$ , which reduces the dynamic range of the detector signal. To remove this unwanted dc component one normally uses a high-pass electronic filter. However, this results in a distortion in the low frequency region of the spectrum. By changing the local oscillator

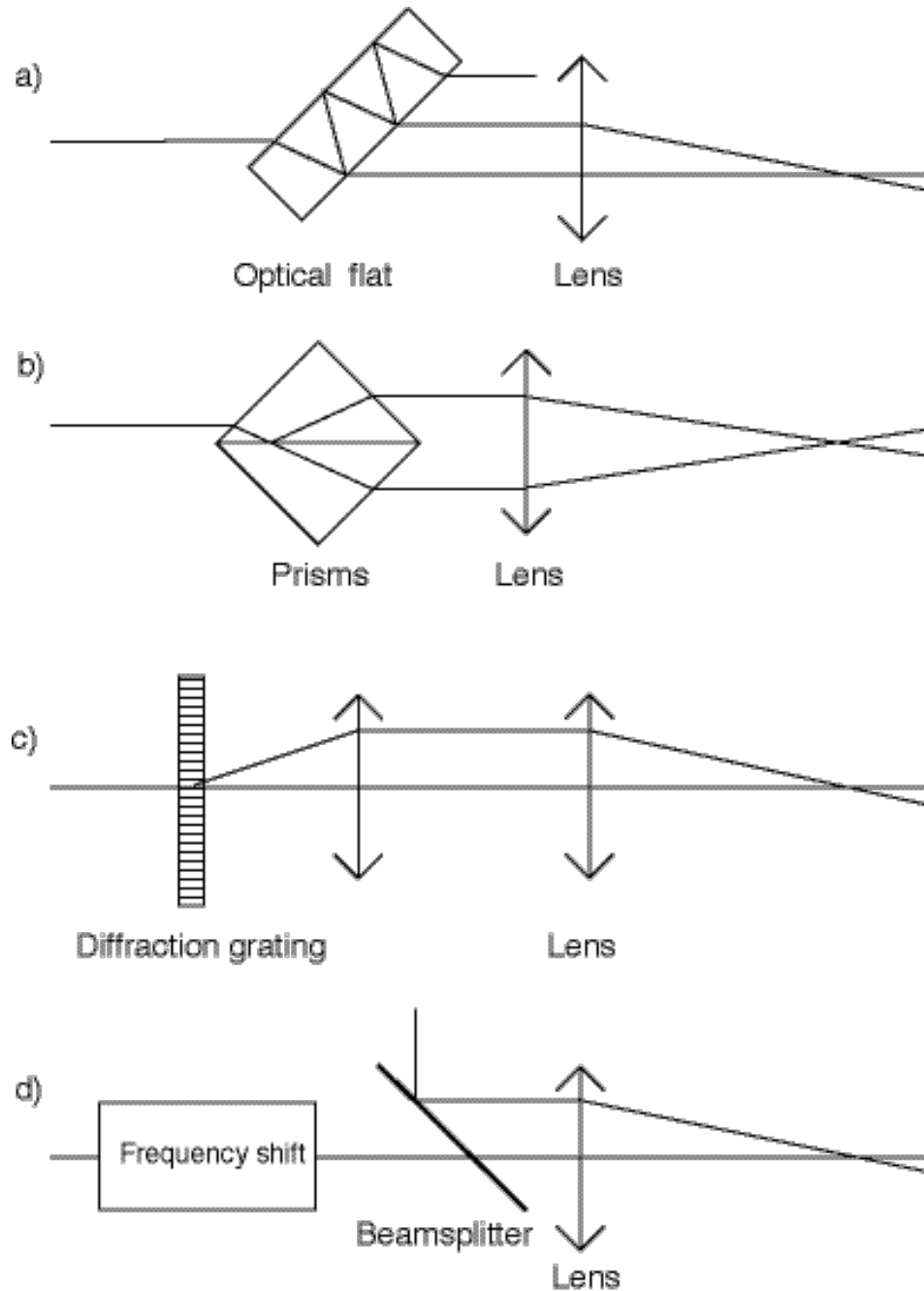


Fig. 2.4. Examples of parallel-beam methods. A pair of beams are made parallel by (a) an optical flat, (b) a prism pair [Pike and Jakeman 1974], (c) a diffraction grating and a lens, or (d) a beamsplitter. Then two beams are focussed onto a single probing point using a lens. The angle of convergence is determined by the focal length of the converging lens and the distance between the two parallel beams which can be changed by (a) rotating the optical flat, (b) translating the prism pair, (c) using another diffraction grating and lens, or (d) translating the beamsplitter. Only method (d) allows one to shift the frequency of the local oscillator beam.

frequency the entire power spectrum can be shifted out of this low frequency region, allowing one to study very low frequency fluctuations which would otherwise be filtered out. According to Eq. (2.41) these very low frequency fluctuations will be visible in the power spectrum of the detector signal near the frequency shift  $\Delta\omega_{LO}$  of the local oscillator. These advantages play an important role in the applications discussed in sections §2.4.1 and §2.4.2, which require a shift of only a few kHz. Generally the optimal frequency shift is determined by the spectral range of the particular application.

One way of shifting the frequency of a laser beam by a few kHz is to reflect it from a moving mirror. The Doppler shift of the reflected beam is

$$\Delta f = 2 \frac{v}{\lambda}, \quad (2.42)$$

with  $v$  the longitudinal component of the velocity of the mirror,  $\lambda$  the wavelength of the beam. For a He-Ne laser ( $\lambda = 632.8$  nm) a frequency shift  $\Delta f = 5$  kHz requires a mirror speed of only 1.6 mm/s. For a typical coherence length of about 0.3 m for an unstabilized He-Ne laser this allows one to sample the detector signal up to 20 s in a single pass of the mirror. However, this method is limited by the stability of the moving mechanism.

Another way of obtaining small frequency shifts, first used by us in 1987 [Mazur and Chung 1987], is by acousto-optic modulation [Yariv 1989]. Acousto-optic modulators typically operate in the MHz frequency range,<sup>†</sup> which is much larger than the desired shift. For that reason, we use a scheme involving two slightly detuned modulators to generate a frequency shift in the kHz regime. The up-shifted component from the first modulator driven at a carrier frequency  $f_1$  is used as an input to the second one driven at a carrier frequency  $f_2$ . The down-shifted component of the second modulator then has a resulting frequency shift

---

<sup>†</sup> At lower frequencies it is impossible to separate spatially the various frequency components of the light diffracted by the acousto-optic crystal.

$$\Delta f_{LO} = f_1 - f_2 . \quad (2.43)$$

Since the carrier frequencies  $f_1$  and  $f_2$  are radio-frequency,  $\Delta f_{LO}$  can be controlled very accurately using crystal oscillators.

The beat signal can be processed in the time domain to get an intensity correlation function or in the frequency domain to get the power spectrum. In early light beating experiments of 1964 the power spectrum was obtained by scanning a narrow band electric filter over a magnetically recorded detector signal [Cummins, Knable *et al.* 1964]. The resolution, determined by the bandwidth of the filter, was typically about 1 Hz. Later, autocorrelators were introduced which made it possible to measure the intensity correlation function in Eq. (2.27) directly. Autocorrelators make more efficient use of the signal than a scanning electric filter and provide the correlation function in real-time [Asch and Ford 1973]. This technique also works well in the photon-counting regime. Since the measured correlation function is a *product* of the instrumental function and the signal correlation function, not a convolution, removing the instrumental contribution is mathematically easier than in the case of power spectrum. Because of these advantages autocorrelators have become standard equipment in dynamic quasi-elastic light scattering experiments [Chu 1974]. However, recent advances in computer technology have again rendered frequency domain analysis more practical. We have obtained excellent results using a personal computer equipped with an analog-to-digital converter board as a spectrum analyzer [Mazur and Chung 1987]. Alternatively one can synthesize the autocorrelation function directly from the digitized data points. This computer-based method is versatile, convenient for data analysis, and, above all, very cost effective. In our experiment, the ac component of the photomultiplier signal is amplified and digitized by a GW Instruments MacAdios II computer board inside a Macintosh II computer. Then the power spectrum of the detector signal is obtained by Fourier transforming the digitized waveform. The transform executed is a discrete fast Hartley transform, which is equivalent to a fast Fourier transform but which requires half the number of operations [Bracewell 1986].

## §2.3 Experimental limits of Fourier transform heterodyne spectroscopy

### §2.3.1 Instrumental resolution

As we have seen the spectral resolution of heterodyne spectroscopy is not limited by fluctuations in the phase of the light source. Factors that contribute to the instrumental resolution limit  $\delta f_{inst}$  are the finite sampling time, as well as electronic, mechanical and optical instabilities .

The most fundamental limitation results from the finite sampling time (cf. Eq. 2.10). If the detector signal  $j(t)$  is sampled for a period  $\mathcal{T}$  (the sampling time), then the frequency interval  $\delta f_{samp}$  between adjacent spectral points in the Fourier transform of  $j(t)$  is given by

$$\delta f_{samp} = \frac{1}{\mathcal{T}} . \quad (2.44)$$

This resolution limit imposed by the sampling time can be made arbitrarily small by increasing the sampling time  $\mathcal{T}$ . For a sampling time of four hours,  $\delta f_{samp}$  is 70  $\mu\text{Hz}$  which for a He-Ne laser corresponds to a Doppler shift resulting from a speed of 0.2  $\text{\AA}/\text{s}$ . In practice the instrumental resolution is determined by a convolution of limits due to electronic instabilities  $\delta f_e$  and to optical path length fluctuations  $\delta f_o$

$$\delta f_{inst} = \delta f_e \oplus \delta f_o , \quad (2.45)$$

where  $\oplus$  denotes the convolution of the two contributions.<sup>†</sup> These two resolution limits,  $\delta f_e$  and  $\delta f_o$  are considered in more detail below.

Fluctuations in the frequency shift  $\Delta f_{LO}$  of the local oscillator,  $\delta f_{LO}$ , and fluctuations

---

<sup>†</sup> For example, if these two contributions are Gaussian, the resulting resolution limit is given by

$$\delta f_{inst} = \sqrt{\delta f_e^2 + \delta f_o^2} .$$

in the digitization clock-rate  $\delta f_{clock}$  (see the next section), contribute to the electronic instabilities:

$$\delta f_e = \delta f_{LO} \oplus \delta f_{clock} . \quad (2.46)$$

Since the frequency shift  $\Delta f_{LO}$  is equal to the difference between the two rf carrier frequencies  $f_1$  and  $f_2$  for the two acousto-optic modulators (see Eq. 2.43),  $\delta f_{LO}$  is determined by the electronic drifts of the rf drivers for the acousto-optic crystals. One can easily get a carrier frequency stability of 100 Hz for a typical 40 MHz carrier frequency with a crystal oscillator; the frequency drifts of the crystal oscillator are mainly caused by temperature fluctuations. The stability of  $\Delta f_{LO}$  can be improved by either stabilizing the temperature of the separate crystal oscillators or by putting the two rf drivers into the same environment and letting them drift by the same amount. Using the latter method without temperature control of the crystal oscillators, we found that  $\delta f_{LO}$  was about 0.1 Hz by measuring the electronic beat signal of the rf outputs directly. This limit can be reduced further by locking the two crystal oscillators to a single oven-controlled time base; this way  $\delta f_{LO}$  could be further reduced down to 1  $\mu$ Hz.

Let us now turn to the second term in Eq. (2.45). In Eqs. (2.20) and (2.29), we assumed the path lengths of the two beams are fixed. In reality, changes in the index of refraction of the air, mechanical perturbations of the optical elements due to temperature fluctuations, and acoustic noise cause optical path length fluctuations  $\delta f_o$ . For a temperature change of 1 K/hour, for example, a 1-m long optical path length contracts at the speed of about 2.5  $\text{\AA}/\text{s}$  resulting from changes in the index of refraction of air. At the same time such a change in temperature would lead to a thermal expansion of the optical table of about 0.5  $\text{\AA}/\text{s}$  for a table made from carbon steel. Temperature fluctuations of 1 K/hour therefore would limit the resolution to about 300  $\mu$ Hz.<sup>†</sup> A rough estimate of the effect of a

---

<sup>†</sup> Note that the Doppler shift due to a decrease in optical pathlength is one half of that in Eq. (2.42), since we are not dealing with a reflection here.

100-Hz sound of 50 dB on a typical aluminum optical mount of 5-cm height and a square cross section of 1 cm<sup>2</sup> yields a lateral speed of the top surface of less than 0.1 Å/s, corresponding to a resolution limit resulting from acoustic noise  $\delta f_{noise}$  of about 30  $\mu$ Hz.

One should keep in mind, however, that the resolution limit is determined by the *difference* in Doppler shift of the local oscillator and signal beams, so the effective resolution limits  $\delta f_{temp}$  and  $\delta f_{noise}$  are generally much smaller than the above estimates. For the two-parallel-beam method (see Fig. 2.4d), the local oscillator and signal beams have almost identical paths, so the resolution limit resulting from optical path length fluctuations is negligible for all practical purposes.

We determined the instrumental resolution  $\delta f_{inst}$  by mixing the local oscillator directly with the main laser beam as shown in Fig. 2.5, and investigated the contribution of the various terms in Eqs. (2.45) and (2.46). The local oscillator was frequency-shifted using a combination of two acousto-optic modulators as described in the previous section. The two carrier frequencies of the modulators were in the 20–40 MHz range, with a frequency difference of 5 kHz.

The resolution was found to increase with increasing sampling time as expected from Eq. (2.44). When the two modulators were driven by two independent rf drivers (ME-40, IntraAction Corp.), a loss of resolution started to occur for sampling times longer than 60 s (open squares in Fig. 2.6). By comparing the FWHM of the 5-kHz peak in the optical beat spectrum with the one obtained by directly beating the two rf carrier signals, it was found that this loss of resolution was entirely caused by instabilities in the carrier frequencies (diagonal crosses). With two Hewlett-Packard 3325-B frequency synthesizers,

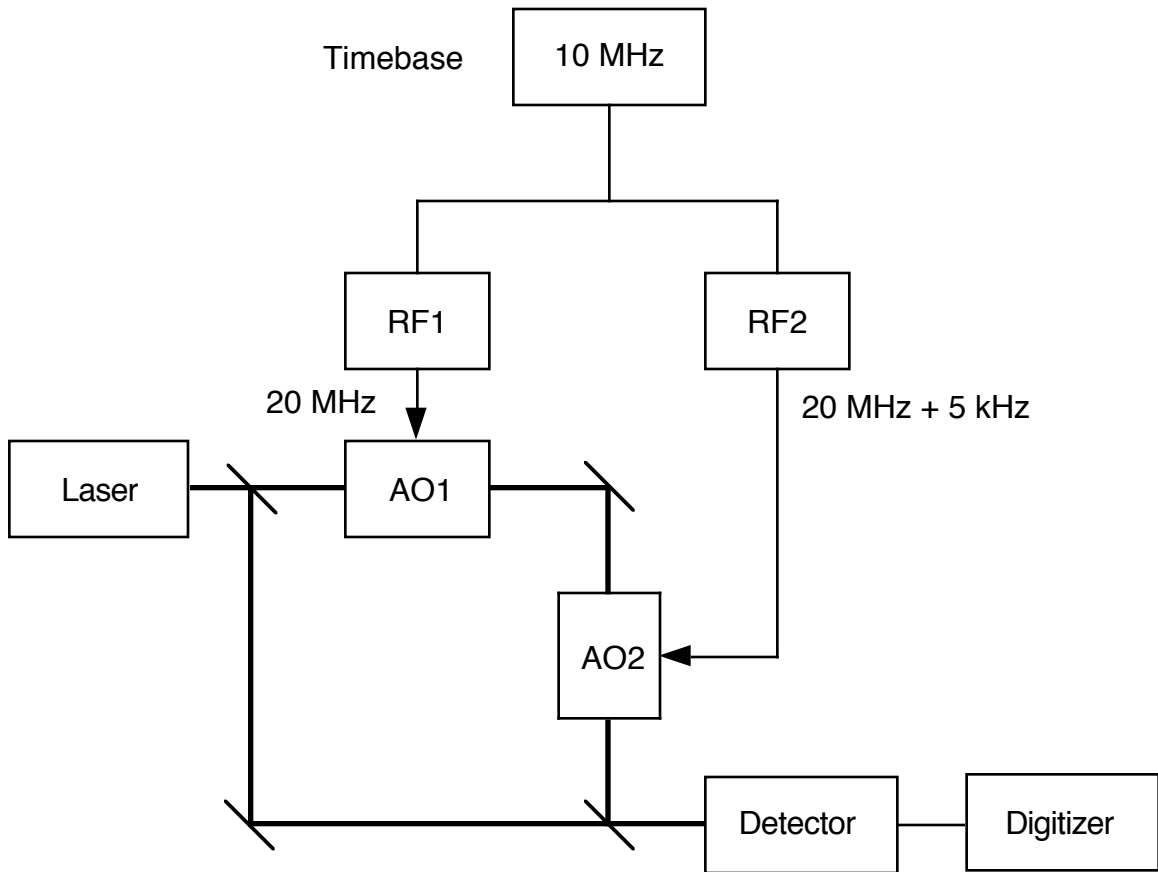


Fig. 2.5. Experimental setup for the measurement of the instrumental resolution using locked rf signals. AO1 and AO2 are two acousto-optic modulators. RF1 and RF2 are the two rf amplifiers for the acousto-optic modulators driven by two frequency synthesizers locked to a common time base.

locked to the same oven-controlled time base, the situation could be improved by a factor of one hundred. As can be seen in Fig. 2.6, the rf resolution follows Eq. (2.44) down to  $140 \mu\text{Hz}$  (vertical crosses). The optical resolution, on the other hand, starts to deviate from the theoretical value of Eq. (2.44) at about  $400 \mu\text{Hz}$ , most probably because of optical path length fluctuations of the setup during the half-hour sampling time. The highest instrumental resolution of the present setup,  $200 \mu\text{Hz}$ , was obtained with a four-hours amplifying time. As mentioned before, this resolution could be further improved by reducing the differences in the environment between the local oscillator and signal beams.

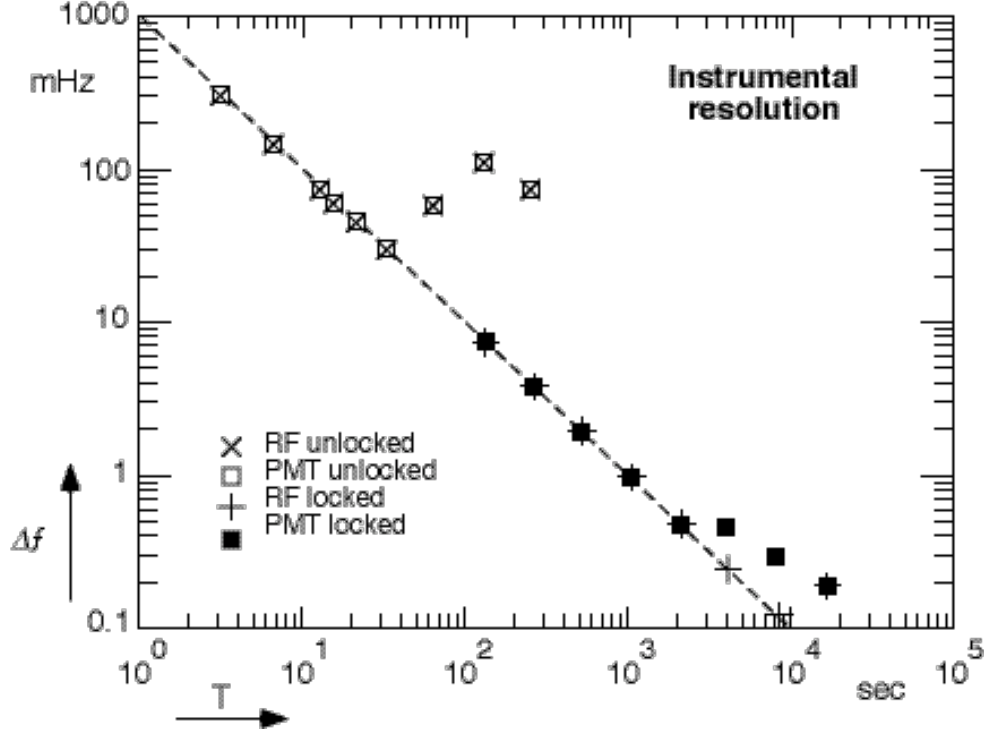


Fig. 2.6. Instrumental resolution as a function of sampling time. The crosses represent the FWHM ( $\delta f$ ) of the central peak in the beat spectra of the two rf carrier signals; the squares represent those of the mixed beams at the photo-multiplier tube (PMT). The dotted line is the resolution limit due to finite sampling time given by Eq. (2.44).

### §2.3.2 Free spectral range

If the detector signal  $j(t)$  is sampled at a sampling frequency  $f_s$  (the inverse of the interval between adjacent sampling points,  $\Delta \mathcal{T}$ ), then the spectrum, obtained by a discrete Fourier transform of the signal  $j(t)$ , has a free spectral range  $\mathcal{F}$  given by<sup>†</sup>

<sup>†</sup> It is interesting to note here that the stability of the digitizer clock signal does not influence the resolution as much as that of the rf carrier frequencies. Fluctuations in the sampling rate due to clock signal instabilities lead to an uncertainty of the free spectral range in Eq. (2.47). If the total sampling time  $\mathcal{T}$  is composed of  $N$  sampling intervals with an accuracy of  $a (\ll 1)$ , the uncertainty of each point in the frequency spectrum is given by

$$\delta f_{clock} \approx a \frac{f_s}{N} = a \frac{1}{\mathcal{T}} = a \delta f_{samp}.$$

Therefore,  $\delta f_{clock}$  is much smaller than the sampling time limit,  $\delta f_{samp}$ , which cannot be avoided.

$$F = \frac{1}{2\Delta T} = \frac{1}{2} f_s. \quad (2.47)$$

Generally, the upper limit of the free spectral range is determined either by the detector response time or by the speed of the signal digitizer; in practice, with a 1-nsec detector response time and a fast transient digitizer, the free spectral range can be extended to the GHz regime. With a streak camera this could even be further extended by at least two orders of magnitude.

Because of the high sub-mHz resolution, and the large spectral range of several GHz, this technique is applicable to a wide variety of fields of research. The only other practical limit one needs to consider is the computation time required to analyze the detector signal. As one increases the number of data points,  $N$ , the time it takes to transform the data grows as  $N \log_2 N$ . With a Macintosh II personal computer, the time needed to calculate the power spectrum of  $2^{16}$  data points is about 40 s. However, this time can easily be reduced with faster computers. Table 2.1 summarizes various experimental aspects of the Fourier transform heterodyne technique.

		Limiting factors	Current limit
Resolution Limits	$\delta f_{samp} = \frac{1}{\mathcal{T}}$	Sampling time (4 hours)	70 $\mu$ Hz
	$\delta f_o$	Temperature drift (1K/hour)	< 300 $\mu$ Hz
	$\delta f_{noise}$	Acoustic noise (100 Hz, 50 dB)	30 $\mu$ Hz
	$\delta f_{inst}$	Rf oscillator precision	1 $\mu$ Hz
	$\delta f_e$	Clock accuracy ( $2.5 \times 10^{-6}$ )	0.2 nHz
	$\delta f_{clock}$		
Spectral range	$\mathcal{F} = \frac{1}{2\Delta\mathcal{T}} = \frac{N\delta f_{samp}}{2}$	Detector response time (< 1 ns)	> 1 GHz
Computation time	$M \log_2 N$ , $N = \mathcal{T}' f_s$	CPU/FPU ( $N = 2^{16}$ , Mac II)	40 s

Table 2.1. Experimental range and limitations of the Fourier transform heterodyne technique. Limiting factors and current limits of various contributions to the resolution limit are given. Spectral range and required computation time are also given.

## §2.4 Applications of Fourier transform heterodyne spectroscopy

### §2.4.1 Separation of counter-propagating capillary waves

The most important advantage of using a frequency-shifted local oscillator is the ability to shift the origin of the power spectrum. This enables one to study the asymmetric power spectrum of a system out of equilibrium. To demonstrate this ability, we measured the power spectrum of capillary waves generated by an external force.

When the water surface is perturbed at a frequency  $f_{ind}$  by a transducer, a surface wave is generated and propagates away from the source. If the perturbation is strong enough, there will be a sharp peak in the power spectrum of the surface fluctuation either at frequency  $+f_{ind}$  or  $-f_{ind}$  depending on the direction of propagation of the surface wave. In a surface light scattering experiment a laser beam is incident on the surface. When the surface wave propagates in the same direction as the light, the reflected light scatters into two directions satisfying the condition of energy and momentum conservation

$$\mathbf{k}_{scatt} = \mathbf{k}_{laser} \pm \mathbf{q}_{ind}, \quad (2.48)$$

$$f_{scatt} = f_{laser} \pm f_{ind}, \quad (2.49)$$

where  $(\mathbf{k}_{scatt}, f_{scatt})$ ,  $(\mathbf{k}_{laser}, f_{laser})$ , and  $(\mathbf{q}_{ind}, f_{ind})$  are the wavevectors and frequencies of the scattered light, reflected light, and surface wave, respectively (see Fig. 2.7). The  $\pm$  signs correspond to annihilation and creation of a surface wave of wavevector  $\mathbf{q}_{ind}$ . The scattering angle  $\phi_{ind}$  is given by the phase-matching (momentum conservation) condition Eq. (2.48). Since  $\mathbf{q}_{ind}$  is much smaller than  $\mathbf{k}_{laser}$ , the magnitudes of the incoming and scattered beams are approximately equal,

$$k_{scatt} \approx k_{laser}, \quad (2.50)$$

and one finds

$$q_{ind} = k_{laser} \{ \sin(\theta_0 + \phi_{ind}) - \sin\theta_0 \} \approx \phi_{ind} k_{laser} \cos\theta_0, \quad (2.51)$$

where  $\theta_0$  is the incidence angle.

For a surface wave of the same frequency  $f_{ind}$ , propagating in the opposite direction, Eqs. (2.48) and (2.49) are modified as

$$\mathbf{k}_{scatt} = \mathbf{k}_{laser} \pm \mathbf{q}', \quad (2.52)$$

$$f_{scatt} = f_{laser} \pm f_{ind}, \quad (2.53)$$

with

$$\mathbf{q}' = -\mathbf{q}_{ind}. \quad (2.54)$$

Therefore, for a given scattering angle, the frequency of the scattered light changes by the amount  $\pm f_{ind}$  depending on the propagation direction of the surface wave. If an unshifted local oscillator is used in a surface light scattering experiment, however, the power

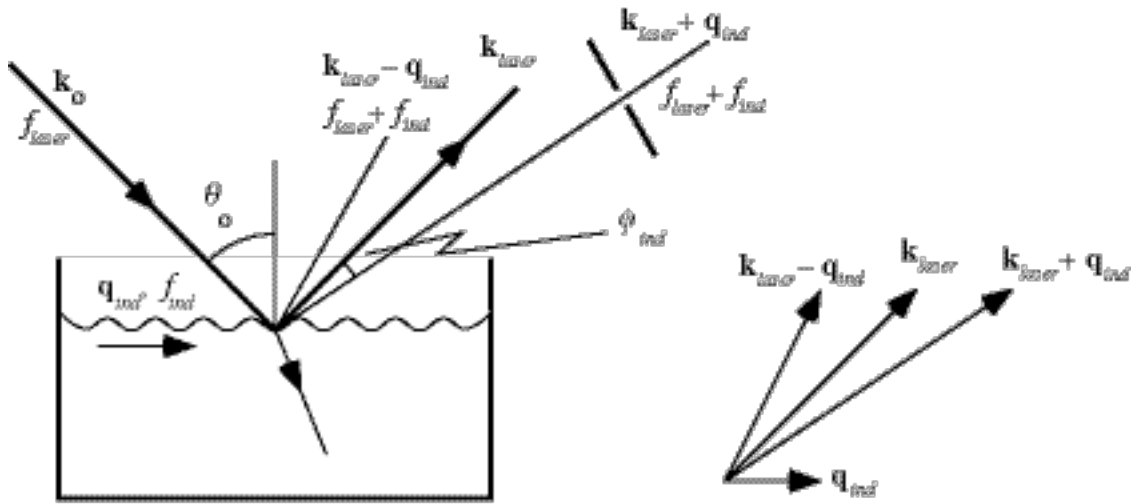


Fig. 2.7. Optical geometry for measuring the spectra of induced capillary waves. An incident light wave with wavevector  $\mathbf{k}_0$  and frequency  $f_{laser}$  is reflected from the surface at an angle  $\theta_0$ . The reflected light is scattered from a capillary wave with wavevector  $\mathbf{q}_{ind}$  and frequency  $f_{ind}$ . The scattering angle  $\phi_{ind}$  of the inelastically scattered light is determined by the phase-matching (momentum conservation) condition. Behind the pinhole the spectrum consists of a central peak at  $f_{laser}$ , and, for the capillary wave shown, a single capillary wave peak at  $f_{laser} + f_{ind}$ .

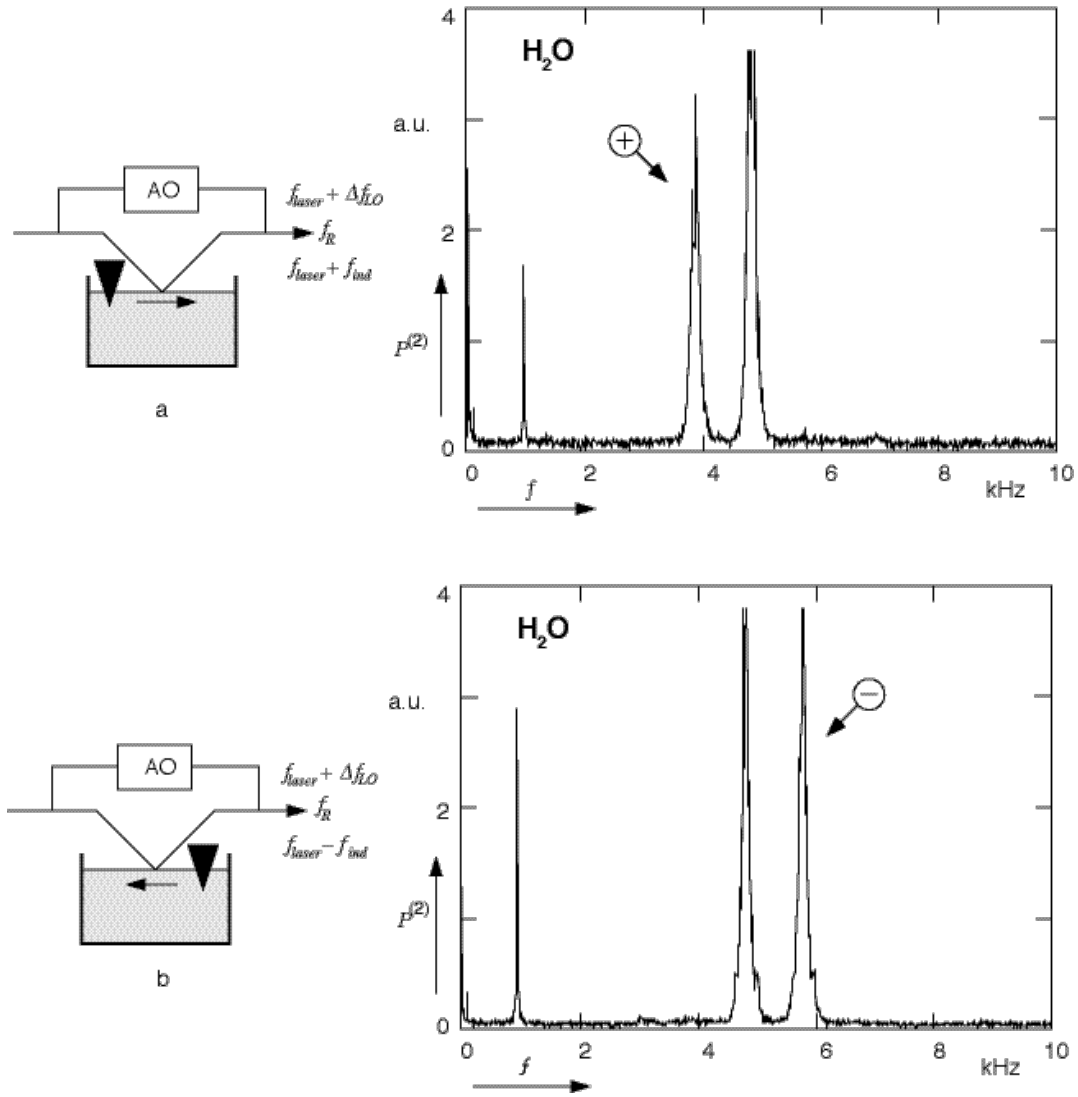


Fig. 2.8. Power spectra of induced capillary waves. A co-propagating (a) or counter-propagating (b) unidirectional capillary wave of frequency  $f_{ind} = 1$  kHz is induced on the water surface by a transducer (black triangle) as shown in the diagrams on the left. In both cases the heterodyne spectrum shows only one capillary wave peak. The  $\oplus$  and  $\ominus$  signs show the beat peaks from the scattered light at  $f_{laser} + f_{ind}$  and  $f_{laser} - f_{ind}$ , respectively. Note that the homodyne peaks, which correspond to the beating of the Rayleigh peak at  $f_R (= f_{laser})$  with the capillary wave peaks at  $f_{laser} \pm f_{ind}$ , appear at  $f_{ind}$ .

spectrum of the detector signal will have a peak at the frequency  $+ f_{ind}$  regardless of the direction of propagation (see Eq. 2.40). If the local oscillator frequency is shifted by an amount  $\Delta f_{LO}$ , for a fixed scattering angle, the peak will appear either at  $\Delta f_{LO} + f_{ind}$  or  $\Delta f_{LO} - f_{ind}$ . A wire attached to a speaker is used as a transducer to perturb the water surface. An electric signal of 1 kHz is supplied to the speaker to induce capillary waves at that

frequency. For a given scattering geometry, the propagation direction of the induced capillary wave is reversed by changing the position of the transducer relative to the probing point. Fig 2.8a shows the spectrum with an unshifted local oscillator. When the frequency of the local oscillator is shifted by 5 kHz, a sharp peak appears at either 4 kHz or 6 kHz satisfying the conservation laws (see Figs. 2.8a and 2.8b). In addition, there are peaks at 1 kHz and 5 kHz, corresponding to the mixing of stray light with the scattered signal and local oscillator, respectively. Therefore, the ability of our setup to separate counter-propagating capillary waves is confirmed. This will be used in Chapter 4 to study the asymmetry of capillary wave spectrum of water out of equilibrium.

#### **§2.4.2 Epitaxial crystal-growth speed measurements**

Because of the high resolution, one can use the Fourier transform heterodyne spectroscopy technique to observe very small frequency shifts. A possible application is the measurement of extremely small Doppler shifts. To illustrate this we have applied our technique to study solid phase epitaxial growth of silicon. For an isolated piece of amorphous silicon, crystallization occurs through random formation of the nucleation clusters and their subsequent growth. When an amorphous thin film of silicon is in direct contact with a crystalline substrate of silicon, the crystalline phase provides a template for ordered crystallization of amorphous film. This occurs as a layer-by-layer conversion of silicon atoms from the amorphous to the crystalline phase. Since the index of refraction of amorphous silicon is different from that of crystalline silicon, a light beam will be reflected at the crystalline-amorphous silicon interface. One can obtain the growth speed of the interface by monitoring either 1) the interference between the reflected beam from the interface and the local oscillator beam using time-resolved reflectivity measurements [Olson and Roth 1988; Lu 1989] or 2) the Doppler shift of the reflected beam using Fourier transform heterodyne technique.

The experimental details are as follows: A layer of 300-nm thick amorphous silicon on a  $200 \mu\text{m} \times 200 \mu\text{m}$  substrate of crystalline silicon(100) is made by implantation of  $^{30}\text{Si}^+$ . The silicon sample is placed on a heating unit in open air with the amorphous phase facing upwards.<sup>†</sup> Since the silicon sample needs to be heated at 800 K or more to increase the crystal growth speed, high temperature air turbulence around the sample and reduced mechanical stability of the heater holding the sample greatly lower the overall stability of the setup. It is therefore necessary to mix the main laser beam with the local oscillator *before* hitting the sample, to ensure constant overlapping of the two (see Fig. 2.9). The main beam is incident at the Brewster angle to suppress reflection from the front air-amorphous silicon interface, which increases the mixing efficiency of the two specularly reflected beams. The Brewster angle is calculated using the real part of the index of refraction of amorphous silicon at the He-Ne laser wavelength of  $\lambda = 632.8 \text{ nm}$  which is given by [Olson and Roth 1988]

$$n_a = 4.39 + 5 \times 10^{-4} T. \quad (2.55)$$

At 835 K,  $n_a = 4.81$  and the Brewster angle, ignoring any contribution of the surface layer of silicon oxide, is given by

$$\theta = \tan^{-1} n_a = 78.2^\circ. \quad (2.56)$$

At this incidence angle the refraction angle is  $11.7^\circ$  and the change in the vertical component of the growth velocity is only 2% ( $= 1 - \cos(11.7^\circ)$ ). The main beam is *p*-polarized and the frequency-shifted local oscillator is *s*-polarized. Most of the local oscillator beam is reflected at the air-amorphous silicon interface, while most of the main beam penetrates the amorphous layer and is reflected at the crystalline-amorphous interface. Mixing of the two

---

<sup>†</sup> The silicon sample and the temperature control unit were supplied by Prof. M. Aziz at Harvard University.

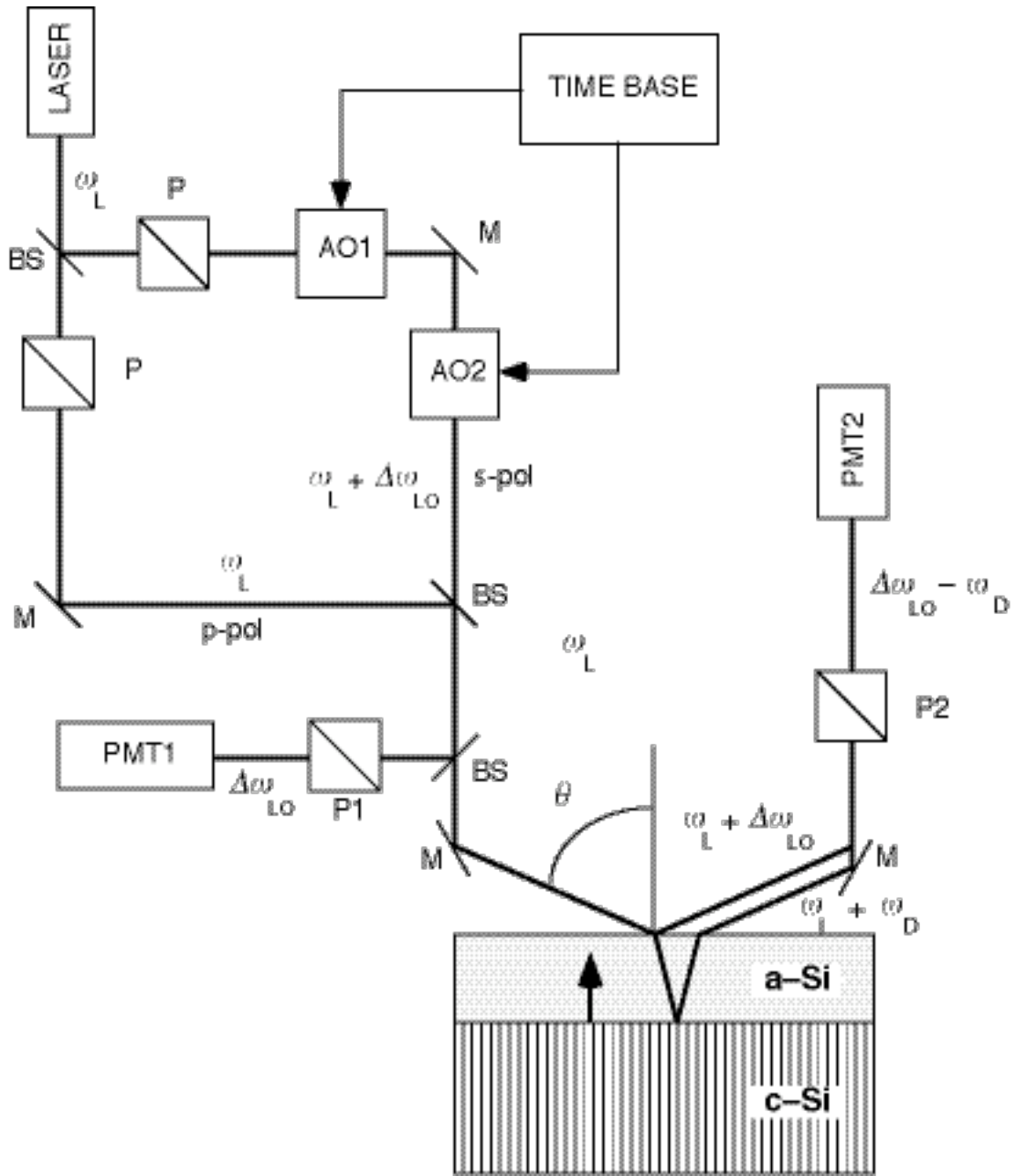


Fig. 2.9. Measurement of the Doppler shift from a growing amorphous/crystalline silicon interface. A *p*-polarized beam at angular frequency  $\omega_L$  and an *s*-polarized beam at  $\omega_L + \Delta\omega_{LO}$  are combined before they hit the interface at Brewster angle  $\theta$ . PMT1 and PMT2 monitor the unshifted and Doppler-shifted peaks, respectively. M, mirror; BS, beamsplitter; P, polarizer; PMT, photomultiplier tube; AO, acousto-optic modulator.

reflected beams is achieved by using a  $45^\circ$ -polarizer. The beat signals are sampled with two photomultiplier tubes. One photomultiplier tube (PMT1), monitoring the beat signal before the sample, provides a reference spectrum without a Doppler shifted peak. The Doppler

shifted spectrum is obtained by another photomultiplier tube (PMT2). The pair of acousto-optic modulators (AOM-40, IntraAction Corp.) are driven at the carrier frequencies of 20.000 MHz and 20.005 MHz. These carrier signals are generated by two Hewlett-Packard 3325-B frequency synthesizers, locked to the same time base to stabilize the shifting frequency of the local oscillator beam.

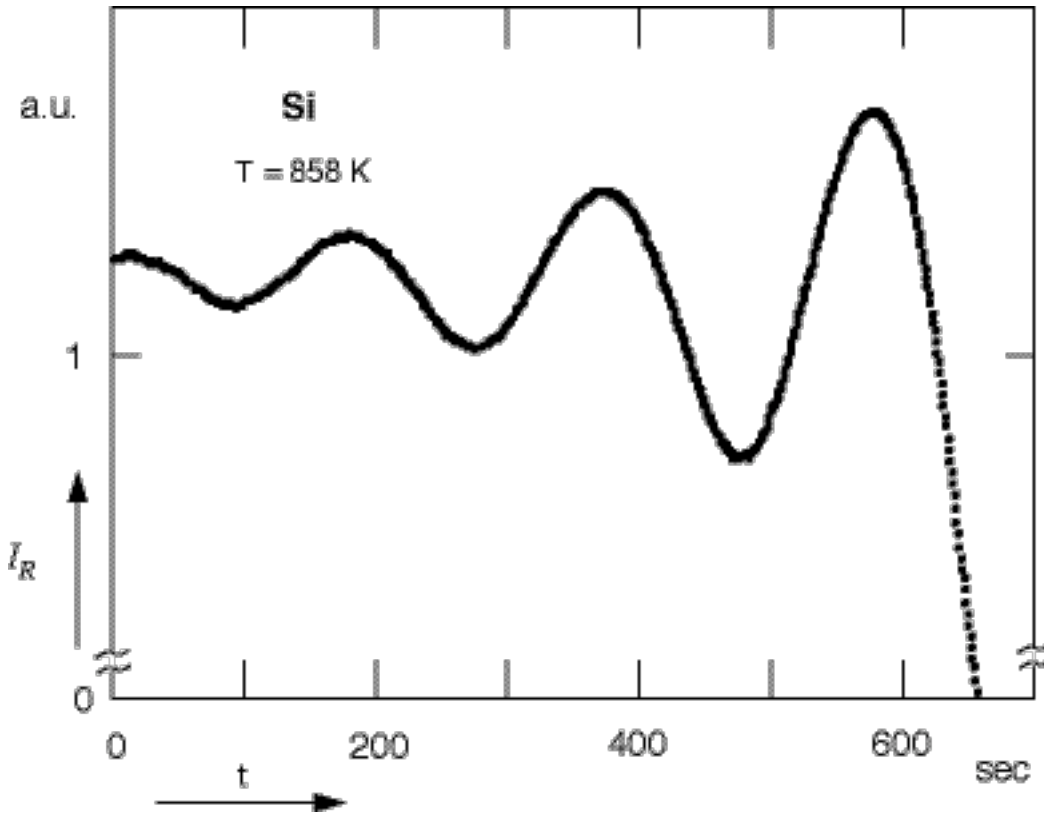


Fig. 2.10. Time-resolved reflectivity measurement of a growing amorphous/crystalline silicone interface at 858 K. The ratio of the outputs from the two PMT's,  $I_R$ , is monitored with time  $t$ .

With the local oscillator beam blocked, the setup is identical to the standard time-resolved reflectivity measurement setup. Fig. 2.10 shows a trace of reflectivity as a function of time when the silicon sample is heated at 858 K. Since the film thickness increment between each successive interference maximum and minimum is  $n_a\lambda/4$ , the growth speed

can be obtained from this trace; this yields a growth speed of 0.35 nm/s in agreement with the published data of Olson and Roth.

With the shifted local oscillator beam unblocked, the spectrum of Fig. 2.11 was

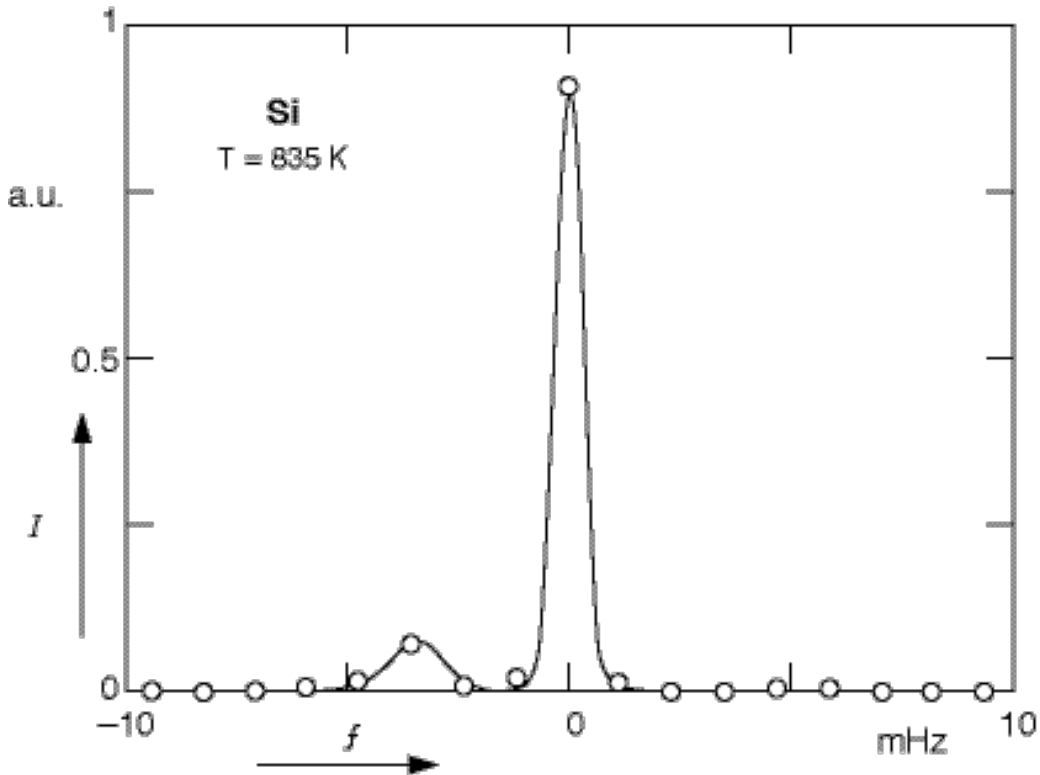


Fig. 2.11. Spectrum of the light reflected from a growing silicon crystal at 835 K. The small peak left of the large central one shows the Doppler shift due to crystal growth. The solid line through the data points is a guide to the eye.

obtained. The signal was sampled for 14 minutes at the rate of 76.9 Hz. Each point in the spectrum is 1.2 mHz apart. Circles are data points from the Fourier transform; the solid line is a guide to the eye. The large peak comes from the beating of the main beam and the local oscillator reflected at the air-amorphous silicon interface. The smaller peak is Doppler shifted by the motion of the crystalline-amorphous interface when the sample is heated at 835 K. The Doppler shift is 3 mHz, corresponding to a growth speed of about 0.2 nm/s.

This is in good agreement with our time-resolved reflectivity measurements and published data [Olson and Roth 1988].

In principle, with increased resolution, one can obtain the *distribution* of growth speeds over the sampled area from the broadening of the Doppler shifted peak (the shift reflects only the *average* speed). The resolution of these measurements is limited by the maximum sampling time, which in turn is limited by the ratio of the amorphous layer thickness to the growth rate. For a fixed growth rate this means one needs thicker samples to increase resolution. However, since the amorphous silicon absorbs a significant amount of visible light, the thickness of the amorphous layer is also limited. The imaginary part of the index of the refraction of amorphous silicon,  $\kappa_a$ , is 0.61 at  $\lambda = 632.8$  nm. For a 300-nm thick layer, 97% of the light is absorbed (the absorption coefficient is  $e^{-4\pi\kappa_a/\lambda}$ ). Thus, it is necessary to probe from the crystalline silicon side which has far less absorption ( $\kappa_s = 0.018$ ) than the amorphous phase. Alternatively, the frequency of the light could be changed to reduce the absorption.

In conclusion, this application demonstrates that ultrahigh resolution work can be done with a relatively simple Fourier transform heterodyne spectroscopy. With a spectral range of up to several GHz and the directional sensitivity demonstrated in the previous section, Fourier transform heterodyne spectroscopy can be applied to study a broad range of physical phenomena.

# Chapter III

## Viscoelastic Properties and Hydrodynamic Fluctuations of Fluid Interfaces

### §3.1 Rheology of interfaces

It is well-known that the actual interface separating two fluids is diffuse [van der Waals 1893; Rowlinson 1979] and rough [Mandelstam 1913]. Ideally one should provide a detailed microscopic description of this inhomogeneous interfacial region, but in practice it is difficult to describe such a nonuniform system [Buff 1952; Kirkwood and Buff 1949]. For a general review, the reader is referred to the monographs of John *et al.* [John, Dahler *et al.* 1981] and Rowlinson and Widom [Rowlinson and Widom 1982]. The description of this system can be simplified by replacing the inhomogeneous interfacial region by a homogeneous *film* with finite thickness between two homogeneous bulk phases [Tiersten 1969].

A further simplification can be made when describing interfacial waves of large wavelength  $\lambda$  such that

$$\lambda \gg d, \tag{3.1}$$

with  $d$  the thickness of the inhomogeneous interfacial region which is on the order of a nanometer away from the critical region [Lee, Barker *et al.* 1974; Schwartz, Schlossman *et al.* 1990]. In this case, the film can be represented by a mathematically sharp equivalent *interface* along with a set of rheological properties of the interface, such as interfacial

tension and dilational modulus. This ‘equivalent interface’ model [Velasco and García-Moliner 1979] has been widely used since the complex problem of describing the interface is replaced by a set of appropriate boundary conditions containing phenomenological interfacial parameters. Let us start this chapter discussing the equivalent interface model and the viscoelastic moduli of the interface. Boundary conditions which should be satisfied by this model are given in the next section.

Consider a system of two fluids separated by a homogeneous film in a large cubical box of volume  $L^3$ . The  $z$ -axis points vertically upwards, with the gravitational force pointing in the negative  $z$ -direction, and the plane  $z = 0$  is the equilibrium position of the film of thickness  $d$ . The lower half-space  $z < -d/2$  is occupied by a fluid having density  $\rho$ , and the upper half-space  $z > d/2$  is occupied by a different fluid whose physical parameters are denoted by primed symbols such as its density  $\rho'$ .

Let us now consider small deformations or displacements  $\mathbf{u}(x,y,z)$  of the interface from its equilibrium position  $z = 0$ . The strain resulting from such a displacement is given by the symmetric strain tensor [Sneddon and Berry 1958]

$$u_{ij} = \frac{1}{2} \left( \frac{\partial u_i}{\partial x_j} + \frac{\partial u_j}{\partial x_i} \right). \quad (3.2)$$

This strain is related to the elastic stress  $\mathbf{T}_e$  by a generalized Hooke’s law

$$T_{ij,e} = \sum_{kl} C_{kl,e}^{ij} u_{kl}, \quad (3.3)$$

where  $C_{kl,e}^{ij}$  is the elastic modulus tensor which has at most 21 independent elements. The elastic free energy density per unit volume of this deformation is given by

$$W_e = \frac{1}{2} \sum_{ijkl} C_{kl,e}^{ij} u_{ij} u_{kl}, \quad (3.4)$$

and the stress tensor is related to the free energy density by

$$T_{ij,e} = \frac{1}{2} \left( \frac{\partial}{\partial u_{ij}} + \frac{\partial}{\partial u_{ji}} \right) W_e . \quad (3.5)$$

When the deformation  $\mathbf{u}$  is time-dependent, one needs to include viscous effects due to the energy dissipation on the interface. Generalizing Newton's law, we have a viscous stress  $\mathbf{T}_v$  proportional to the rate of the deformation

$$T_{ij,v} = \sum_{kl} C_{kl,v}^{ij} \frac{\partial}{\partial t} u_{kl} , \quad (3.6)$$

where the subscript 'v' denotes viscous contributions. For a harmonically varying deformation with angular frequency  $\omega$ , the time derivative can be replaced by  $-i\omega$ , using the associated complex notation for each quantity<sup>†</sup> ;

$$T_{ij,v} = \sum_{kl} \left\{ -i\omega C_{kl,v}^{ij} u_{kl} \right\} . \quad (3.7)$$

The generalized viscoelastic effects can be represented by the viscoelastic stress  $\mathbf{T}$  given by

$$T_{ij} = \sum_{kl} C_{kl}^{ij} u_{kl} , \quad (3.8)$$

where  $\mathbf{C}$  is the viscoelastic modulus tensor. The expression for  $\mathbf{C}$  in terms of  $C_{kl,e}^{ij}$  and  $C_{kl,v}^{ij}$  depends on how the elastic and viscous contributions are combined [Bland 1960]. Appendix A of this chapter shows two models for combining an ideal elastic element, a spring, and an ideal viscous element, a dashpot using a parallel combination (Voigt element) and a series one (Maxwell element). For a Voigt element one finds

$$C_{kl}^{ij} = C_{kl,e}^{ij} - i\omega C_{kl,v}^{ij} , \quad (3.9)$$

and for a Maxwell element

---

<sup>†</sup> Unless otherwise specified we will use complex notation.

$$C_{kl}^{ij} = \left[ \frac{1}{C_{kl,e}^{ij}} - \frac{1}{i\omega C_{kl,v}^{ij}} \right]^{-1}. \quad (3.10)$$

In either case, the viscoelastic modulus tensor can be decomposed into real and imaginary parts

$$C_{kl}^{ij} = C_{kl0}^{ij} - i\omega C_{kl1}^{ij}, \quad (3.11)$$

where  $C_{kl0}^{ij}$  and  $C_{kl1}^{ij}$  are called dynamic elasticity and viscosity coefficients, respectively.  $C_{kl0}^{ij}$  and  $C_{kl1}^{ij}$  present components of the stress in and out of phase with the strain, respectively [Ferry 1961]. Note that, in contrast to the Voigt element, the real and imaginary parts of  $C_{kl}^{ij}$  for a Maxwell element are not equal to  $C_{kl,e}^{ij}$  and  $-\omega C_{kl,v}^{ij}$ , respectively.  $C_{kl0}^{ij}$  and  $C_{kl1}^{ij}$  can also be functions of frequency even when  $C_{kl,e}^{ij}$  and  $C_{kl,v}^{ij}$  are constants.

If the film has a hexagonal symmetry along the  $z$ -axis,<sup>†</sup> there are symmetry relations between the elements of  $C_{kl}^{ij}$

$$C_{xx}^{xx} = C_{yy}^{yy}, \quad C_{xx}^{xx} - C_{yy}^{yy} = 2C_{xy}^{xy}, \quad C_{xy}^{xx} = 0. \quad (3.12)$$

which leaves only five independent elements in the viscoelastic modulus tensor. The viscoelastic free energy density of this film can be written in the form [Kramer 1971; Landau 1986]

$$W = \frac{1}{2} \sum_{ijkl} C_{kl}^{ij} u_{ij} u_{kl} \quad (3.13)$$

$$\begin{aligned} &= \frac{1}{2} C_{xx}^{xx} (u_{xx} + u_{yy})^2 + \frac{1}{2} C_{zz}^{zz} u_{zz}^2 + C_{xx}^{zz} (u_{xx} + u_{yy}) u_{zz} \\ &\quad + 2C_{xz}^{xz} (u_{xz}^2 + u_{yz}^2) + 2C_{xy}^{xy} (u_{xy}^2 - u_{xx} u_{yy}). \end{aligned} \quad (3.14)$$

For a description of the waves on a film whose thickness  $d$  is much smaller than the wavelength (see Eq. 3.1), the  $z$ -dependence of  $\mathbf{u}$  can be neglected as [Goodrich 1961]

---

<sup>†</sup> If the interface is covered with surfactant molecules which are tilted from the normal, the film may be anisotropic. However, if the wavelength of the interfacial wave is longer than the correlation length of the crystalline islands of surfactants, we may consider the film to be isotropic.

$$\mathbf{u} = \mathbf{u}(x, y, z=0, t), \quad (3.15)$$

and

$$u_{zz} = 0, \quad u_{xz} = \frac{1}{2} \frac{\partial u_z}{\partial x}, \quad u_{yz} = \frac{1}{2} \frac{\partial u_z}{\partial y}. \quad (3.16)$$

The viscoelastic free energy per unit *area* of the equivalent interface with zero-thickness becomes

$$\begin{aligned} \mathcal{W} &\equiv \lim_{d \rightarrow 0} Wd \\ &= \frac{1}{2} \mathcal{C}_{xx}^{xx} (u_{xx} + u_{yy})^2 + 2 \mathcal{C}_{xy}^{xy} (u_{xy}^2 - u_{xx}u_{yy}) + \frac{1}{2} \mathcal{C}_{xz}^{xz} \left[ \left( \frac{\partial u_z}{\partial x} \right)^2 + \left( \frac{\partial u_z}{\partial y} \right)^2 \right], \end{aligned} \quad (3.17)$$

where  $C_{kl}^{ij}$  is the viscoelastic modulus of the equivalent interface defined by

$$\mathcal{C}_{kl}^{ij} \equiv \lim_{d \rightarrow 0} C_{kl}^{ij} d. \quad (3.18)$$

It can be shown that the remaining three elements in Eq. (3.17) are given by

$$\mathcal{C}_{xx}^{xx} = K + G, \quad \mathcal{C}_{xy}^{xy} = G, \quad \mathcal{C}_{xz}^{xz} = \sigma, \quad (3.19)$$

where  $K$ ,  $G$  and  $\sigma$  are the lateral compression modulus, the lateral shear modulus and the interfacial tension, respectively (see Appendix B). Then Eq. (3.17) can be rewritten as

$$\mathcal{W} = \frac{K+G}{2} (u_{xx} + u_{yy})^2 + 2G(u_{xy}^2 - u_{xx}u_{yy}) + \frac{\sigma}{2} \left[ \left( \frac{\partial u_z}{\partial x} \right)^2 + \left( \frac{\partial u_z}{\partial y} \right)^2 \right]. \quad (3.20)$$

### §3.2 Interfacial boundary conditions

Since we are mainly concerned with interfacial waves, the motion of fluids is confined to the interface and the velocities of the fluids at the top and bottom walls of the container are zero,

$$\mathbf{v} \Big|_{z=\pm L/2} \approx \mathbf{v} \Big|_{z=\pm\infty} = 0. \quad (3.21)$$

The second boundary condition is that the two fluids and the interface remain in contact during the motion,<sup>†</sup>

$$\mathbf{v}|_{z=u_z} = \mathbf{v}'|_{z=u_z} = \frac{D\mathbf{u}}{Dt}, \quad (3.22)$$

where

$$\frac{D}{Dt} = \frac{\partial}{\partial t} + \mathbf{v} \cdot \nabla \quad (3.23)$$

represents the hydrodynamic derivative. If, for a given interfacial wave, the amplitude is much smaller than the wavelength, Eq. (3.22), to first order in  $u_z$ , reduces to

$$\mathbf{v}|_{z=0} = \mathbf{v}'|_{z=0} = \frac{\partial \mathbf{u}}{\partial t}, \quad (3.24)$$

where we have dropped the second-order term  $\mathbf{v} \cdot \nabla \mathbf{u}$  and taken  $u_z = 0$ .

The third boundary condition is from the result of the condition that the net force exerted on the interface must be zero. Forces exerted on the interface are due to 1) the stresses from the two fluids and 2) the deformation of the interface. The stress tensor  $\mathbf{s}$  of a viscous fluid is given by [Landau and Lifshitz 1959]

$$s_{ij} = -\delta_{ij} p + \delta_{ij} \left( \kappa_B - \frac{2}{3} \eta \right) \nabla \cdot \mathbf{v} + \eta \left( \frac{\partial v_i}{\partial x_j} + \frac{\partial v_j}{\partial x_i} \right), \quad (3.25)$$

where the fluid density  $\rho$ , velocity  $\mathbf{v}$ , and pressure  $p$  are generally functions of position and time, and  $\kappa_B$  and  $\eta$  are respectively the coefficients of bulk and shear viscosity, assumed to be constants for a given substance. The force  $\mathbf{P}$  acting on a unit interface area by the lower fluid is

$$\mathbf{P} = -\mathbf{s}|_{z=u_z} \cdot \mathbf{n}. \quad (3.26)$$

where  $\mathbf{n}$  is the upward normal to the interface  $z = u_z(\mathbf{r}, t)$ . For a small deformation  $u_z$ , we

---

<sup>†</sup> This is a stick boundary condition; the treatment of the slip boundary condition can be found in the literature [Bedeaux and Oppenheim 1978].

can neglect the deviation of  $\mathbf{n}$  from the unit vector along the  $z$ -axis

$$\mathbf{n} \approx \hat{\mathbf{z}}, \quad (3.27)$$

and the forces normal and tangential to the interface act vertically and horizontally to the equilibrium plane  $z = 0$ , respectively. Then,

$$\mathbf{P} \approx -\mathbf{s}\big|_{z=u_z} \cdot \hat{\mathbf{z}} \approx -\mathbf{s}\big|_{z=0} \cdot \hat{\mathbf{z}} - \rho g u_z \hat{\mathbf{z}}. \quad (3.28)$$

where the term  $-\rho g u_z \hat{\mathbf{z}}$  is the gravitational pressure due to the lower fluid displaced vertically by the amount  $u_z$ . Similarly the force exerted by the upper fluid is given by

$$\mathbf{P}' = -\mathbf{s}'\big|_{z=u_z} \cdot \mathbf{n}' \approx \mathbf{s}'\big|_{z=0} \cdot \hat{\mathbf{z}} + \rho' g u_z \hat{\mathbf{z}}, \quad (3.29)$$

since  $\mathbf{n}' = -\mathbf{n}$ .

The force  $\mathbf{P}^i$  exerted on a unit area of the interface by the surrounding interface is given by the divergence of the stress of the interface

$$\mathbf{P}^i = \nabla \cdot \mathcal{T}, \quad (3.30)$$

where  $\mathcal{T}$  is defined by

$$\mathcal{T} \equiv \lim_{d \rightarrow 0} \mathbf{T} d, \quad (3.31)$$

with  $\mathbf{T}$  the viscoelastic stress of the film with thickness  $d$ . Since  $\mathbf{T}$  can be given by

$$T_{ij} = \frac{1}{2} \left( \frac{\partial}{\partial u_{ij}} + \frac{\partial}{\partial u_{ji}} \right) W, \quad (3.32)$$

where  $W$  is the free energy density, we have

$$\mathcal{T}_{ij} = \frac{1}{2} \left( \frac{\partial}{\partial u_{ij}} + \frac{\partial}{\partial u_{ji}} \right) \mathcal{W}, \quad (3.33)$$

and in matrix form

$$\mathcal{F} = \begin{pmatrix} (K+G)u_{xx} + (K-G)u_{yy} & 2Gu_{xy} & \sigma \frac{\partial u_z}{\partial x} \\ 2Gu_{xy} & (K+G)u_{yy} + (K-G)u_{xx} & \sigma \frac{\partial u_z}{\partial y} \\ \sigma \frac{\partial u_z}{\partial x} & \sigma \frac{\partial u_z}{\partial y} & 0 \end{pmatrix}. \quad (3.34)$$

Taking the divergence of this equation and decomposing the resulting  $\mathbf{P}^i$  into tangential and normal components, one obtains

$$\mathbf{P}_t^i = (K + G) \nabla_t (\nabla_t \bullet \mathbf{u}_t) - G \nabla_t \times \nabla_t \times \mathbf{u}_t, \quad (3.35)$$

$$\mathbf{P}_z^i = \sigma \nabla_t^2 u_z \hat{\mathbf{z}}, \quad (3.36)$$

where

$$\mathbf{u}_t = u_x \hat{\mathbf{x}} + u_y \hat{\mathbf{y}}, \quad (3.37)$$

$$\nabla_t = \hat{\mathbf{x}} \frac{\partial}{\partial x} + \hat{\mathbf{y}} \frac{\partial}{\partial y}, \quad (3.38)$$

and we have used the vector identity

$$\nabla^2 \mathbf{u}_t = \nabla (\nabla \bullet \mathbf{u}_t) - \nabla \times \nabla \times \mathbf{u}_t. \quad (3.39)$$

Note that Eq. (3.36) is the Laplace-Young equation which relates the capillary pressure across an interface to the curvature of the interface.

So far we have only considered forces resulting from a deformation of a clean interface. If the interfacial region is composed of surfactant molecules, which usually lowers the interfacial tension, the interfacial tension is a function of the concentration of surfactant molecules,  $\gamma$ . If  $\gamma$  varies along the interface, there is an additional tangential force due to the resulting variation of interfacial tension,  $\nabla_t \sigma$ , which can be rewritten as

$$\nabla_t \sigma = \frac{\partial \sigma}{\partial \gamma} \nabla_t \gamma. \quad (3.40)$$

Let us now relate the variation of the surfactant concentration to the interfacial wave. The dilational modulus due to the variation of the interfacial area  $A$  is defined by

$$E_{\sigma} \equiv A \frac{\partial \sigma}{\partial A} = -\gamma \frac{\partial \sigma}{\partial \gamma} = \gamma \frac{\partial \Pi}{\partial \gamma}, \quad (3.41)$$

with  $\Pi$  the surface pressure which is the decrease in the tension of an interface with surfactants from that of a clean interface. Then, Eq. (3.40) can be rewritten as

$$\nabla_t \sigma = -\frac{E_{\sigma}}{\gamma} \nabla_t \gamma. \quad (3.42)$$

The equation for the conservation of surfactant molecules at a planar interface is [Levich 1962]

$$\frac{\partial \gamma}{\partial t} + \nabla_t \bullet (\gamma \mathbf{v}) \Big|_{z=0} = 0, \quad (3.43)$$

where we have neglected the mass flux per unit area between the interface and the bulk fluids as in the case of an insoluble surfactant. For small-amplitude fluctuations, the surfactant concentration can be written as

$$\gamma = \gamma_0 + \delta\gamma, \quad (3.44)$$

where  $\gamma_0$  and  $\delta\gamma$  are the equilibrium concentration and the variation from it, respectively. Then Eq. (3.43), using the boundary condition (3.24), becomes

$$\frac{\partial \delta\gamma}{\partial t} = -\gamma_0 \nabla_t \bullet \mathbf{v} \Big|_{z=0} = -\gamma_0 \frac{\partial}{\partial t} \nabla_t \bullet \mathbf{u}_t. \quad (3.45)$$

Integrating this equation with respect to time and using the condition that  $\delta\gamma$  is zero when  $\mathbf{u} = 0$ , we have

$$\delta\gamma = -\gamma_0 \nabla_t \bullet \mathbf{u}_t. \quad (3.46)$$

Hence, in terms of the deformation  $\mathbf{u}$ , the tangential force  $\nabla_t \sigma$  is given by

$$\nabla_t \sigma \approx -\frac{E_{\sigma}}{\gamma_0} \nabla_t \delta\gamma = E_{\sigma} \nabla_t (\nabla_t \bullet \mathbf{u}_t). \quad (3.47)$$

The total tangential force from the deformation of the interface is given by the sum of the forces in Eqs. (3.35) and (3.47),

$$\mathbf{P}_t^i = \mathcal{E} \nabla_t (\nabla_t \bullet \mathbf{u}_t) - G \nabla_t \times \nabla_t \times \mathbf{u}_t, \quad (3.48)$$

where

$$\mathcal{E} \equiv K + G + \mathcal{E}_\sigma \quad (3.49)$$

is the (total) dilational modulus.<sup>†</sup> Hence, the boundary condition of matching forces is given by

$$\boxed{-\Delta \mathbf{s} \Big|_{z=0} \bullet \hat{\mathbf{z}} + \mathcal{E} \nabla_t (\nabla_t \bullet \mathbf{u}_t) - G \nabla_t \times \nabla_t \times \mathbf{u}_t + \{ \sigma \nabla_t^2 - \Delta \rho g \} u_z \hat{\mathbf{z}} = 0,} \quad (3.50)$$

where  $\Delta \mathbf{s} = \mathbf{s} - \mathbf{s}'$  and  $\Delta \rho = \rho - \rho'$ .

In conclusion, the problem of describing the two-fluid system with inhomogeneous interfacial region is reduced to the set of boundary conditions for an equivalent mathematical interface with complex viscoelastic properties. In the following sections of this chapter, we will discuss fluctuations on this equivalent interface.

### §3.3 Interfacial waves

In 1847 Stokes treated undamped gravity waves (long-wavelength surface waves with gravity acting as the restoring force) at a free surface of an inviscid liquid [Stokes 1847]. Later the effect of the surface tension was included by Kelvin to describe short wavelength capillary waves [Kelvin 1871]. By adding the effect of bulk shear viscosity on surface waves, Lamb [Lamb 1932] and Levich [Levich 1962] completed the theory of the

---

<sup>†</sup> For an interface covered with an insoluble surfactant, the term  $(K + G)$  is negligible compared to  $\mathcal{E}_\sigma$ . Then  $\mathcal{E}$  measured in a surface light scattering experiment is equal to  $\mathcal{E}_\sigma$  calculated from Eq. (3.44). However, it is possible that  $\mathcal{E}$  differs from  $\mathcal{E}_\sigma$  in particular for an interface covered with a soluble surfactant [Mayer 1969].

clean zero-thickness surface of a single liquid [Stone and Rice 1977]. Waves on a clean interface between two viscid fluids were treated by Bellman and Pennington [Bellman and Pennington 1954]. When the interface is covered with a surfactant layer, one needs to extend the description by introducing additional viscoelastic properties of the interface through boundary conditions discussed in the previous section. In this section, we summarize the description of waves at an interface covered with an insoluble surfactant.

The spatial and temporal variations of a fluid system are governed by the hydrodynamic equations of motion which consist of three balance equations for the mass, momentum and energy of the system [Landau and Lifshitz 1959]. To describe interfacial waves one needs the mass and momentum balance equations,

$$\frac{\partial \rho}{\partial t} - \nabla \bullet (\rho \mathbf{v}) = 0, \quad (3.51)$$

$$\rho \left[ \frac{\partial \mathbf{v}}{\partial t} + (\mathbf{v} \bullet \nabla) \mathbf{v} \right] + \nabla p - \eta \nabla^2 \mathbf{v} - \left( \kappa_B + \frac{1}{3} \eta \right) \nabla (\nabla \bullet \mathbf{v}) = \rho \mathbf{g}. \quad (3.52)$$

For motion of small amplitude, one can linearize the momentum balance equation by dropping the second order term  $(\mathbf{v} \bullet \nabla) \mathbf{v}$ . If the velocity is much smaller than that of the adiabatic sound wave, the fluid can be considered as incompressible, and the hydrodynamic equations simplify to

$$\nabla \bullet \mathbf{v} = 0, \quad (3.53)$$

$$\rho \frac{\partial \mathbf{v}}{\partial t} + \nabla p - \eta \nabla^2 \mathbf{v} = \rho \mathbf{g}, \quad (3.54)$$

where  $\mathbf{g}$  is the gravitational acceleration.

Let us consider the case that the upper fluid is a vapor whose density and viscosity are negligible. For simplicity, motion of the interface is restricted to the  $xz$ -plane. Neglecting any  $y$ -dependence, the viscoelastic free energy density simplifies to

$$\mathcal{W} = \frac{\mathcal{E}}{2} \left( \frac{\partial u_x}{\partial x} \right)^2 + \frac{\sigma}{2} \left( \frac{\partial u_z}{\partial x} \right)^2 . \quad (3.55)$$

This implies that only two viscoelastic moduli  $\mathcal{E}$  and  $\sigma$  are necessary to describe the motion.

These moduli can be decomposed as

$$\mathcal{E} = \mathcal{E}_0(\omega) - i\omega \kappa(\omega), \quad (3.56)$$

$$\sigma = \sigma_0(\omega) - i\omega \mu(\omega), \quad (3.57)$$

where  $\kappa$  and  $\mu$  are the dilational and transverse surface viscosity, respectively [Langevin and Greismar 1980] (see Eq. 3.11). Boundary condition (3.50) simplifies to

$$p \Big|_{z=0} - 2\eta \left. \frac{\partial v_z}{\partial z} \right|_{z=0} + \sigma \frac{\partial^2 u_z}{\partial x^2} - \rho g u_z = 0 , \quad (3.58)$$

$$- \eta \left( \left. \frac{\partial v_x}{\partial z} \right|_{z=0} + \left. \frac{\partial v_z}{\partial x} \right|_{z=0} \right) + \mathcal{E} \frac{\partial^2 u_x}{\partial x^2} = 0 , \quad (3.59)$$

in the  $x$ - and  $z$ - coordinates, respectively, where we have substituted Eq. (3.25).

For harmonic plane-wave motion, the velocity of the lower fluid is of the form

$$\mathbf{v}(x,z,t) = a(z) e^{iQx - i\Omega t} , \quad (3.60)$$

where  $a(z)$ ,  $Q$  and  $\Omega$  are the amplitude, the complex wavevector and the angular frequency, respectively.  $Q$  and  $\Omega$  can be split into real and imaginary parts

$$Q = q + i\Gamma, \quad (3.61)$$

$$\Omega = \omega - i\beta, \quad (3.62)$$

where the imaginary parts  $\Gamma$  and  $\beta$  are the spatial and temporal damping coefficients of the wave motion, respectively.

Substituting Eq. (3.60) into the linearized hydrodynamic equations (3.53) and (3.54), and using boundary condition (3.21), the solution for harmonic plane-wave motion  $\mathbf{v}$  is given by [Levich 1962]

$$v_x = [ -iQAe^{Qz} + MB e^{Mz} ] e^{iQx - i\Omega t} , \quad (3.63)$$

$$v_z = [ -QAe^{Qz} - iQB e^{Mz} ] e^{iQx - i\Omega t} , \quad (3.64)$$

with

$$M = \sqrt[+]{Q^2 - \frac{i\Omega\rho}{\eta}} , \quad (3.65)$$

where the plus sign indicates the root with a positive real part, and  $Q$  has a positive real part also. The vertical and horizontal displacements can be obtained from boundary condition (3.24), by integrating Eqs. (3.63) and (3.64),

$$u_x = \frac{iQA - MB}{i\Omega} e^{iQx - i\Omega t} , \quad (3.66)$$

$$u_z = \frac{QA + iQB}{i\Omega} e^{iQx - i\Omega t} . \quad (3.67)$$

The boundary conditions, (3.58) and (3.59), give a pair of equations for  $A$  and  $B$

$$\begin{cases} [\Omega^2\rho + 2i\eta Q^2\Omega - \rho\Omega_o^2]A + i[2i\eta Q\Omega M - \rho\Omega_o^2]B = 0 \\ [-2\eta\Omega Q^2 + iEQ^3]A - [(2i\eta Q^2 + \Omega\rho)\Omega + EQ^2M]B = 0 \end{cases} ,$$

(3.68)

where

$$\Omega_o = \sqrt[+]{gQ + \frac{\sigma}{\rho}Q^3} , \quad (3.69)$$

which is the dispersion equation of Kelvin for a clean surface. For a non-trivial solution for  $A$  and  $B$ , the determinant of the coefficients in Eq. (3.68) must be zero. This yields the dispersion equation

$$D(Q, \Omega; \rho, \eta, \sigma, \epsilon) = \{EQ^2 - i\Omega\eta(Q + M)\} \{\rho\Omega_0^2 - i\Omega\eta Q(Q + M) - \rho\Omega^2\} + \Omega^2\eta^2 Q(Q - M)^2 = 0. \quad (3.70)$$

Since this is a third order equation in  $\Omega$ , for a given complex wavevector  $Q$  there are three solutions for  $\Omega$  that satisfy the dispersion equation. The general solutions for interfacial waves should therefore consist of a superposition of these solutions. For the vertical displacement, for example, this reads

$$u_z = \sum_v \frac{A_v + iB_v}{i\Omega_v} Q e^{iQx - i\Omega_v t}. \quad (3.71)$$

### §3.4 Power spectrum of interfacial waves

The frequency spectrum of light scattered from an interfacial wave is given by the power spectrum of the interfacial fluctuations (see Eq. 2.38). An interfacial wave represented by

$$u_z = u_{z0} e^{iqx - i\omega t - \beta t} \quad \text{for } t > 0, \quad (3.72)$$

gives rise to a Lorentzian peak at angular frequency  $\omega$  with FWHM of  $2\beta$ . If the wave is produced by thermal motion of molecules, we need to consider the statistical average of possible modes for a given wavevector (see Eq. 3.71) in order to obtain the interfacial power spectrum. Let us devote this section to the calculation of the power spectrum of thermally induced interfacial fluctuations, especially capillary waves.

There are several ways of calculating the power spectrum of hydrodynamic fluctuations: 1) linear response theory, using the fluctuation-dissipation theorem which relates the mean square fluctuations in the excitation amplitude to the imaginary part of an appropriately defined response function [Bouchiat and Meunier 1971a; Loudon 1984], 2)

straight forward calculation using the solution of the hydrodynamic equations [Bouchiat and Meunier 1971a], and 3) fluctuating hydrodynamics approach [Landau and Lifshitz 1959; Lifshitz and Pitaevskii 1980; Grant and Desai 1983]. The method of linear response theory will not be discussed here since it is well established and reviewed in the literature [Cottam and Maradudin 1984]. The second method will be discussed in detail in this section using the result of the previous section, and the third method of fluctuating hydrodynamics will be used in the next chapter to consider nonequilibrium fluctuations.

Bouchiat and Meunier first derived the power spectrum of thermal fluctuations of a clean liquid-vapor surface [Bouchiat and Meunier 1971a]. Later they extended it to the case of monolayer-covered liquid surfaces by adding extra terms in the boundary conditions [Langevin 1981]. Let us first consider the case in which the dilational modulus  $\mathcal{E}$  can be neglected. In this case the dispersion equation (3.70) has two non-zero roots

$$\Omega_{\pm} = \pm \omega_R - i\beta_R, \quad (3.73)$$

for a given real wavevector  $q$ . With an (arbitrary) initial condition of

$$v_{zq}(z, t=0) = 0, \quad (3.74)$$

the Fourier transform of the vertical displacement is given by substituting Eq. (3.73) into Eq. (3.71),

$$u_{zq}(t) = \frac{u_{zq}(0)}{\Omega_+ - \Omega_-} \left[ \Omega_+ e^{-i\Omega_- t} - \Omega_- e^{-i\Omega_+ t} \right] \quad \text{for } t > 0, \quad (3.75)$$

where the subscript ‘ $q$ ’ denotes the Fourier amplitude for a wavevector  $q$ . Note that the wavevectors in the power spectrum measurements are real quantities determined by a scattering geometry. Using the fact that the correlation function is an even function of time, the power spectrum is given by

$$P_{u_{zq}}(\omega) = \int_{-\infty}^{\infty} \langle u_{zq}^*(0) u_{zq}(\tau) \rangle e^{i\omega\tau} d\tau \quad (3.76)$$

$$= 2 \int_0^{\infty} \langle u_{zq}^*(0) u_{zq}(\tau) \rangle \cos \omega \tau d\tau . \quad (3.77)$$

Substituting  $u_{zq}$  of Eq. (3.75), one obtains the power spectrum of a damped harmonic oscillator [Bouchiat and Meunier 1971a]

$$P_{u_{zq}}(\omega) = \langle |u_{zq}(0)|^2 \rangle \frac{4\beta_R(\omega_R^2 + \beta_R^2)}{[\omega^2 - (\omega_R^2 + \beta_R^2)]^2 + 4\beta_R^2\omega^2} . \quad (3.78)$$

Let us now calculate the ensemble averages of the displacements of the interface in the above equation. For a deformation of the interface in the  $xz$ -plane with wavevector  $q$

$$\mathbf{u}^R(x,t) = \mathbf{u}_0^R \cos[qx - \phi(t)] = \text{Re}[\mathbf{u}_0(t) e^{iqx}] , \quad (3.79)$$

where

$$\mathbf{u}_0(t) = \mathbf{u}_0^R e^{-i\phi(t)} , \quad (3.80)$$

the free energy density of Eq. (3.20), including the gravity term, becomes

$$\mathcal{W} = \frac{1}{2} [\mathcal{E}q^2 u_{xo}^2 + \sigma q^2 u_{zo}^2] \sin^2 qx + \frac{\rho g}{2} u_{zo}^2 \cos^2 qx , \quad (3.81)$$

where  $u_{xo}$  and  $u_{zo}$  are real amplitudes of horizontal and vertical displacements, respectively.

Integration of  $\mathcal{W}$  over the interface area  $L^2$  yields

$$\int_{-L/2}^{L/2} \int_{-L/2}^{L/2} \mathcal{W} dx dy = \frac{L^2}{4} [\mathcal{E}q^2 u_{xo}^2 + (\sigma q^2 + \rho g) u_{zo}^2] , \quad (3.82)$$

where  $L$  is the dimension of the system. Therefore, the ensemble averages of the vertical and horizontal displacements with wavevector  $q$  are given by [Mandelstam 1913; Vrij 1968]

$$\langle u_z(x,t)^2 \rangle_q = \frac{1}{2} \langle u_{zo}^2 \rangle_q = \frac{k_B T}{(\sigma q^2 + \rho g) L^2} , \quad (3.83)$$

$$\langle u_x(x,t)^2 \rangle_q = \frac{1}{2} \langle u_{xo}^2 \rangle_q = \frac{k_B T}{\mathcal{E} q^2 L^2} , \quad (3.84)$$

$$\langle u_z(t) u_x(t) \rangle_q = 0 . \quad (3.85)$$

The average corrugation of an interface due to thermal motion of fluid molecules can be given by the root mean square of a summation of Eq. (3.83) over all wavevectors [Herpin and Meunier 1974]

$$\langle u_z(x,t)^2 \rangle = \int_0^{q_{max}} \langle u_z(x,t)^2 \rangle_q n(q) dq \approx \frac{k_B T}{4\pi\sigma} \ln \frac{\sigma q_{max}^2}{\rho g}, \quad (3.86)$$

where  $n(q)$  is the density of states with wavevector  $q$  and  $q_{max}$  is the maximum allowed wavevector corresponding to the mean separation between molecules in the fluid. The rms amplitude of surface waves at the air/water interface at room temperature is about 4 Å with the value of  $q_{max} \approx 10^8 \text{ cm}^{-1}$ .

In terms of the Fourier amplitudes of the associated complex quantities, the above equations become

$$\langle |u_{zq}(t)|^2 \rangle = 2 \langle u_z(x,t)^2 \rangle_q L^2 = \frac{2k_B T}{\sigma q^2 + \rho g}, \quad (3.87)$$

$$\langle |u_{xq}(t)|^2 \rangle = 2 \langle u_x(x,t)^2 \rangle_q L^2 = \frac{2k_B T}{\rho g}, \quad (3.88)$$

$$\langle u_{zq}(t) u_{xq}^*(t) \rangle = 0. \quad (3.89)$$

Note that the minor differences between Eqs. (3.83) – (3.85) and Eqs. (3.87) – (3.89) which are often neglected in the literature. Substituting Eq. (3.87) into Eq. (3.78), one obtains the power spectrum of the vertical displacements  $u_z$

$$P_{u_z}(\omega) = \frac{2k_B T}{\sigma q^2 + \rho g} \frac{4\beta_R (\omega_R^2 + \beta_R^2)}{[\omega^2 - (\omega_R^2 + \beta_R^2)]^2 + 4\beta_R^2 \omega^2}. \quad (3.90)$$

When the damping is small ( $\beta_R \ll \omega_R$ ) [Levich 1962], the approximate solution of the dispersion equation is given by

$$\omega_R \approx \omega_c \equiv \sqrt{gq + \frac{\sigma}{\rho} q^3}, \quad (3.91)$$

$$\beta_R \approx \beta_c = \frac{2\eta q^2}{\rho}, \quad (3.92)$$

where  $\omega_c$  and  $\beta_c$  are the angular frequency and temporal damping coefficient of the capillary wave. The power spectrum of Eq. (3.90) becomes a usual Lorentzian with the narrow line approximation, which considers only the angular frequency around  $\omega_c$  ( $\omega \approx \omega_c$ ) as [Loudon 1984]

$$\begin{aligned} P_{u_z, q}(\omega) &\approx \frac{2qk_B T}{\rho\omega_c^2} \frac{4\beta_c \omega_c^2}{(\omega + \omega_c)^2 (\omega - \omega_c)^2 + 4\beta_c^2 \omega^2} \\ &\approx \frac{2qk_B T}{\rho} \frac{\beta_c}{(\omega - \omega_c)^2 + \beta_c^2}. \end{aligned} \quad (3.93)$$

Thus the peak frequency and width of a single spectrum provide the interfacial tension and bulk shear viscosity, respectively.

For the opposite extreme of large damping ( $\beta_R \gg \omega_R$ ), the dispersion equation has a single imaginary solution [Levich 1962]

$$\Omega \approx -i \frac{\omega_c^2}{\beta_c}, \quad (3.94)$$

and the power spectrum of this overdamped capillary wave is given by

$$P_{u_z, q}(\omega) = \frac{2qk_B T}{\rho\omega_c^2} \frac{\frac{\omega_c^2}{\beta_c}}{\omega^2 + \left(\frac{\omega_c^2}{\beta_c}\right)^2}, \quad (3.95)$$

which is also a Lorentzian centered at  $\omega = 0$ . The width of this Lorentzian gives only the relation between  $\sigma$  and  $\eta$ . If the width of the peak is measured for several wavevectors, the individual values for  $\sigma$  and  $\eta$  can be obtained by fitting values for the width as a function of the wavevector as given by Eq. (3.94).

Without the assumption of the harmonic time dependence as Eq. (3.72), Bouchiat and Meunier [Bouchiat and Meunier 1971a] looked for a general solution of hydrodynamic

equations in terms of the Laplace transformed components defined as<sup>†</sup>

$$\tilde{F}_q(\alpha) = \int_0^{\infty} e^{-\alpha t} F_q(t) dt. \quad (3.96)$$

Let us now consider a monolayer-covered interface and use the general solution of Bouchiat and Meunier. Since we are interested in the interfacial waves, let us neglect the gravity term in the *bulk* which depends only on  $z$ . This is equivalent to dropping the gravity term in the hydrodynamic equations but keeping the term in the boundary conditions. Then the hydrodynamic equations of motion in Fourier transformed components are

$$iqv_{xq} + \frac{\partial v_{zq}}{\partial z} = 0, \quad (3.97)$$

$$\rho \frac{\partial v_{xq}}{\partial t} = \eta \left( \frac{\partial^2}{\partial z^2} - q^2 \right) v_{xq} - iqp_q, \quad (3.98)$$

$$\rho \frac{\partial v_{zq}}{\partial t} = \eta \left( \frac{\partial^2}{\partial z^2} - q^2 \right) v_{zq} - \frac{\partial p_q}{\partial z}. \quad (3.99)$$

Eliminating  $v_{xq}$  and  $v_{zq}$ , the solution of  $p_q$  satisfying the boundary condition (3.58) is given by

$$p_q = e^{qz} \left[ (\rho g + \sigma q^2) u_{zq} + 2\eta \frac{\partial v_{zq}}{\partial z} \Big|_{z=0} \right]. \quad (3.100)$$

A Laplace transform of Eq. (3.99) yields

$$\begin{aligned} & \left[ \rho\alpha - \eta \left( \frac{\partial^2}{\partial z^2} - q^2 \right) \right] \tilde{v}_{zq}(z, \alpha) - \rho v_{zq}(z, t=0) = \\ & = -q e^{qz} \left[ (\rho g + \sigma q^2) \tilde{u}_{zq}(\alpha) + 2\eta \frac{\partial \tilde{v}_{zq}(z, \alpha)}{\partial z} \Big|_{z=0} \right]. \end{aligned} \quad (3.101)$$

---

<sup>†</sup> When  $\alpha = -i\omega$ , the Laplace transform is a one-sided Fourier transform which is used by Lifshitz and Pitaevskii [Lifshitz and Pitaevskii 1980] to calculate hydrodynamic fluctuations.

With the initial condition of Eq. (3.74), let us look for a solution of the type,

$$\tilde{v}_{zq}(z, \alpha) = f(\alpha) e^{qz} + h(\alpha) e^{m(\alpha)z}, \quad (3.102)$$

where

$$m(\alpha) = \sqrt[+]{q^2 + \frac{\alpha\rho}{\eta}}. \quad (3.103)$$

Substituting the expression for  $\tilde{v}_{zq}(z, \alpha)$  into Eq. (3.101), one gets

$$(\rho\alpha + 2\eta q^2) f(\alpha) + 2\eta q m h(\alpha) = -\rho\omega_c^2 \tilde{u}_{zq}(\alpha). \quad (3.104)$$

The boundary condition (3.59) provides the relation

$$2\eta q^2 f(\alpha) + \eta(m^2 + q^2) h(\alpha) = i \mathcal{E} q^3 \tilde{u}_{xq}(\alpha). \quad (3.105)$$

Substituting the following relations

$$\tilde{v}_{xq}(z=0, \alpha) = \alpha \tilde{u}_{xq}(\alpha) - u_{xq}(0), \quad (3.106)$$

$$\tilde{v}_{zq}(z=0, \alpha) = \alpha \tilde{u}_{zq}(\alpha) - u_{zq}(0), \quad (3.107)$$

into Eqs. (3.104) and (3.105), one obtains a set of equations for  $f(\alpha)$  and  $h(\alpha)$

$$[\rho\alpha^2 + 2\eta q^2\alpha + \rho\omega_c^2] f(\alpha) + [2\eta q m\alpha + \rho\omega_c^2] h(\alpha) = -\rho\omega_c^2 u_{zq}(0), \quad (3.108)$$

$$[2\eta q^2\alpha + \mathcal{E} q^3] f(\alpha) + [\eta(m^2 + q^2)\alpha + \mathcal{E} q^2 m] h(\alpha) = i \mathcal{E} q^3 u_{xq}(0). \quad (3.109)$$

Solving the above equations, the Laplace transform of the vertical displacement is given by

$$\tilde{u}_{zq}(\alpha) = \frac{1}{\alpha} \left\{ \left[ -\rho\omega_c^2 \frac{\eta\alpha(m+q) + \mathcal{E} q^2}{D(q, i\alpha)} + 1 \right] u_{zq}(0) - \frac{i\mathcal{E}\eta\alpha q^3(m-q)}{D(q, i\alpha)} u_{xq}(0) \right\}, \quad (3.110)$$

where  $D(q, i\alpha)$  is the dispersion equation (3.70). The power spectrum of the wave is then given by

$$P_{u_{zq}}(\omega) = \int_{-\infty}^{\infty} \langle u_{zq}^*(0) u_{zq}(\tau) \rangle e^{i\omega\tau} d\tau$$

$$\begin{aligned}
&= \left[ \langle \tilde{u}_{zq}(\alpha) u_{zq}^*(0) \rangle + \langle \tilde{u}_{zq}^*(\alpha) u_{zq}(0) \rangle \right]_{\alpha=-i\omega} \\
&= 2 \operatorname{Re} \left\{ \langle \tilde{u}_{zq}(\alpha) u_{zq}^*(0) \rangle \right\}_{\alpha=-i\omega} .
\end{aligned} \tag{3.111}$$

Substituting Eq. (3.110) into the above equation, one gets the power spectrum of capillary waves at the interface covered with a monolayer as

$$P_{u_{z,q}}(\omega) = \frac{4qk_B T}{\omega} \operatorname{Im} \left\{ \frac{-i\eta\omega[m(-i\omega)+q]+\mathcal{E}q^2}{D(q,\omega)} \right\} . \tag{3.112}$$

For a clean interface ( $\mathcal{E} = 0$ ), the above power spectrum becomes

$$P_{u_{z,q}}(\omega) = \frac{2qk_B T}{\rho\omega_c^2} \frac{4\beta\omega_c^2 \left( \frac{m}{q+m} \right)}{[\omega^2 - \omega_c^2]^2 + 4\omega^2\beta^2 \left( \frac{m}{q+m} \right)^2} . \tag{3.113}$$

This power spectrum is equivalent to the power spectrum of Eq. (3.93) or (3.95) when the damping is either very small ( $\beta_R \ll \omega_R$ ) or very large ( $\beta_R \gg \omega_R$ ), respectively. The discrepancy for intermediate damping can be explained in terms of the frequency dependent perturbation of interfacial waves which is associated with the transmission of motion from the surface to the bulk [Bouchiat and Meunier 1971b].

The detailed form of the spectrum Eq. (3.112) is determined by the viscoelastic moduli  $\sigma$  and  $\mathcal{E}$ . Thus it is possible to obtain the elastic and viscous parts of the two moduli from a single measured spectrum. This method requires fitting the power spectrum (or correlation function which is a Fourier transform of the power spectrum) with four parameters ( $\sigma_0$ ,  $\mu$ ,  $\mathcal{E}_0$  and  $\kappa$ ), after deconvoluting the instrumental function from the measured spectrum [Earnshaw, McGivern et al. 1990]. To show the general effect of viscoelasticity of an interface on the power spectrum, let us summarize the case of, for example, a water surface covered with a myristic acid monolayer [Byrne and Earnshaw 1979; Langevin and Greismar 1980]. The peak frequency of the spectrum is mainly

determined by  $\sigma_0$ , the elastic part of the interfacial tension. The transverse surface viscosity  $\mu$  and the dilational modulus  $\mathcal{E}$  modify the peak frequency values by about 10% at most. The width of the peak varies significantly depending on  $\mathcal{E}_0$ . A maximum in the width is expected and observed [Dorrestein 1951; Hansen and Mann 1964], which was attributed to the coupling between capillary and longitudinal surface waves [Lucassen-Reynders and Lucassen 1969]. The transverse surface viscosity  $\mu$  increases the width and shifts the position of the maximum of the width towards the lower  $\mathcal{E}_0/\sigma_0$  value. The effect of the surface dilational viscosity  $\kappa$  on the width is somewhat complicated but generally reduces the maximum width.

### §3.5 Appendices

#### §3.5.1 Viscoelasticity; a combination of elasticity and viscosity [Bland 1960]

Let us represent the elasticity and viscosity with an ideal spring and a dashpot, respectively. When a force is exerted on an ideal spring, the deformation of the spring is proportional to the force (Hooke's law)

$$F_e^R = C_e a_e^R, \quad (3.A1)$$

where  $F_e^R$ ,  $a_e^R$  and  $C_e$  are the force on the spring, the extension of the spring and the spring constant, respectively, and the superscript 'R' denotes a real quantity. For an ideal dashpot, the rate of extension is proportional to the applied force (Newton's law)

$$F_v^R = C_v \frac{\partial}{\partial t} a_v^R, \quad (3.A2)$$

where  $F_v^R$ ,  $a_v^R$  and  $C_v$  are the force on the dashpot, the extension of the dashpot and the

viscosity, respectively.

In analogy to the combination of a resistor and a capacitor, there are two possible ways of combining a spring and a dashpot: parallel and series combinations. In a parallel combination (Voigt element), the extensions of the spring and dashpot are the same and the total force is the sum of the forces exerted on the spring and dashpot,

$$a^R = a_e^R = a_v^R, \quad F^R = F_e^R + F_v^R. \quad (3.A3)$$

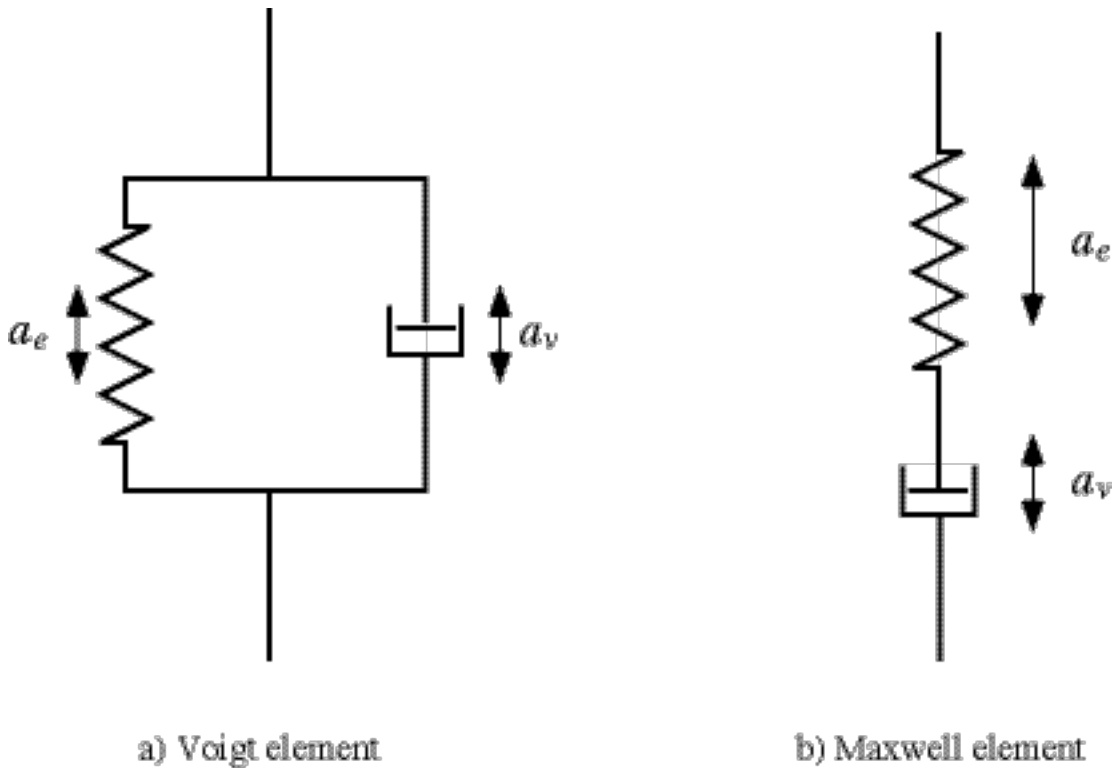


Fig. 3.1. A parallel combination (Voigt element) and a series combination (Maxwell element) of a spring and a dashpot.  $a_e$  and  $a_v$  are the extensions of the spring and the dashpot from equilibrium length, respectively.

For the combined unit, the relation between the total force and the extension is given by

$$F^R = (C_e + C_v \frac{\partial}{\partial t}) a^R. \quad (3.A4)$$

In a series combination (Maxwell element), the total extension is the sum of each extension of the spring and dashpot and the forces on the spring and dashpot are the same.

$$a^R = a_e^R + a_v^R, \quad FR = F_e^R = F_v^R. \quad (3.A5)$$

Thus the relation in this case is given by

$$\frac{\partial}{\partial t} a^R = \frac{1}{C_e} \frac{\partial}{\partial t} FR + \frac{1}{C_v} FR. \quad (3.A6)$$

For a harmonic force of angular frequency  $\omega$ , let us use complex notation of the associated complex quantity

$$a^R = \text{Re} [ a e^{-i\omega t} ], \quad FR = \text{Re} [ F e^{-i\omega t} ]. \quad (3.A7)$$

Then, the time derivative can be replaced by a number  $-i\omega$ , yielding force-extension relations respectively for the Voigt and the Maxwell elements,

$$F = [C_e - i\omega C_v] a, \quad (3.A8)$$

$$F = \left[ \frac{1}{C_e} - \frac{1}{i\omega C_v} \right]^{-1} a. \quad (3.A9)$$

Eqs. (3.9) and (3.10) are generalization of the above two relations for three dimensional case.

### §3.5.2 Viscoelastic moduli of an interface

When a uniform hydrostatic force per unit length  $\rho$  is applied laterally to an area  $A$  of the interface, the area will decrease by an amount of  $\delta A$  which can be found as

$$\delta A = A (u_{xx} + u_{yy}). \quad (3.A10)$$

The lateral compressional modulus,  $K$ , is defined by the generalized Hooke's law

$$\rho = K \frac{\delta A}{A} = K (u_{xx} + u_{yy}). \quad (3.A11)$$

Substituting the following relation between the lateral force per unit length and the lateral tensor

$$\rho = \lim_{d \rightarrow 0} T_{xx} d = \lim_{d \rightarrow 0} T_{yy} d, \quad (3.A12)$$

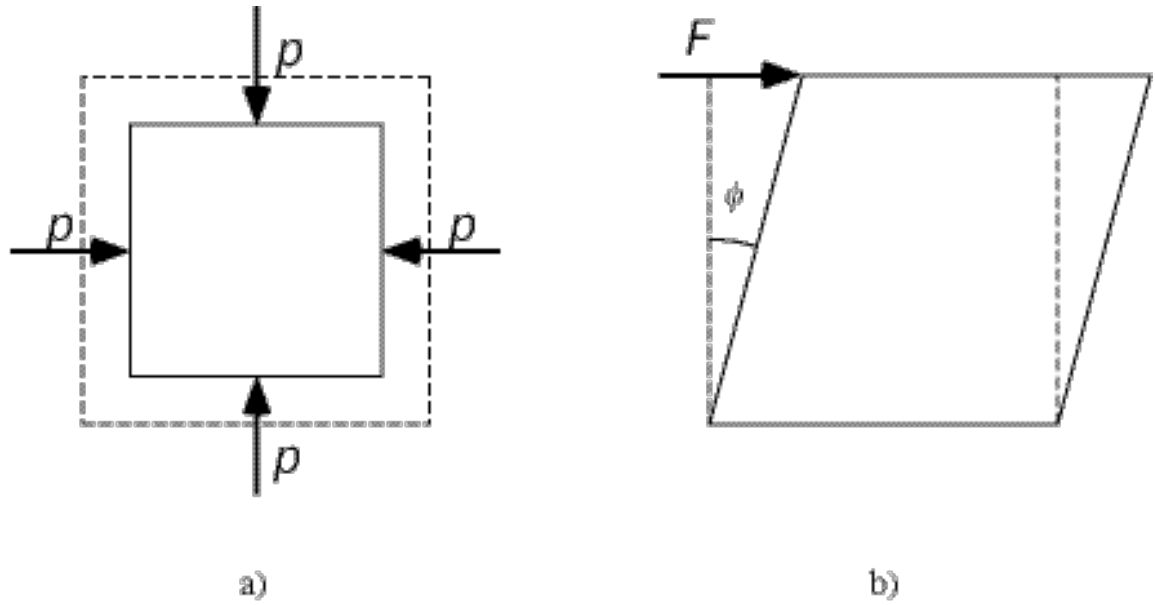


Fig. 3.2. Deformation of a square (dashed line) by (a) a hydrostatic force  $p(\rho)$  per unit length and (b) a shear force  $\mathcal{F}$  per unit length.  $\phi$  is the shear angle.

into Eq. (3.8), and making use of Eq. (3.12), we find

$$K (u_{xx} + u_{yy}) = \mathcal{C}_{yy}^{xx} (u_{xx} + u_{yy}) + 2 \mathcal{C}_{xy}^{xy} u_{xx}, \quad (3.A13)$$

$$K (u_{xx} + u_{yy}) = \mathcal{C}_{yy}^{xx} (u_{xx} + u_{yy}) + 2 \mathcal{C}_{xy}^{xy} u_{yy}. \quad (3.A14)$$

Adding Eqs. (3.A13) and (3.A14), the lateral compressional modulus is given by

$$K = \mathcal{C}_{yy}^{xx} + \mathcal{C}_{xy}^{xy}. \quad (3.A15)$$

Similarly considering a deformation of a square by a shearing force, one can identify [Sneddon and Berry 1958]

$$\mathcal{C}_{xy}^{xy} = G, \quad (3.A16)$$

where  $G$  is the lateral shear modulus defined by the ratio

$$G \equiv \frac{\mathcal{F}}{\phi}, \quad (3.A17)$$

where  $F$  is the shearing force per unit length applied to a side of the square and  $\phi$  is the resulting angle of shear. Using Eq. (3.12) again,  $\mathcal{C}_{xx}^{xx}$  can be written as the sum of the lateral compressional modulus and the lateral shear modulus of the interface

$$\mathcal{E}_{xx}^{xx} = K + G. \quad (3.A18)$$

If the deformation  $\mathbf{u}$  is small, the area  $A$  of a surface  $z = u_z(x,y)$  is given by

$$A = \int \left[ 1 + \left( \frac{\partial u_z}{\partial x} \right)^2 + \left( \frac{\partial u_z}{\partial y} \right)^2 \right]^{\frac{1}{2}} dx dy \approx \int \left[ 1 + \frac{1}{2} \left( \frac{\partial u_z}{\partial x} \right)^2 + \frac{1}{2} \left( \frac{\partial u_z}{\partial y} \right)^2 \right] dx dy. \quad (3.A19)$$

Thus the third term of Eq. (3.17) represents the free energy increase due to the deformation  $\mathbf{u}$  and we can identify

$$\mathcal{E}_{xz}^{xz} = \sigma, \quad (3.A20)$$

where  $\sigma$  is the interfacial tension.

## Chapter IV

### Spectral Asymmetry of the Light Scattered from a Nonequilibrium Liquid Interface

In the previous chapter we discussed the power spectrum of capillary waves caused by the thermal motion of liquid molecules in equilibrium. These waves give rise to a doublet in the spectrum of light scattered from the liquid interface. For a given scattering angle, each peak of the doublet corresponds to an interaction of the light (photons) with capillary waves (ripples) travelling in opposite directions. The intensity of each peak is proportional to the population of the ripples travelling in each direction;

$$I_{\pm} \sim n_{\pm}, \quad (4.1)$$

where  $I_+$  and  $I_-$  are the peak intensities of the up-shifted and down-shifted peaks, respectively, and  $n_+$  and  $n_-$  are the populations of the corresponding ripples travelling in opposite directions. In equilibrium, the up-shifted and down-shifted peaks have the same intensity, since the populations  $n_+$  and  $n_-$  are equal.

Out of equilibrium, however,  $n_+$  and  $n_-$  are no longer equal and the spectrum becomes asymmetric. In order to calculate the spectral asymmetry it is necessary to use nonequilibrium statistical mechanics. This was done in 1983 by Grant and Desai [Grant and Desai 1983; Desai and Grant 1986]. They derived the spectral asymmetry of capillary waves on a liquid surface in the presence of a small temperature gradient along the surface.

In this chapter we study the spectral asymmetry of light scattered from capillary waves on a nonequilibrium water surface, and compare the observed spectral asymmetry

with the theoretically predicted one.

#### §4.1 Basic considerations

Let us first use simple arguments [Chung, Lee *et al.* 1988] to derive an approximate expression for the asymmetry  $\Delta_c$  of the capillary wave peak intensities defined as<sup>†</sup>

$$\Delta_c \equiv \frac{I_- - I_+}{I_- + I_+} \approx \frac{n_- - n_+}{n_- + n_+} . \quad (4.2)$$

At high temperature  $T$ , the population  $n$  of capillary waves with angular frequency  $\omega_c$  is proportional to temperature,

$$n = \frac{k_B T}{\hbar \omega_c} , \quad (4.3)$$

with  $k_B$  and  $\hbar$  the Boltzmann and Planck constants, respectively. The population difference  $n_- - n_+$  can then be approximated by

$$n_- - n_+ = \frac{k_B}{\hbar \omega_c} 2\Delta T^* , \quad (4.4)$$

with  $\Delta T^*$  the ‘effective’ temperature difference for a capillary wave along its mean free path  $l_c$  which is the inverse of the spatial damping coefficient (see Fig. 4.1). Thus, if we write

$$\Delta T^* = l_c \hat{\mathbf{q}} \cdot \nabla T , \quad (4.5)$$

with  $\hat{\mathbf{q}}$  a unit vector along the wavevector of the capillary wave  $\mathbf{q}$ , the asymmetry  $\Delta_c$  becomes

$$\Delta_c \approx \frac{n_- - n_+}{2n} \approx \frac{l_c \hat{\mathbf{q}} \cdot \nabla T}{T} . \quad (4.6)$$

Defining the characteristic length scale of the temperature gradient as

---

<sup>†</sup> This definition of the asymmetry differs from that of Grant and Desai [Grant and Desai 1983] by a factor of two. Also, there is a minor difference from the asymmetry defined in terms of the integrated intensities [Fox, 1982].

$$L_{\nabla} \equiv [\hat{\mathbf{q}} \cdot \nabla \ln T]^{-1}, \quad (4.7)$$

we obtain

$$\Delta_c \approx \frac{l_c}{L_{\nabla}}. \quad (4.8)$$

Therefore, the asymmetry should be proportional to the ratio of the mean free path to the characteristic length of the temperature gradient.

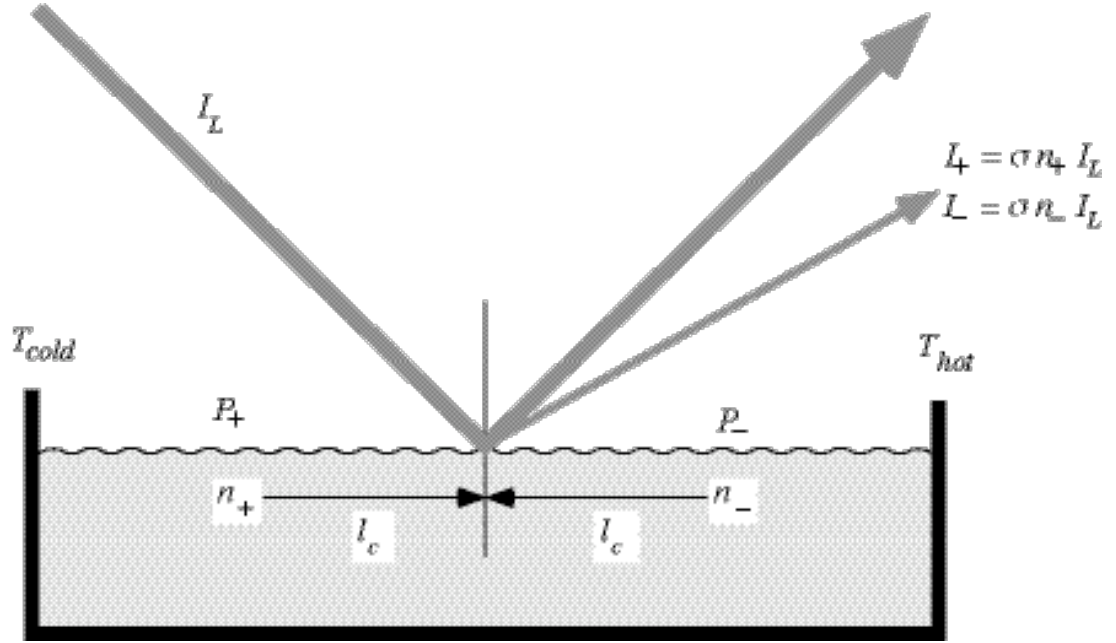


Fig. 4.1. Scattering of light from a nonequilibrium interface;  $I_L$  is the intensity of the incident light;  $S$  is the cross-section of the scattering process;  $I_+$  and  $I_-$  are the intensities of the light scattered from the capillary waves generated at positions  $x_+$  and  $x_-$  which are one mean free path,  $l_c$ , away from the probing points, respectively;  $n_+ = n(T_+)$  and  $n_- = n(T_-)$  are the populations of the capillary waves, where  $T_+$  and  $T_-$  are the temperatures at  $x_+$  and  $x_-$ , respectively. The scattered light intensity is given by the product of  $S n(T) I_L$ .

## §4.2 Fluctuating hydrodynamic theory

A more rigorous derivation of the asymmetry using fluctuating hydrodynamics was given by Grant and Desai [Grant and Desai 1983; Desai and Grant 1986]. First, the equation of motion for the instantaneous position  $u_z$  of a fluid interface is derived from the linearized hydrodynamic equations. Spontaneous thermal fluctuations, which are the cause of the time-dependent behavior of  $u_z$ , are taken into account by adding stochastic driving forces to the equations of motion. Next, the nonequilibrium ensemble average of the interfacial fluctuations in  $u_z$  is obtained from the generalized fluctuation-dissipation theorem. In this section the spectral asymmetry  $\Delta_c$  is re-derived in detail following the general method used by Grant and Desai. While our final result is equivalent to Grant and Desai's, the derivation given here is more consistent and corrects a number of inaccuracies in the original derivation.

Let us first briefly summarize the framework for calculating equilibrium fluctuations using fluctuating hydrodynamics. The hydrodynamic equation of motion (3.54) describes the average macroscopic behavior of the fluid. If we are interested in instantaneous values of the fluctuating quantities we need to add a Langevin force to Eq. (3.54) [Landau and Lifshitz 1959]

$$\rho \frac{\partial \mathbf{v}}{\partial t} + \nabla p - \eta \nabla^2 \mathbf{v} = \rho \mathbf{g} + \nabla \cdot \mathbf{S}, \quad (4.9)$$

where  $\mathbf{S}$  is a random local stress due to the thermal fluctuations. The fluctuations in the hydrodynamic quantities can now be obtained by formally solving the hydrodynamic equations of motion in terms of  $\mathbf{S}$  and using the fluctuation-dissipation theorem for the random stress  $\mathbf{S}$  [Landau and Lifshitz 1959; Lifshitz and Pitaevskii 1980; Desai and Grant 1986]<sup>†</sup>

$$\langle S_{ik}(\mathbf{r}, t) S_{lm}^*(\mathbf{r}', t') \rangle_{eq} = 4\eta k_B T [\delta_{il} \delta_{km} + \delta_{im} \delta_{kl}] - \frac{2}{3} \delta_{ik} \delta_{lm} \delta(\mathbf{r} - \mathbf{r}') \delta(t - t'), \quad (4.10)$$

---

<sup>†</sup> We have introduced an extra factor of two because of the complex notation used here.

where  $\langle \rangle_{eq}$  denotes an equilibrium ensemble average. This Langevin formalism, which is well justified in the case of equilibrium fluctuations, can be generalized to the case of nonequilibrium steady states of a bulk system [Ronis and Putterman 1980; Tremblay, Arai *et al.* 1981; Zwan, Bedeaux *et al.* 1981]. We will use this generalized Langevin formalism to calculate the power spectrum of the vertical displacement of a nonequilibrium interface.

With the addition of the random stress, the hydrodynamic equations (3.97) – (3.99) become

$$iqv_{xq} + \frac{\partial v_{zq}}{\partial z} = 0, \quad (4.11)$$

$$\rho \frac{\partial v_{xq}}{\partial t} = \eta \left( \frac{\partial^2}{\partial z^2} - q^2 \right) v_{xq} - iq p_q + iq S_{xxq} + \frac{\partial S_{xzq}}{\partial z}, \quad (4.12)$$

$$\rho \frac{\partial v_{zq}}{\partial t} = \eta \left( \frac{\partial^2}{\partial z^2} - q^2 \right) v_{zq} - \frac{\partial p_q}{\partial z} + iq S_{xzq} + \frac{\partial S_{zzq}}{\partial z}, \quad (4.13)$$

and the boundary conditions (3.58) and (3.59) are modified as

$$p_q \Big|_{z=0} - 2\eta \frac{\partial v_{zq}}{\partial z} \Big|_{z=0} - S_{zzq} \Big|_{z=0} - (\sigma q^2 + \rho g) u_{zq} = 0, \quad (4.14)$$

$$-\eta \left( \frac{\partial v_{xq}}{\partial z} + iq v_{zq} \right) \Big|_{z=0} - S_{xzq} \Big|_{z=0} - \mathcal{E} q^2 u_{xq} = 0. \quad (4.15)$$

where  $q$  is a real and positive wavevector. Using the continuity equation (4.11), Eq. (4.12) can be changed to an equation for  $v_{zq}$ . Then multiplying the resulting equation and Eq. (4.13) by  $e^{qz}$ , and using the following relation

$$\int_{-\infty}^0 dz e^{qz} \frac{\partial B}{\partial z} = B \Big|_{z=0} - q \int_{-\infty}^0 dz e^{qz} B, \quad (4.16)$$

one obtains

$$\begin{aligned}
& \rho \left. \frac{\partial v_{zq}}{\partial t} \right|_{z=0} - \eta \left. \frac{\partial^2 v_{zq}}{\partial z^2} \right|_{z=0} + \eta q^2 v_{zq} \Big|_{z=0} + q \left( p_q \Big|_{z=0} - S_{zzq} \Big|_{z=0} + i S_{xzq} \Big|_{z=0} \right) \\
& = -q^2 \int_{-\infty}^0 dz e^{qz} (S_{zzq} - S_{xxq} - 2iS_{xzq}) .
\end{aligned} \tag{4.17}$$

Substituting the boundary values for the pressure and the random stress from boundary conditions (4.14) and (4.15) into the above equation, one gets

$$\begin{aligned}
& \left. \frac{\partial v_{zq}}{\partial t} \right|_{z=0} + \omega_c^2(q) u_{zq} + \frac{\beta_c(q)}{q} \left. \frac{\partial v_{zq}}{\partial z} \right|_{z=0} + \beta_c(q) v_{zq} \Big|_{z=0} - i\mathcal{E}q^3 u_{xq} \\
& = -\frac{q^2}{\rho} \int_{-\infty}^0 dz e^{qz} (S_{zzq} - S_{xxq} - 2iS_{xzq}) .
\end{aligned} \tag{4.18}$$

where  $\omega_c(q)$  and  $\beta_c(q)$  given by Eqs. (3.91) and (3.92) are the angular frequency and temporal damping coefficient of a capillary wave. Using Eq. (4.11) and boundary condition (3.24),  $v_{zq}$  and its derivatives in the above equation can be expressed by the horizontal and vertical displacements of the interface, yielding the equation of motion for the interface covered with a monolayer of surfactant molecules

$$\begin{aligned}
& \left[ \frac{\partial^2}{\partial t^2} + \beta_c(q) \frac{\partial}{\partial t} + \omega_c^2(q) \right] u_{zq}(t) - i \left[ \beta_c(q) \frac{\partial}{\partial t} + \mathcal{E}q^3 \right] u_{xq}(t) \\
& = -\frac{q^2}{\rho} \int_{-\infty}^0 dz e^{qz} [S_{zzq}(z,t) - S_{xxq}(z,t) - 2iS_{xzq}(z,t)] .
\end{aligned} \tag{4.19}$$

Let us now consider the small-viscosity limit ( $\beta_c \ll \omega$ ). If the above equation is Fourier transformed into the frequency domain in the same way as in Eq. (2.11), one obtains

$$\begin{aligned}
& \mathcal{D}(q, \omega) u_{zq}(\omega) + i\beta_c(q)\omega [iu_{zq}(\omega) - u_{xq}(\omega)] - i\mathcal{E}q^3 u_{xq}(\omega) \\
&= -\frac{q^2}{\rho} \int_{-\infty}^0 dz e^{qz} [S_{zzq}(z, \omega) - S_{xxq}(z, \omega) - 2iS_{xzq}(z, \omega)], \tag{4.20}
\end{aligned}$$

where quantities with arguments of  $\omega$  are the Fourier amplitudes and

$$\mathcal{D}(q, \omega) = -\omega^2 - 2i\beta_c(q)\omega + \omega_c^2(q). \tag{4.21}$$

Using Eq. (4.11), one can eliminate  $v_{xq}(t)$  and  $v_{zq}(t)$  from Eqs. (4.12) and (4.13) to get

$$\left( \frac{\partial^2}{\partial z^2} - q^2 \right) p_q(t) = \frac{\partial^2 S_{zzq}(t)}{\partial z^2} - q^2 S_{xxq}(t) + 2iq \frac{\partial S_{xzq}(t)}{\partial z}. \tag{4.22}$$

Applying Eq. (4.16) to this equation and Fourier transforming the result into the frequency domain, one obtains

$$\begin{aligned}
\frac{\partial p_q(\omega)}{\partial z} \Big|_{z=0} - q p_q(\omega) \Big|_{z=0} &= \frac{\partial S_{zzq}(\omega)}{\partial z} \Big|_{z=0} - q S_{zzq}(\omega) \Big|_{z=0} + 2iq S_{xzq}(\omega) \Big|_{z=0} \\
&+ q^2 \int_{-\infty}^0 dz e^{qz} [S_{zzq}(\omega) - S_{xxq}(\omega) - 2iS_{xzq}(\omega)]. \tag{4.23}
\end{aligned}$$

Let us now show that the second term on the left hand side of Eq. (4.20) is negligible. Eqs. (4.12) and (4.13) can be rewritten as

$$-i\rho\omega v_{xq}(\omega) = -iqp_q(\omega) + iqS_{xxq}(\omega) + \frac{\partial S_{xzq}(\omega)}{\partial z} + O(\eta), \tag{4.24}$$

$$-i\rho\omega v_{zq}(\omega) = -\frac{\partial p_q(\omega)}{\partial z} + iqS_{xzq}(\omega) + \frac{\partial S_{zzq}(\omega)}{\partial z} + O(\eta), \tag{4.25}$$

where  $O(\eta)$  represents a term linear in  $\eta$ . Hence one obtains, using Eq. (4.23),

$$\begin{aligned}
\beta_c \omega [iu_{zq}(\omega) - u_{xq}(\omega)] &= i\beta_c \{iv_{zq}(\omega) - v_{xq}(\omega)\} \Big|_{z=0} = \\
&= \frac{i\beta_c}{\omega\rho} \left\{ -qS_{zzq}(\omega) + qS_{xxq}(\omega) + iqS_{xzq}(\omega) - i\frac{\partial S_{xzq}(\omega)}{\partial z} \right\} \Big|_{z=0} \\
&+ \frac{i\beta_c}{\omega} \left\{ \frac{q^2}{\rho} \int_{-\infty}^0 dz e^{qz} [S_{zzq}(\omega) - S_{xxq}(\omega) - 2iS_{xzq}(\omega)] \right\} + \frac{\beta_c}{\omega} O(\beta_c). \quad (4.26)
\end{aligned}$$

Thus, Eq. (4.20) can be written as

$$\begin{aligned}
\mathcal{D}(q,\omega)u_{zq}(\omega) - i\mathcal{E}q^3u_{xq}(\omega) \\
&= - \left[ 1 + \frac{i\beta_c}{\omega} \right] \frac{q^2}{\rho} \int_{-\infty}^0 dz e^{qz} [S_{zzq}(z,\omega) - S_{xxq}(z,\omega) - 2iS_{xzq}(z,\omega)] \\
&- \frac{i\beta_c}{\omega\rho} \left\{ -qS_{zzq}(\omega) + qS_{xxq}(\omega) + iqS_{xzq}(\omega) - i\frac{\partial S_{xzq}(\omega)}{\partial z} \right\} \Big|_{z=0} + \frac{\beta_c}{\omega} O(\beta_c). \quad (4.27)
\end{aligned}$$

In the small-viscosity limit for a clean interface ( $\mathcal{E} = 0$ ), this reproduces the result derived by Grant and Desai [Grant and Desai 1983; Desai and Grant 1986]

$$\mathcal{D}(q,\omega)u_{zq}(\omega) = - \frac{q^2}{\rho} \int_{-\infty}^0 dz e^{qz} [S_{zzq}(z,\omega) - S_{xxq}(z,\omega) - 2iS_{xzq}(z,\omega)]. \quad (4.28)$$

Next we will calculate the power spectrum of the interfacial fluctuations in the presence a small temperature gradient. A steady state solution for the temperature profile and its Fourier transform are given as

$$T(x) = T_0 [1 + kx], \quad (4.29)$$

$$T_q = 2\pi T_0 [\delta(q) + ik\nabla_q \delta(q)], \quad (4.30)$$

where

$$k = \nabla \ln T. \quad (4.31)$$

To first order in  $q$  [Tremblay, Arai *et al.* 1981], Eqs. (4.29) and (4.30) can be approximated by

$$T(x) = T_0 [1 + \sin(kx)], \quad (4.32)$$

$$T_q = 2\pi T_0 \left\{ \delta(q) + \frac{i}{2} [\delta(q+k) - \delta(q-k)] \right\}. \quad (4.33)$$

Fourier transforming the correlation function of the random stress in Eq. (4.10), one gets

$$\begin{aligned} \lim_{\mathcal{T} \rightarrow \infty} \frac{1}{2\mathcal{T}} S_{ikq}(z, \omega) S_{lmq'}^*(z', \omega) \\ = \frac{4\eta k_B T_{q-q'}}{L} [\delta_{il}\delta_{km} + \delta_{im}\delta_{kl} - \frac{2}{3}\delta_{ik}\delta_{lm}] \delta(z-z'), \end{aligned} \quad (4.34)$$

where  $L$  is the dimension of the system in the  $x$ -axis. Using the relation between  $u_{zq}(\omega)$  and  $S_{ikq}(z, \omega)$  in Eq. (4.28), the above equation yields

$$\lim_{\mathcal{T} \rightarrow \infty} \frac{1}{2\mathcal{T}} u_{zq}(\omega) u_{zq'}^*(\omega) = \frac{32\eta q^2 q'^2}{L\rho^2(q+q')\mathcal{D}(q, \omega)\mathcal{D}^*(q', \omega)} k_B T_{q-q'}. \quad (4.35)$$

Then, the power spectrum of the vertical displacement is given by

$$\begin{aligned} P_{u_{zq}}(\omega) \Big|_{SS} &= \lim_{\mathcal{T} \rightarrow \infty} \frac{1}{2\mathcal{T}} \left| u_{zq}(\omega) \right|^2 = \int_{-\infty}^{\infty} \delta(q-q') \lim_{\mathcal{T} \rightarrow \infty} \frac{1}{2\mathcal{T}} u_{zq}(\omega) u_{zq'}^*(\omega) dq' \\ &= \int_{-\infty-L/2}^{\infty-L/2} \int_{-\infty-L/2}^{\infty-L/2} e^{-i(q-q')x} \frac{32\eta q^2 q'^2}{L\rho^2(q+q')\mathcal{D}(q, \omega)\mathcal{D}^*(q', \omega)} k_B T_{q-q'} dx \frac{dq'}{2\pi} \\ &= \int_{-\infty-L/2}^{\infty-L/2} \int_{-\infty-L/2}^{\infty-L/2} \mathcal{R}(q, q') \left\{ \delta(q-q') + \frac{i}{2} [\delta(q-q'+k) - \delta(q-q'-k)] \right\} \frac{dx}{L} dq' \\ &= \mathcal{R}(q, q) + \frac{i}{2} \left[ \mathcal{R}\left(q - \frac{k}{2}, q + \frac{k}{2}\right) - \mathcal{R}\left(q + \frac{k}{2}, q - \frac{k}{2}\right) \right], \end{aligned} \quad (4.36)$$

where the subscript 'SS' denotes a steady state and  $\mathcal{R}(q, q')$  is short-hand for

$$\mathcal{R}(q, q') = e^{-i(q-q')x} \frac{32k_B T_0 \eta q^2 q'^2}{\rho^2 (q+q') \mathcal{D}(q, \omega) \mathcal{D}^*(q', \omega)} . \quad (4.37)$$

To first order in  $k$ ,

$$\begin{aligned} & \frac{i}{2} \left[ \mathcal{R}\left(q - \frac{k}{2}, q + \frac{k}{2}\right) - \mathcal{R}\left(q + \frac{k}{2}, q - \frac{k}{2}\right) \right] \\ &= -\frac{16k_B T_0 \eta q^3}{\rho^2} \left[ \frac{(8\omega^2 + 4\omega_c^2) \omega \frac{\eta k q}{\rho}}{|\mathcal{D}(q, \omega)|^4} + \frac{kx}{|\mathcal{D}(q, \omega)|^2} \right] . \end{aligned} \quad (4.38)$$

For a small temperature gradient

$$L_\nabla \gg L , \quad (4.39)$$

the second term on the right hand side of Eq. (4.38) becomes negligible since

$$|kx| \leq L_\nabla^{-1} L \ll 1 . \quad (4.40)$$

In this limit the steady state power spectrum,  $P_{u_{z,q}}(\omega)|_{SS}$ , then reduces to

$$\boxed{P_{u_{z,q}}(\omega)|_{SS} = P_{u_{z,q}}(\omega)|_{eq} \left[ 1 - \frac{\frac{4\eta}{\rho} (2\omega^2 + \omega_c^2) \omega q \nabla \ln T}{[\omega^2 - \omega_c^2]^2 + 4\beta_c^2 \omega^2} \right]} , \quad (4.41)$$

where the temperature gradient independent term

$$P_{u_{z,q}}(\omega)|_{eq} = \frac{2k_B T_0 q}{\rho \omega_c^2} \frac{4\beta_c \omega_c^2}{[\omega^2 - \omega_c^2]^2 + 4\beta_c^2 \omega^2} . \quad (4.42)$$

represents the equilibrium power spectrum equivalent to that of Eq. (3.90) since in the small-viscosity limit  $\omega_R$  and  $\beta_R$  reduce to  $\omega_c$  and  $\beta_c$ , respectively. For a given capillary wave frequency  $\omega_c$ , this expression yields an asymmetry

$$\boxed{\Delta_c \equiv \frac{P_{u_{z,q}}(-\omega_c) - P_{u_{z,q}}(+\omega_c)}{P_{u_{z,q}}(-\omega_c) + P_{u_{z,q}}(+\omega_c)} = \frac{3}{4} \frac{\sqrt{\sigma \rho}}{\eta} q^{-3/2} \nabla \ln T .} \quad (4.43)$$

Let us compare this result to the approximate expression obtained in the previous section. In the small-viscosity limit, it can be shown that the mean free path of a capillary wave, defined as the inverse of the spatial damping coefficient, is given by<sup>†</sup>

$$l_c \equiv \frac{1}{\Gamma_c} = \frac{1}{\beta_c} \frac{\partial \omega_c}{\partial q} = \frac{3}{4} \frac{\sqrt{\sigma \rho}}{\eta} q^{-3/2}, \quad (4.44)$$

where  $\Gamma_c$  is the spatial damping coefficient (see §5.1). Substituting this equation and  $L_{\nabla} = [\nabla \ln T]^{-1}$  into Eq. (4.43), one obtains

$$\Delta_c = \frac{l_c}{L_{\nabla}}, \quad (4.45)$$

which is identical to the one in Eq. (4.8) derived by using simple arguments.

Note that the results obtained in this chapter are valid when finite size effects and higher order effect in temperature gradient are negligible. To avoid finite size effects the ratio of the mean free path of the capillary wave to the dimension of the system must be much smaller than one. Nonlinearities in the temperature gradient are negligible when the ratio  $l_c/L_{\nabla}$  are small. Combining the condition of Eq. (4.39), the requirement for the these length scales is

$$L_{\nabla} \gg L \gg l_c. \quad (4.46)$$

### §4.3 Experimental

Experiments were carried out with mercury, octane and water. Mercury has a large ratio  $\sqrt{\sigma \rho} / \eta$ , which would yield a large asymmetry (see Eq. 4.43). Unfortunately the high

---

<sup>†</sup> The definition of the mean free path of the capillary wave is different from that of Grant and Desai [Grant and Desai 1983; Desai and Grant 1986]. Theirs is defined as the ratio of the phase velocity of the capillary wave to the temporal damping coefficient

$$l_c \equiv \frac{1}{\beta_c} \frac{\omega_c}{q},$$

while ours is the ratio of the group velocity to the temporal damping coefficient.

surface tension results in low amplitude capillary waves (see Eq. 3.87) and therefore insufficient signal-to-noise ratio to observe the asymmetry. Measurements on octane yielded spectra with an excellent signal-to-noise ratio in equilibrium. In the presence of a temperature gradient, however, the system became unstable. The experiments described below, therefore, were all carried out on water samples which yield a reasonable signal-to-noise ratio, and remain stable because the temperature dependences of  $\sigma$ ,  $\rho$ , and  $\eta$  are relatively small.

For water around room temperature with a temperature gradient of 20 K/cm along its surface<sup>†</sup>, Eq. (4.43) yields an asymmetry of 4.8–8.9 % in the height of the two capillary wave peaks for a capillary wavevector in the range 60–90 cm<sup>-1</sup>. According to Eq. (3.91), this wavevector corresponds to a capillary wave frequency  $f_c$  of 630–1160 Hz. To resolve such a small frequency shift in an optical spectrum requires a resolving power of 10<sup>13</sup> or better. This requirement can be easily satisfied by the Fourier transform heterodyne technique. It is also necessary to shift the frequency of the local oscillator in order to separate the two side peaks of a capillary wave spectrum.

When a light incident at an angle  $\theta_0$  is scattered from a capillary wave, from Eq. (2.51), the scattering angle is given by

$$\phi = \frac{q}{k_{laser} \cos \theta_0}, \quad (4.47)$$

where  $k_{laser}$  and  $q$  are the wavevectors of the incident light and the capillary wave, respectively. To increase the scattering angle for a given wavevector, it is necessary to increase the angle of incidence as much as the dimension of the setup allows. With an incidence angle of 80° from the normal, the scattering angle for a wavevector in the range 60–90 cm<sup>-1</sup> is about 3–5 mrad, and it is essential to minimize stray forward scattering from

---

<sup>†</sup> The maximum value of  $\nabla \ln T$  is limited by the freezing and vaporizing temperatures of the liquid sample. Another limit on  $\nabla \ln T$  is imposed by the appearance of nonlinear effects and convection due to gradients in the density and surface tension.

optics, divergence of the source laser beam, and angular motion of the water surface. To reduce stray forward scattering, no optical component is placed closer than 35 cm from the probing spot on the water surface. The divergence of the laser beam is reduced by spatially filtering and collimating with lenses. Angular stability of the water surface is achieved by reducing the depth of the water sample and isolating the setup from environmental perturbations. The entire experimental setup is placed on an actively stabilized platform (EVIS electronic vibration isolation system, Newport Corporation), which in turn is located on top of a pneumatically vibration-isolated optical table. The angular motion from residual table vibrations was about  $60 \mu\text{rad}$ . The angle of view, determined by the opening of the pinhole, is about  $100 \mu\text{rad}$ .

A schematic diagram of the surface light scattering apparatus is shown in Fig. 4.2.<sup>†</sup> A collimated, 4-mW multimode He-Ne laser beam is split into two with a beam splitter: 5% of the beam serves as local oscillator, while the remainder illuminates the liquid surface. The main beam, which is polarized perpendicular to the plane of incidence, makes an angle of about  $80^\circ$  with the normal to the surface. The beam width near the surface is 2 mm, yielding a surface spot of about 10 mm. A polarizer in front of the photomultiplier tube is used to reject stray light. To separate the two side peaks the local oscillator is frequency-shifted by 3.5 kHz using two acousto-optic modulators (AOM-40, IntraAction Corp.). To align the spectrometer in Fig. 4.2, a strong surface wave of the desired frequency is induced with a wire glued to a tweeter. For large enough amplitude, the Bragg scattered beam is visible and can easily be aligned with the local oscillator beam. Since the alignment is very sensitive to the motion of the interface, good vibration isolation of the system is necessary.

The water sample is contained in a shallow black Delrin container ( $7.5 \times 7.5 \times 0.4 \text{ cm}^3$ ), located inside a sealed compartment ( $66 \times 23 \times 23 \text{ cm}^3$ ) made of black anodized aluminum. Much attention is paid to prevent dust and impurities from contaminating the

---

<sup>†</sup> The setup was designed before the implementation of the parallel-beam method described in Chapter 2.

water surface. Distilled and deionized water is obtained from a Milli-Q system and prepared in a class 1000 clean room. Before each set of measurements the Delrin container is carefully cleaned and soaked. Then, the compartment is evacuated and flushed several times with ‘dry high purity’ grade nitrogen gas filtered through a  $0.22\text{-}\mu\text{m}$  filter to remove dust particles. Finally, the distilled and deionized water is introduced into the compartment and in the container by means of a feedthrough tube containing a  $0.22\text{-}\mu\text{m}$  filter, and the compartment is filled with nitrogen gas at atmospheric pressure.

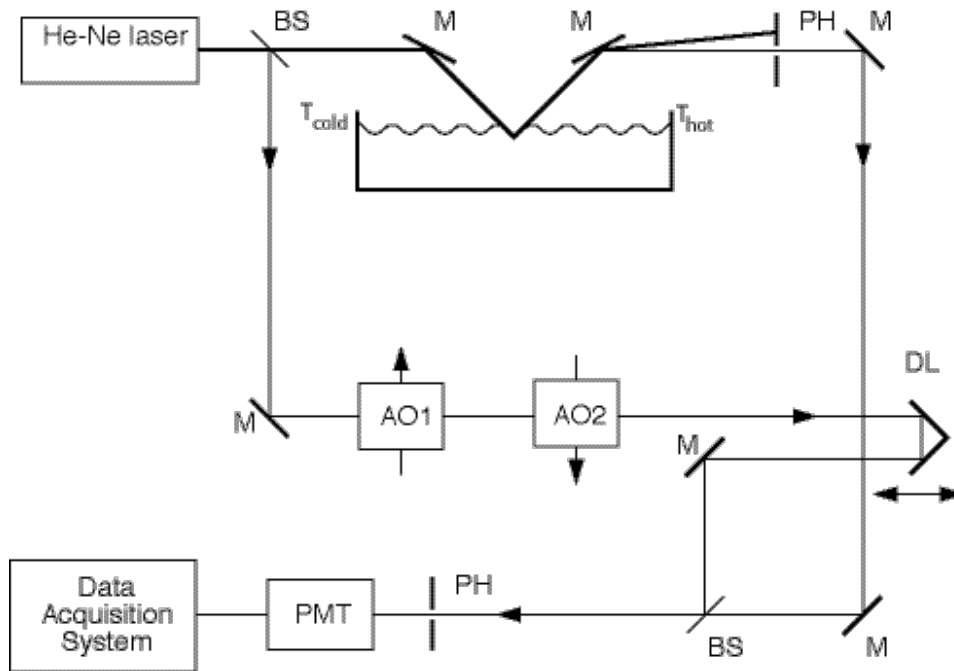


Fig. 4.2. Schematic diagram of the experimental setup. The surface of the liquid is probed with a multimode He-Ne laser beam. A local oscillator is derived from the same laser, and frequency-shifted by a set of two acousto-optic modulators (AO1 and AO2). The beat signal of the scattered light with the local oscillator is recorded with a photomultiplier tube (PMT). M = mirror, BS = beam splitter, PH = pinhole, DL = delay line.

The temperature gradient along the surface is applied with a pair of epoxy-coated copper plates that are temperature-controlled with two thermoelectric heat pumps (CP 1.4-127-06L, Melcore) as shown in Fig. 4.3. The plates, which are spaced by 1.6 cm, are immersed just below the surface to avoid distortion of the surface. Because of evaporation and freezing of the water, the maximum workable temperature difference of the two plates is about 30 K. A liquid-cooled heat sink drains the excess heat from the heat pumps and

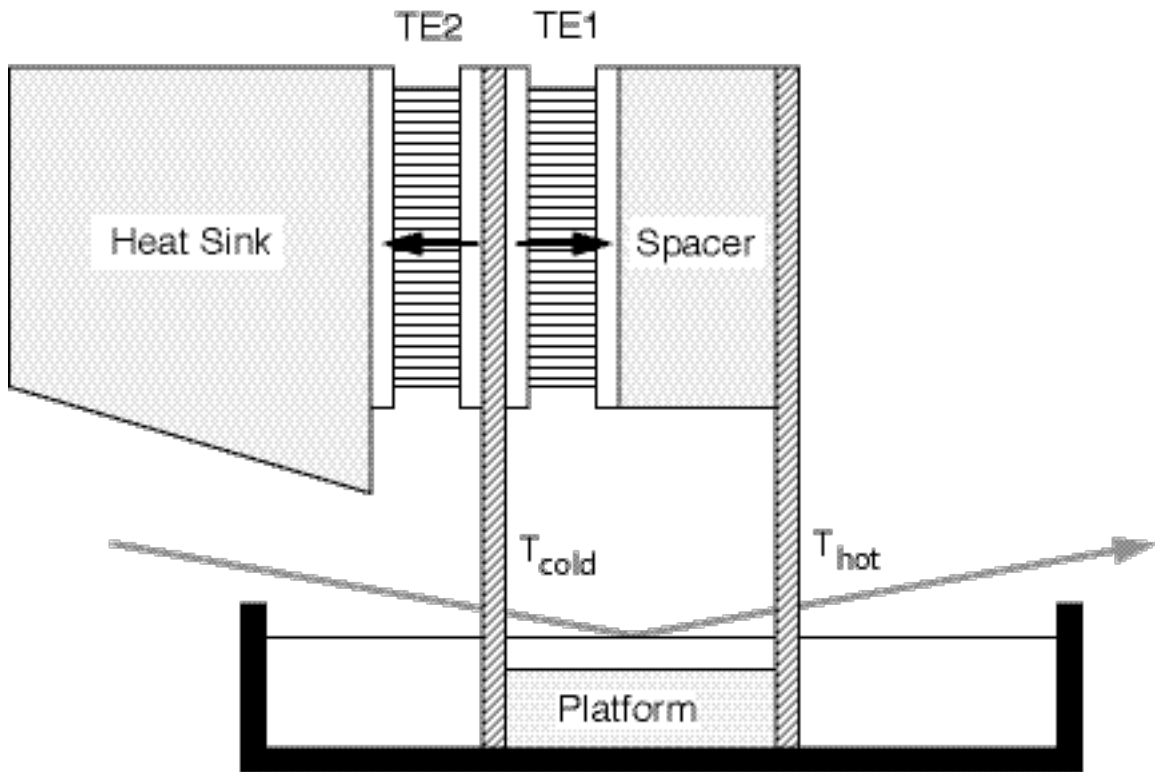


Fig. 4.3. Temperature gradient assembly. A temperature gradient is applied along the surface by a pair of copper plates kept at temperatures  $T_{hot}$  and  $T_{cold}$ , respectively. The spacing between the plates is 16 mm. The temperatures of the plates are controlled with a pair of thermoelectric heat pumps (TE1 and TE2). Arrows indicate the direction of the heat flows. A water cooled heat sink removes the excess heat from the heat pumps.

prevents condensation of water vapor on the optics. The temperature of the plates is monitored by a pair of thermistors that read the temperatures to within  $\pm 0.1$  K. The actual temperature profile along the surface was measured with a second pair of thermistors mounted on a translation stage. Because of convection in the liquid, the profile is not linear, and the temperature gradient at the center between the two plates is about two times smaller than what one would expect for a linear profile. A platform is inserted between the two copper plates to reduce the convection.

The beat signal between the scattered light and the local oscillator is recorded with a photomultiplier tube. The signal is sampled for 15 s at a 20-kHz rate with a GW Instruments MacAdios II computer interface, and the full signal trace is stored in the memory of an Apple Macintosh II computer. Next, the frequency spectrum of the digitized signal is obtained by a fast Hartley transform of the stored signal [Bracewell 1986]. The resulting spectrum, an example of which is shown in Fig. 4.4, corresponds to the spectrum of the interfacial fluctuations as described in the previous chapter. To improve the signal-to-noise ratio, this procedure was repeated up to eight times.

Asymmetry values are determined by fitting a theoretical spectrum to the experimental data points. Because of the divergence of the laser beam, finite size of the pinholes, and residual motion of the water surface, the experimental spectra are always convoluted with some instrumental function. For example, the spectrum in Fig. 4.4 has a FWHM of 300 Hz which is about five times larger than the width of  $2\beta_c/2\pi$ . The best way to fit the data points therefore would be to use a convolution of the theoretical spectrum Eq. (4.41) with the instrumental function measured for a system with very small viscosity. In general, however, the instrumental function is approximately Gaussian [Earnshaw, McGivern *et al.* 1988], and the measured spectrum can be approximated by a convolution of a Lorentzian and a Gaussian (Voigt profile) [Armstrong 1967]. Since we are interested in the relative difference of the intensities of the two side peaks, the shifted power spectrum of the detector signal is approximated by ‘squared’ Lorentzians as

$$P_j(\omega) \approx P_o(\omega) + \frac{4\beta_c^2 \omega_c^2 \left[ 1 - \Delta_c \frac{\omega - \omega_{AO}}{\omega_c} \right] I_c}{[(\omega - \omega_{AO})^2 - \omega_c^2]^2 + 4\beta_c^2 (\omega - \omega_{AO})^2}, \quad (4.48)$$

or by Lorentzians with the narrow line approximation (see Eq. 3.93) as

$$P_j(\omega) \approx P_o(\omega) + \frac{\beta_c^2 (1 - \Delta_c) I_c}{(\omega - \omega_{AO} - \omega_c)^2 + \beta_c^2} + \frac{\beta_c^2 (1 + \Delta_c) I_c}{(\omega - \omega_{AO} + \omega_c)^2 + \beta_c^2}, \quad (4.49)$$

where

$$P_o(\omega) = \frac{\beta_o^2 I_o}{(\omega - \omega_{AO})^2 + \beta_o^2} + B, \quad (4.50)$$

is the central Lorentzian peak at  $\omega = \omega_{AO}$  with FWHM of  $2\beta_o$  which is mainly due to the stray scattering and the background noise  $B$ . The measured spectra were fit to simple Lorentzians, squared Lorentzians, and Voigt profiles. All asymmetries reported here were obtained from the nonlinear least-squares fitting with Voigt profiles because these fits produced about two times better  $\chi^2$ -values than others.

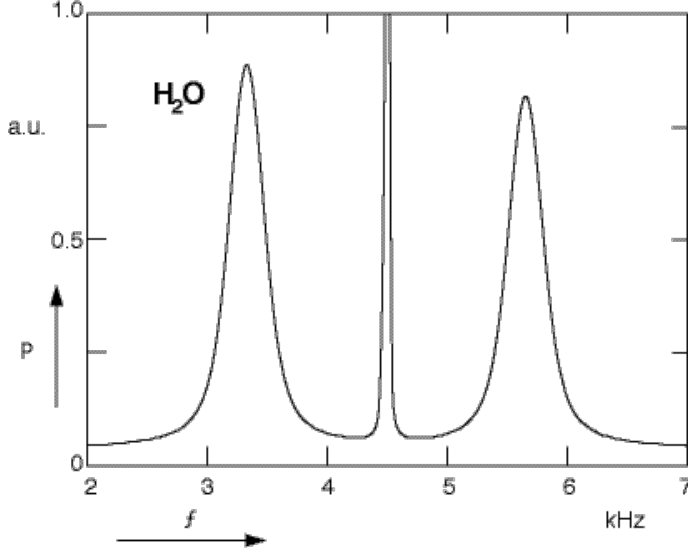


Fig. 4.4 Experimental spectrum for  $q = 90 \text{ cm}^{-1}$  and  $\nabla T = 9.5 \text{ K/cm}$  at  $T = 295 \text{ K}$  showing the two capillary wave peaks around an intense central peak, which is due to stray elastic scattering of the incident laser light. The solid line is a least-squares fitted set of two Voigt profiles for the two side peaks and a Lorentzian for the central peak to the data points. The corrected experimental asymmetry,  $\Delta_c^{expt}$ , is 0.008 while the theoretically predicted asymmetry in Eq. (4.43),  $\Delta_c^{theor}$ , is 0.023.

#### §4.4 Results and discussion

In Fig. 4.5, the experimental asymmetry,  $\Delta_c^{expt}$ , determined from the fit as described in the previous section, is compared with the theoretical one,  $\Delta_c^{theor}$ , predicted by Eq. (4.43), using literature values for the density, surface tension and viscosity at the average temperature of the probing region. Since the frequency response of the apparatus is not completely flat, the spectra taken in the absence of a temperature gradient show a small instrumental asymmetry,  $\Delta_c^{inst}$ . All data were corrected for this instrumental asymmetry. The error bar for the point at  $\Delta_c^{theor} = 0$ , represents the standard deviation in  $\Delta_c^{inst}$  when  $\nabla T = 0$ . Because the sign of the temperature difference in our setup cannot be reversed, the sign of  $\hat{\mathbf{q}} \cdot \nabla T$  was changed by reversing  $\hat{\mathbf{q}}$  and not  $\nabla T$ . As shown in Fig. 4.5, this indeed resulted in a sign change of the measured asymmetry. The slope of the experimental data points, represented by the solid line in Fig. 4.5, is 0.35, or about three times smaller than expected on the basis of Eq. (4.43). In light scattering experiments on nonequilibrium bulk

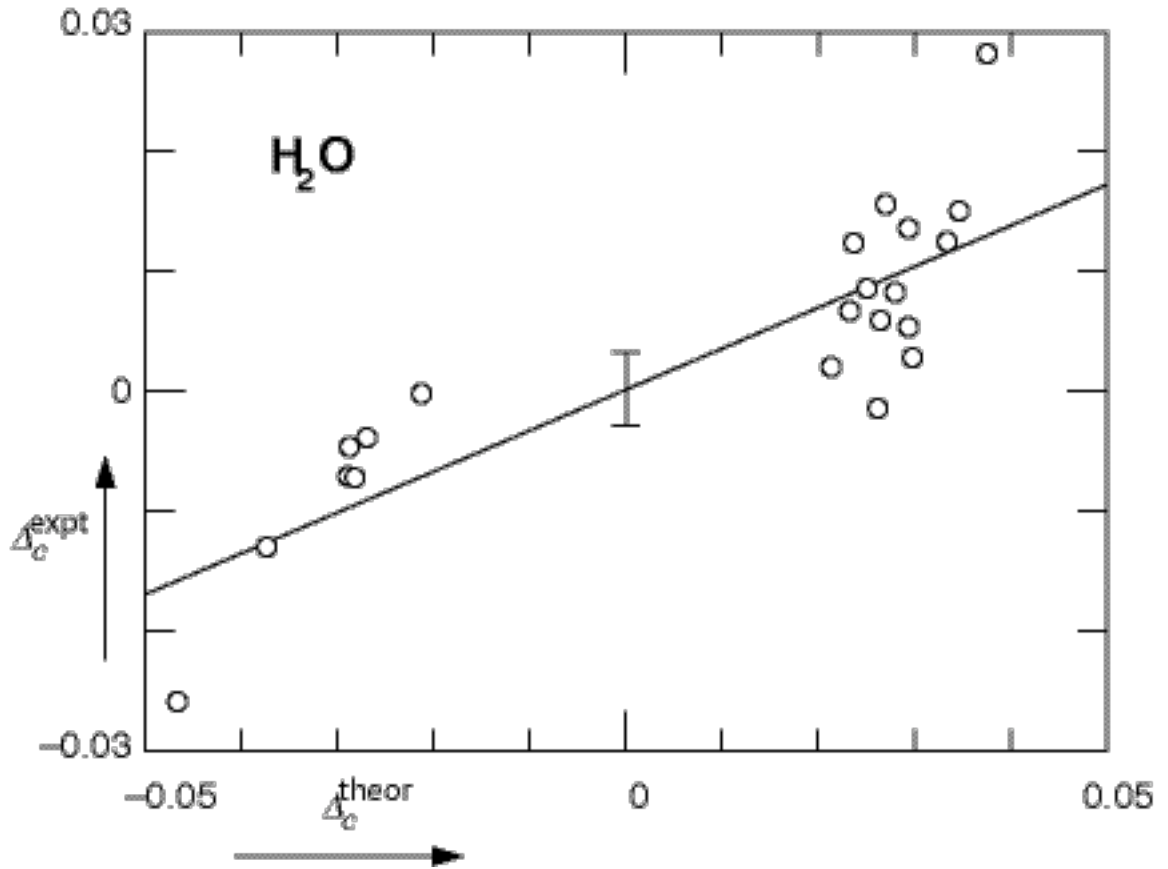


Fig. 4.5 Measured capillary wave asymmetry  $\Delta_c^{expt}$  vs. theoretical asymmetry  $\Delta_c^{theor}$  given in Eq. (4.43). The expected slope is 1. The experimental slope (solid line) is 0.35.

liquids, similar discrepancies have been observed [Beysens, Garrabos *et al.* 1980] and explained in terms of finite size [Satten and Ronis 1982] and nonlinearity [Kieft, Clouter *et al.* 1984] effects. In a more recent experiment by Kieft *et al.*, agreement with the theory was obtained for a particular ‘best’ data set, and it was shown that while nonlinearities cannot be excluded, finite size effects indeed affect the measurements. Theoretical analyses of finite size and nonlinearity effects [Kirkpatrick, Cohen *et al.* 1982] have so far only been carried out for bulk liquids.

In the case of a nonequilibrium interface one expects finite size effects to play a role when  $l_c/L$ , the ratio of the mean free path,  $l_c$  to the spacing  $L$  between the two plates is large, or when the acoustic reflectivity  $R$  of the container walls is large [Satten and Ronis 1982]. Nonlinear effects of the temperature gradient depend on the ratio of the mean free path to the characteristic length scale of the gradient,  $l_c/L_\nabla$ . In addition, the ratio  $\Delta T/T$  must be

small enough to neglect the temperature dependence of the molecular parameters and to maintain a steady state. In the present setup,  $0.45 \leq l_c/L \leq 0.9$ ,  $l_c/L_{\nabla} \leq 0.05$ ,  $\Delta T/T \approx 0.1$ ; this is comparable to the situation for the best data set from the experiment by Kiefte *et al.* on bulk water, which is in agreement with theory. In Tab. 4.1, our results are compared with those of the bulk experiments.<sup>†</sup> The spectrum for an induced capillary wave travelling in one direction has only one side peak, showing that the acoustic reflectivity is negligible in our setup. We attempted to investigate the dependence of the asymmetry on the temperature difference and the plate spacings. Unfortunately because of the limited signal-to-noise ratio the relevant parameters could not be changed sufficiently to further investigate these effects.

Based on more recent evidence, we believe that contamination of the water surface with impurities from the gas phase can account for the observed discrepancy. Contamination at the interface increases the spatial damping coefficient which in turn reduces the mean free path of the capillary wave of Eq. (4.44) and the asymmetry Eq. (4.45). In a related experiment (see §5.3.1) we found that the spatial damping coefficient of capillary wave on a water surface can vary by factor of two to four from the expected literature value unless ‘ultrapure’ grade (THC < 0.5 ppm) nitrogen gas is used to fill the compartment, and the water surface is meticulously cleaned by multiple wiping and aspirating of the surface using a Langmuir trough.

---

<sup>†</sup> Note that the definition of our mean free path is one and half times larger than that used by many other authors.

Table 4.1 Comparison with bulk experiments.

	Beysens <i>et al.</i> <sup>1</sup>	Kiefte <i>et al.</i> <sup>2</sup>	Ours
$\frac{l_c}{L}$	4.5 – 9	0.23 – 4.5	0.45 – 0.9
$\frac{l_c}{L\nabla}$	0.75 – 1.5	0.03 – 0.6	$\leq 0.05$
$\frac{\Delta T}{T}$	$\approx 0.16$	$\approx 0.15$	$\approx 0.1$
$\frac{\Delta_c^{expt}}{\Delta_c^{theor}}$	$\approx 0.3$	$\approx 1$	$\approx 0.35$

1 [Beysens, Garrabos *et al.* 1980]

2 [Kiefte, Clouter *et al.* 1984]

In conclusion, the Fourier transform heterodyne spectroscopy technique, with its directional sensitivity and high resolution, allows one to observe the broken translational symmetry on a nonequilibrium liquid interface. We have measured the asymmetry of the two capillary wave peaks of light scattered from a liquid-vapor interface subject to a temperature gradient. Our result agrees, in sign and order of magnitude, with the asymmetry predicted by linearized fluctuating hydrodynamics.

Table 4.1 Comparison with bulk experiments.

	Beysens <i>et al.</i> <sup>1</sup>	Kiefte <i>et al.</i> <sup>2</sup>	Ours
$\frac{l_c}{L}$	4.5 – 9	0.23 – 4.5	0.45 – 0.9
$\frac{l_c}{L\nabla}$	0.75 – 1.5	0.03 – 0.6	$\leq 0.05$
$\frac{\Delta T}{T}$	$\approx 0.16$	$\approx 0.15$	$\approx 0.1$
$\frac{\Delta_c^{expt}}{\Delta_c^{theor}}$	$\approx 0.3$	$\approx 1$	$\approx 0.35$

1 [Beysens, Garrabos *et al.* 1980]

2 [Kiefte, Clouter *et al.* 1984]

In conclusion, the Fourier transform heterodyne spectroscopy technique, with its directional sensitivity and high resolution, allows one to observe the broken translational symmetry on a nonequilibrium liquid interface. We have measured the asymmetry of the two capillary wave peaks of light scattered from a liquid-vapor interface subject to a temperature gradient. Our result agrees, in sign and order of magnitude, with the asymmetry predicted by linearized fluctuating hydrodynamics.

## Chapter V

### Damping of Capillary Waves

In the 18th century, Benjamin Franklin wrote in a letter to a colleague [Franklin 1774]:

*... I then went to the windward side, where (the waves) began to form; and there the oil, though not more than a teaspoonful, produced an instant calm over a space several yards square, which spread amazingly, and extended itself gradually till it reached the lee side, making all that quarter of the pond, perhaps half an acre, as smooth as a looking glass.*

...

This fascinating calming effect of oils has actually been known to sailors since antiquity and was used by the Greek to calm rough seas. It is, however, only after Franklin's experiment that the calming effect of oils has drawn the attention of scientists and engineers.

More than a century later, Rayleigh realized that Franklin's oil film was only a single molecule thick [Rayleigh 1890]. Although this calming effect of a monolayer is not yet fully understood, it has been established that the viscoelastic properties of the monolayer contribute to the calming effect in two ways. First, theoretical studies have shown that the presence of a monolayer with finite dilational compressibility can suppress the generation of capillary waves by reducing the coupling between the liquid surface and the wind [Miles 1967; Nelson 1985]. The second way in which the viscoelastic properties of the monolayer contribute to the calming effect is by increasing the damping of any capillary waves present

at the liquid interface. It is this damping mechanism that we will be dealing with in this chapter. First we will discuss the relation between the damping coefficient of a capillary wave and the viscoelastic properties of a monolayer-covered interface. Next we will present the results of experiments on the spatial damping of capillary waves using a newly developed technique.

### §5.1 Damping measurements of capillary waves

The hydrodynamic theory of capillary waves on an interface provides a relation between the viscoelastic properties of the interface and the characteristics of the waves in the form of a dispersion relation between the wavevector,  $Q$ , and angular frequency,  $\Omega$ , of capillary waves (see Eq. 3.70)

$$D(Q, \Omega; \rho, \eta, \sigma, \mathcal{E}) = 0. \quad (5.1)$$

This equation allows one to obtain information on viscoelastic moduli  $\sigma$  and  $\mathcal{E}$  for a fluid of known density  $\rho$  and bulk shear viscosity  $\eta$  by measuring the relation between the wavevector and angular frequency of capillary waves.

In general the wavevector and angular frequency are complex numbers with their imaginary parts representing the damping of capillary waves. Measurements of this damping can be classified into two categories: 1) *temporal* damping measurements of thermally excited waves; the wavevector is set to a real value, and the real and imaginary parts of the angular frequency  $\Omega$  are measured [Chen, Kawaguchi *et al.* 1987; Earnshaw, McGivern *et al.* 1988; Thominet, Stenvot *et al.* 1988; Earnshaw, McGivern *et al.* 1990], and 2) *spatial* damping measurements of induced waves; now the angular frequency is fixed to some real value, and the real and imaginary parts of the wavevector  $Q$  are measured [Goodrich 1962; Mann and Hansen 1963; Davies and Vose 1965; Stenvot and Langevin 1988].

One can derive a general relationship between the damping coefficients obtained

from these two types of damping measurements. If one expands the dispersion equation (5.1) to first order for each of the cases mentioned above, one gets

$$D(q, \omega - i\beta) = D(q, \omega) - i \left( \frac{\partial D}{\partial \omega} \right)_q \beta = 0, \quad (5.2)$$

$$D(q + i\Gamma, \omega) = D(q, \omega) + i \left( \frac{\partial D}{\partial q} \right)_\omega \Gamma = 0. \quad (5.3)$$

Equating Eqs. (5.2) and (5.3) yields the following relation between the temporal and spatial damping coefficients

$$\beta = - \frac{\left( \frac{\partial D}{\partial q} \right)_\omega}{\left( \frac{\partial D}{\partial \omega} \right)_q} \Gamma = \frac{\partial \omega}{\partial q} \Gamma = v_g \Gamma, \quad (5.4)$$

where  $v_g$  is the group velocity of the wave. It is important to note that this relation only holds when the damping coefficients are sufficiently small to neglect higher order terms. Therefore, this relation cannot be used in the case of strongly damped waves.

The temporal damping of capillary waves produced by thermal fluctuations has been studied extensively using light scattering techniques [Thominet, Stenvot *et al.* 1988; Earnshaw, McGivern *et al.* 1988]. In these experiments, the viscoelastic moduli  $\sigma$  and  $\mathcal{E}$  are obtained from the power spectrum of the scattered light. Although this method has the advantage of not perturbing the interface and obtaining two viscoelastic moduli from a single measurement, it has a low accuracy because the measured spectrum is in general significantly broadened by instrumental contributions.

Alternatively, one can study the spatial damping of an induced capillary wave from the deflection of a laser beam specularly reflected by the wave [Sohl and Miyano 1979; Stenvot and Langevin 1988]. The deflection angle, which is proportional to the amplitude of the wave, is measured as a function of the distance between the point where the wave is induced and the point where the laser beam probes the interface to determine the spatial

damping coefficient. The highest frequency ( $\approx 1000$  Hz) one can study with this technique, however, is limited by the spot size of the laser light beam on the interface.

If, instead, a heterodyne technique is used to measure the amplitude of the wave, one can probe a wider frequency range. In the next section, we will discuss the application of heterodyne light scattering to the measurement of the spatial damping of induced capillary waves.

## §5.2 Spatial damping of induced waves

### §5.2.1 Basic considerations

Let us first discuss in more detail how viscoelastic moduli of an interface can be determined from the spatial damping coefficient. In a spatial damping measurement, a sinusoidal plane wave of a real angular frequency  $\omega_{ind}$  is induced by an external force. The resulting waves propagating in opposite directions are of the form

$$u_z = u_{z0} e^{iq_{ind}|x| - i\omega_{ind}t} = A(x) e^{iq_{ind}|x| - i\omega_{ind}t}, \quad (5.5)$$

where

$$A(x) = u_{z0} e^{-\Gamma|x|}, \quad (5.6)$$

is the amplitude of the wave at a distance  $x$  from the point where the wave of amplitude  $u_{z0}$  is induced. The spatial damping coefficient  $\Gamma$  is obtained from the decay of the wave amplitude as a function of distance  $x$ . The real part  $q_{ind}$  is related to the wavelength of the wave  $\lambda$  by

$$q_{ind} = \frac{2\pi}{\lambda}. \quad (5.7)$$

The wavelength  $\lambda$  can be measured directly by a microscope using a stroboscopic method

[Goodrich 1961], or indirectly from the scattering angle using the momentum conservation condition of Eq. (2.51).

The complex wavevector and angular frequency are related by the dispersion equation

$$D(q_{ind} + i\Gamma, \omega_{ind}) = 0 . \quad (5.8)$$

Without additional information it is not possible to determine two viscoelastic moduli  $\sigma$  and  $\mathcal{E}$  from this single equation. Let us therefore consider a number of special cases.

1) *Separate measurement of interfacial tension.* As discussed in §3.1, viscoelastic moduli are complex numbers and in general the imaginary and real parts are functions of frequency. In practice, however, it is very difficult to determine the dynamic behavior of all viscoelastic moduli for an interface, and approximations are made to simplify the situation. There are indications that the transverse surface viscosity  $\mu$  is much smaller than other viscoelastic moduli [Langevin and Greismar 1980; Earnshaw, McGivern *et al.* 1988], and the interfacial tension is usually considered to be real:

$$\sigma(\omega) = \sigma_0(\omega) - i\omega\mu(\omega) \approx \sigma_0(\omega). \quad (5.9)$$

If the frequency dependence of interfacial tension is negligible,<sup>†</sup> the static interfacial tension measured by mechanical methods such as by a Wilhelmy plate can be used to solve the dispersion equation with a single measurement of the complex wavevector to determine the dilational modulus  $\mathcal{E}$  [Stenvot and Langevin 1988].

2) *Pure interfaces.* For a pure liquid surface the dilational modulus  $\mathcal{E}$  and the transverse surface viscosity  $\mu$  are zero, so

$$\mathcal{E} = 0 , \quad \sigma = \sigma_0 . \quad (5.10)$$

---

<sup>†</sup> Dynamic interfacial tension values obtained from temporal damping measurements differ from the static ones  $\sigma_0(0)$  by less than 1 dyne/cm [Earnshaw, McGivern *et al.* 1988].

This yields a system of two equations (the real and imaginary parts of the dispersion equation) and one real unknown,  $\sigma_0$ .

When the damping is small ( $\Gamma \ll q_{ind}$ ), the dispersion equation reduces to an approximate expression for the complex wavevector [Goodrich 1961]

$$Q_{ind} \approx \sqrt[3]{\frac{\rho \omega_{ind}^2}{\sigma_0}} - i \frac{4\eta}{3\sigma_0} \omega_{ind}, \quad (5.11)$$

which yields the spatial damping coefficient

$$\Gamma = \Gamma_c \equiv \frac{4\eta}{3\sigma_0} \omega_{ind}, \quad (5.12)$$

where  $\Gamma_c$  is the spatial damping coefficient of capillary waves at a clean liquid interface. Thus, the interfacial tension  $\sigma_0$  can be obtained directly from the measured spatial damping coefficient  $\Gamma$ . A separate measurement of the real part of the wavevector provides an independent check on the value of  $\sigma_0$ .

3) *Monolayer-covered liquid interfaces.* An approximate expression for the dispersion equation for an interface covered with an insoluble monolayer with a negligible transverse surface viscosity  $\mu$  was first derived by Dorrestein [Dorrestein 1951]. In the small-viscosity limit

$$\theta \equiv \frac{\beta_c}{\omega_c} = 2\eta \sqrt{\frac{q_{ind}}{\sigma_0 \rho}} \ll 1, \quad (5.13)$$

where  $\omega_c$  and  $\beta_c$  are the frequency and temporal damping coefficient of a capillary wave on a clean interface given in Eqs. (3.91) and (3.92), respectively, the angular frequency is given by

$$\Omega \approx \omega_c \left[ \frac{\frac{1}{2}\xi - i\theta}{1 - (1-i)\xi\theta^{-1/2}} + 1 \right], \quad (5.14)$$

with

$$\xi \equiv \frac{\mathcal{E}}{\sigma_0} = \frac{\mathcal{E}_0}{\sigma_0} - i\omega \frac{\kappa}{\sigma_0} . \quad (5.15)$$

If one substitutes the static interfacial tension for  $\sigma_0$ , the dispersion equation (5.14) allows one to determine the dilational modulus  $\mathcal{E}$  [Stenvot and Langevin 1988].

For a pure liquid surface Eqs. (5.11) and (5.12) have been verified experimentally [Goodrich 1962; Stone and Rice 1977; Earnshaw and McGivern 1987]. For monolayer-covered surfaces, however, the agreement between theory and experiment is qualitative at best. A possible reason for this is that the transverse and dilational surface viscosities may not be zero. There are many indications, including our own results, that the dilational surface viscosity  $\mu$  plays an important role for surfactant monolayers [Langevin and Greismar 1980; Earnshaw, McGivern *et al.* 1988].

### §5.2.2 Power spectrum of an induced wave

Let us next consider the measurement of the capillary wave amplitude using light scattering. First we need to calculate the Fourier amplitude of the capillary wave in Eq. (5.5) in order to obtain the power spectrum. For a wavevector in the  $x$ -direction, the Fourier amplitude is given by

$$u_{zq}|_{x_i} = \int_0^{l_y} \int_{x_i}^{x_i+l_x} u_z(x,y) e^{-iqx} dx dy = \frac{u_{z0} e^{\mathcal{G}x_i} [e^{\mathcal{G}l_x} - 1]}{\mathcal{G}l_y} e^{-i\omega_{ind}t} \quad \text{for } x_i > 0, \quad (5.16)$$

where the Fourier integration is restricted to the dimensions  $l_x$  and  $l_y$  of the laser spot at the interface and  $x_i$  is the distance between the probing beam and the point where the wave is induced, and

$$\mathcal{G} = -\Gamma + i(q_{ind} - q). \quad (5.17)$$

A similar result can be derived for negative  $x_i$ . Using Eq. (3.76), one gets for the power

spectrum of the induced capillary wave

$$P_{u_{z_0}}(\omega) \Big|_{x_i} \propto |u_{z_0}|^2 e^{-2\Gamma|x_i|} \frac{\delta(\omega - \omega_{ind})}{(q - q_{ind})^2 + \Gamma^2} . \quad (5.18)$$

As we have seen the light scattering spectrum is directly related to the power spectrum of the capillary waves (see Eqs. 2.39 and 2.41).

Because of the delta-function in Eq. (5.18) the heterodyne spectrum of the scattered light will thus have a sharp peak at angular frequency  $\omega_{ind}$ . At this frequency the intensity  $P(\omega_{ind})$  of the scattered light is proportional to the square of the amplitude of the induced wave  $u_{z_0}$  and it falls off exponentially as a function of distance  $x_i$ . Measuring  $P(\omega_{ind})$  as a function of  $x_i$  therefore directly determines the spatial damping coefficient  $\Gamma$ .

Alternatively one can measure  $P(\omega_{ind})$  as a function of  $q$  (in practice this means measuring the scattering intensity as a function of scattering angle). According to Eq. (5.18) the intensity of the scattered light then has a Lorentzian profile centered at  $q_{ind}$  with a full-width at half-maximum of  $2\Gamma$ . The damping coefficient  $\Gamma$  can therefore also be determined by measuring the spatial profile of the scattered light. This technique is discussed in more detail in §5.2.4.

### §5.2.3 Double-beam heterodyne measurements of spatial damping

As shown in the previous section the spatial damping coefficient can be obtained by measuring the amplitude of the induced peak in the frequency spectrum of the scattered light as a function of distance. Note that one only needs to compare relative changes in peak intensities, and that a deconvolution of instrumental broadening is not necessary. There are, however, a number of technical difficulties: 1) measurement of the intensity of a very narrow peak, 2) inducing a capillary wave of a given frequency without perturbing the interface or monolayer, and 3) varying the distance without affecting the measurement.

*Intensity measurement.* In theory the width of the induced peak is infinitely narrow, see Eq. (5.18). In practice, however, it has a small, but finite, instrumental width due to fluctuations in  $\omega_{ind}$ . In general the width of the induced peak is much narrower than the spacing  $\delta f_{samp}$  between the discrete points in the heterodyne frequency spectrum (see Eq. 2.44). As a result the center frequency of the peak usually falls in between two spectral points and it is hard to obtain the peak intensity from the values of the discrete spectrum.<sup>†</sup> If the average frequency does not drift, however, one can simply compare the values of the highest point in the peaks, since for a given spectral shape these values are directly proportional to the intensity of the real peaks.

*Inducing capillary waves.* For accurate measurements of the spatial damping of a monolayer-covered interface it is preferable that the wave-inducing mechanism does not touch the interface. A suitable technique is that of electrocapillarity [Sohl, Miyano *et al.* 1978]; capillary waves are generated by applying an oscillating electric potential to a sharp blade edge placed close to the interface. The potential difference between the blade and the interface creates an inhomogeneous electric field that exerts a force on the molecules because of their dipole moments. Although a detailed calculation of this effect is complicated a few basic remarks are in order.

The electric field around the blade edge is a steep function of the distance  $h$  from the edge and is proportional to the applied electric potential  $V$  [Jackson 1975]

$$E \propto Vh^{-1/\nu}, \quad (5.19)$$

---

<sup>†</sup> Since the peaks consist of at most four points a simple fitting procedure does not work well. Instead, using the relation

$$\int_{-\infty}^{\infty} \sin \omega_m t \sin \omega_n t dt = 2\pi \delta(\omega_m - \omega_n) \quad \text{for } \omega_m, \omega_n > 0,$$

one can get an accurate intensity by maximizing the product of the digitized detector signal and a sine wave with angular frequency  $\omega_{ind}$  as a function of the phase of the sine wave.

where  $\nu$  is an exponent in the range 2–3 depending on the edge angle of the blade. This electric field induces an electric dipole proportional to  $E$  on the interface, and the change in the electric energy due to the induced dipole is proportional to the *square* of the electric field applied to the blade. The force on this induced dipole is then given by the derivative of the dipole energy, and the amplitude of the induced wave is given by

$$u_z(0) \propto V^2 h^{-2/\nu-1}. \quad (5.20)$$

By applying an electric potential of angular frequency  $\frac{1}{2} \omega_{ind}$ , a wave of angular frequency  $\omega_{ind}$  is induced. To increase the efficiency of capillary wave generation, it is often necessary to put the blade edge close (typically less than 0.25 mm) to the interface.

*Varying distance.* To vary the distance, one must either move the point where the capillary wave is induced or that where the surface is probed. Since the heterodyne signal is very sensitive to the alignment of the scattered and the local oscillator beams, moving the probe spot is not practical. On the other hand, with the electrocapillarity method mentioned above, keeping the amplitude of the induced waves constant while moving the blade is also difficult; since the wave amplitude is a steep function of the distance between the blade edge and the liquid surface, see Eq. (5.20), raising or lowering the blade by a minute amount in the translation process can alter the amplitude of the wave dramatically. If the amplitude of the source wave  $u_{z0}$  is not constant as a function of distance, one does not obtain an exponential fall-off as shown in Eq. (5.18).

This problem can be circumvented by carrying out a *differential* measurement and probing two instead of one points at the interface, see Fig. 5.1. The surface is probed at two fixed positions  $x_1$  and  $x_2$ , separated by a distance  $d$ , while the blade is placed at a variable position  $x$  between  $x_1$  and  $x_2$ . The peak intensities in the light scattering spectrum at  $x_1$  and  $x_2$  are

$$P_1(\omega_{ind}) = B_1 |u_{z0}|^2 e^{-2\Gamma|x-x_1|} = B_1 |u_{z0}|^2 e^{-2\Gamma(x-x_1)}, \quad (5.21)$$

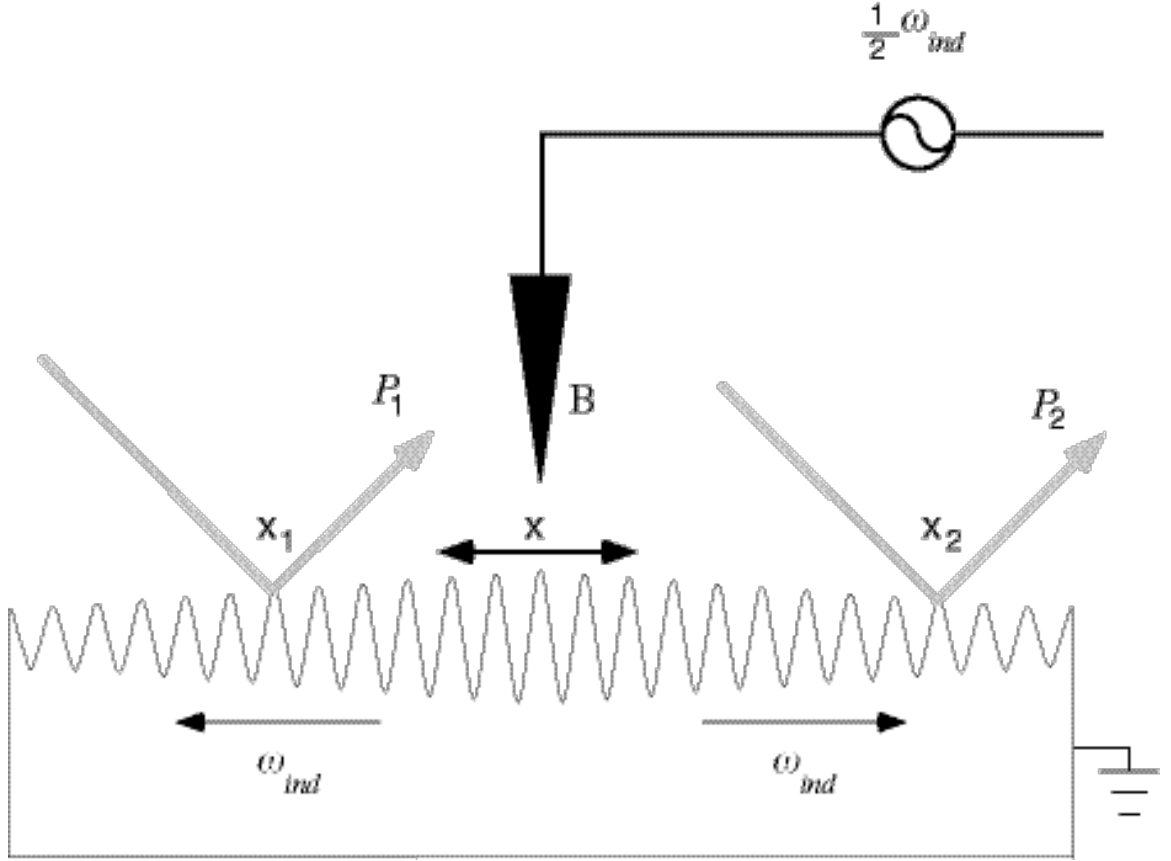


Fig. 5.1. Double-beam measurement of the spatial damping of induced capillary waves. By applying an oscillating electric potential of angular frequency  $\omega_{ind}/2$  to the blade (B) at position  $x$ , capillary waves of angular frequency  $\omega_{ind}$  propagating away from the blade are induced. The amplitude of the wave at the position of the blade is  $u_{z0}$  and it decays exponentially in space. Amplitudes of the waves at two positions  $x_1$  and  $x_2$  are obtained from the intensities  $P_1$  and  $P_2$  of the heterodyne spectrum. Although  $u_{z0}$  may vary while translating the blade between  $x_1$  and  $x_2$ , the ratio  $P_1/P_2$  is an exponential function of  $x$ , independent of  $u_{z0}$  (see text).

$$P_2(\omega_{ind}) = B_2 |u_{z0}|^2 e^{-2\Gamma|x - x_2|} = B_2 |u_{z0}|^2 e^{-2\Gamma(x_1 + d - x)}, \quad (5.22)$$

respectively, where  $B_1$  and  $B_2$  are instrumental constants which are determined by the intensity of the incident light, that of the local oscillator, the optical alignment, the electronic gain of the detector, the data acquisition system, etc. By taking the ratio of these two intensities the factor  $|u_{z0}|^2$  drops out, yielding

$$\frac{P_1}{P_2} = \frac{B_1 e^{2\Gamma(2x_1 + d)}}{B_2} e^{-4\Gamma x} = B e^{-4\Gamma x}, \quad (5.23)$$

where

$$B = \frac{B_1 e^{2\Gamma(2x_1 + d)}}{B_2} \quad (5.24)$$

is a *constant* which is independent of the source amplitude  $u_{z_0}$ . Hence, as long as the constant  $B$  does not change, the intensity *ratio* falls off as  $e^{-4\Gamma x}$  even if the source amplitude varies.

Note that the induced capillary waves travel in opposite directions at the positions  $x_1$  and  $x_2$ . If the frequency of the local oscillator is shifted, then the scattered beams can be detected with a single detector and the spectrum will contain two separate peaks, one for each of the two positions  $x_1$  and  $x_2$ . Because of the opposite direction of propagation of the capillary waves one will be shifted up, the other shifted down (see Fig. 5.2). The intensities of these two peaks can now be obtained from a *single* spectrum and the ratio of the intensities  $P_1/P_2$  is now also independent of any drift in detection sensitivity.

In summary, the double-beam heterodyne measurement of capillary wave damping has three major advantages: 1) it does not require any deconvolution of instrumental broadening, 2) it is independent of fluctuations in source amplitude and the detector sensitivity, and 3) the measurements are automatically calibrated.

#### §5.2.4 Static light scattering measurements of spatial damping

If the spatial damping coefficient is large, the amplitude of the capillary waves falls off over a very short distance and it becomes difficult to monitor the amplitude of the waves over a distance long enough to obtain an accurate value for  $\Gamma$ . As mentioned in §5.2.2 the spatial damping coefficient can then be obtained by studying the scattered light intensity as a function of the scattering angle, instead of distance.

Let us therefore look at the power spectrum in Eq. (5.18) as a function of scattering angle

$$P(\phi) \propto \frac{1}{(q_\phi - q_{ind})^2 + \Gamma^2} = \frac{1}{k_{laser}^2 \cos^2 \theta_0 (\phi - \phi_{ind})^2 + \Gamma^2} \quad (5.25)$$

where  $q_\phi$  is the wavevector corresponding to a scattering angle  $\phi$  (see Eq. 2.51 and Fig. 2.7);  $k_{laser}$  and  $\theta_0$  are the wavevector and incidence angle of the incident probe beam, respectively. Equation (5.25) shows that the spatial profile of the scattered light is a Lorentzian centered at  $\phi_{ind}$  with a full-width at half-maximum of  $2\Gamma/k_{laser}\cos\theta_0$ . In practice the expression in Eq. (5.25) is broadened by the finite waist and divergence of the incident beam. However, this instrumental broadening function can be readily determined from the profile of the specularly reflected beam, which contains only the instrumental broadening.

When the induced wave is strong enough, one can measure the profiles of the specularly reflected and two first-order diffracted beams with a position-sensitive detector such as a CCD camera. When the scattered intensity is too weak to be detected directly, one can use a heterodyne technique to extract the scattered beam, which is frequency-shifted by an amount  $\omega_{ind}$  from the laser frequency.

Notice that this static light scattering method works best for large spatial damping, when the broadening of the spatial profile exceeds the instrumental broadening due to divergence and finite beam width. Since the heterodyne method of the previous section works best for small damping the two methods complement one another and can be used to study damping coefficients over a large range of interest.

### §5.3 Experimental

Measurements were conducted on a clean water surface and a water surface covered with a monolayer of pentadecanoic acid (PDA). The liquid sample is contained in a Teflon-coated stainless steel trough ( $30.5 \times 7.6 \times 0.5$  cm<sup>3</sup>). To prevent contamination of the liquid

surface the trough is located inside a sealed compartment. The temperature of the trough is regulated by circulating a temperature stabilized liquid through the trough and is monitored by a thermistor (ON-950, Omega) attached to the side wall of the trough. During the optical measurements, the liquid circulation is turned off so as not to disturb the liquid surface; the temperature stability during a typical 20-minute measurement is about 0.5 K. A Teflon barrier sitting on top of the trough wall is used for sweeping the water surface and controlling the surface area. The barrier is held down by a holder which can be moved across the trough by a driving mechanism consisting of a rulon nut and a stainless steel lead screw driven by a dc-motor (CTC-323-22, Micro Kinetics). The position of the barrier is recorded using a magnetic encoder (CTC-322-MI, Micro Kinetics). No lubricant is used to ease the friction between the rulon nut and the lead screw and the lifetime of the nut is rather short (a few weeks).<sup>†</sup>

For all experiments ultrapure (18-M $\Omega$ , deionized and distilled) water obtained from a Millipore Milli-Q UV system was used. The surfactant used was n-pentadecanoic acid, with a stated purity of 99+%, supplied by Aldrich Chemical Company. To prevent the pentadecanoic acid from dissolving into the water, the aqueous subphase was made acidic (pH = 2.0) using concentrated HCl (Ultrex II Ultrapure Reagent, Baker Analyzed). To spread the surfactant on the water surface, a chloroform solution of pentadecanoic acid is made using HPLC grade chloroform from Fisher Scientific (residue after evaporation < 2 ppm). A monolayer of pentadecanoic acid is formed by spreading the chloroform solution onto a clean aqueous subphase with a Hamilton 10-microliter syringe. After spreading, the chloroform is left to evaporate for at least 20 minutes, after which the compartment is pumped out to remove the chloroform vapor. After removing the chloroform, the compartment is filled with ultrapure nitrogen gas. Each time the surface concentration is

---

<sup>†</sup> A new design of the driving mechanism using an inch worm motor from Burleigh is under construction. Inch worm motors use the piezoelectric effect to move linearly along a shaft. This eliminates the need for lubrication.

changed, the system is allowed to equilibrate before optical measurements were made. Before and after each optical measurements, the surface tension of the sample is measured using a Wilhelmy plate (see below). The surface concentration of pentadecanoic acid was increased by adding surfactant onto the aqueous subphase.<sup>†</sup>

For measurements both on clean and monolayer-covered liquid surfaces, it is very important that no impurities accumulate on the surface. Before each set of measurements, the trough and barrier are first cleaned with a soap solution in an ultrasonic cleaner, rinsed with distilled water, and wiped with chloroform and acetone. Then they are placed in a bath of warm dilute chromic acid (five times diluted cleaning solution) for 30 minutes and rinsed with 18-M $\Omega$  distilled and deionized water. Clean-room compatible cotton wipers (TX309, Texwipe) are used to wipe and clean other components inside the compartment. All the translation stages are lubricated with vacuum grease (L grade, Apiezon) and sealed with plastic bags. The compartment is flushed and filled with nitrogen of ultrahigh purity (THC < 0.5 ppm) from Med Tech. To ensure a clean interface the water surface is cleaned by sweeping it with the barrier and aspirating the compressed surface with a glass pipet attached to a feedthrough on the wall of the compartment. During this cleaning process, the pressure inside the compartment is kept higher than that outside the compartment to prevent contamination from outside. When the change in surface tension under a 5:1-ratio compression or expansion of the surface area by the barrier is less than 0.05 dyne/cm, the water surface is considered to be clean.

The surface tension of the liquid is measured with a Wilhelmy plate [Gains 1977]. The plate used in our measurements is a  $1.3 \times 1.3$  cm<sup>2</sup> square of filter paper (Durapore type, Millipore). It is suspended from a Teflon-coated leaf spring and is immersed into the liquid. The force exerted on the plate by the liquid surface is proportional to the vertical displacement of the plate. This displacement is measured using a hermetically sealed linear

---

<sup>†</sup> Because of leakage across the barrier, the barrier was only used to clean the interface not for changing the surface area during a measurement.

variable displacement transducer (LVDT) suitable for use in humid conditions (HPA-50, Schaevits). The LVDT readings are averaged for 0.5 s and the force is calibrated by suspending a number of known weights from the spring and measuring the resulting displacements.

Because of the buoyancy of the submerged part of the Wilhelmy plate, the force on the spring depends on the depth of the plate in the liquid. The entire Wilhelmy plate and LVDT assembly is therefore mounted on a vertical dc-motor-driven (Encoder Mike, Oriol) translation stage. For an absolute measurement of the surface tension the stage is raised in small steps until the filter paper is just detached from the liquid surface. The surface tension is then obtained by comparing the LVDT readings just before and after the plate is detached from the surface and dividing the measured force by the perimeter of the Wilhelmy plate. The surface tension for clean water obtained in this way is within  $\pm 2\%$  of the literature value. During the damping measurements the Wilhelmy unit remained at some fixed arbitrary height to monitor relative changes in surface tension; the sensitivity for relative changes in surface tension is about 0.05 dyne/cm.

The optical setup is similar to the one described in Chapters 2 and 4. Therefore we will only mention the most important points here (see Fig. 5.2). A collimated, 10-mW multimode He-Ne laser beam (106-1, Spectra Physics) is split into two beams with a beamsplitter: 5% of the beam serves as local oscillator, while the remainder (main beam) illuminates the liquid surface. Both the main beam and the local oscillator are frequency-shifted using two acousto-optic modulators (AOM-40, IntraAction Corp.), such that the difference frequency between the two is 5 kHz. Since the optimum carrier frequency of the acousto-optic modulator crystals is 40 MHz, 20.000 MHz and 20.0025 radio-frequency signals from two Hewlett-Packard 3325-B frequency synthesizers are doubled by the combination of frequency doubler (FD-2, Mini-Circuits), high-pass filter (BHP-50, Mini-Circuits), and low-pass filter (BLP-50, Mini-Circuits). The resulting two doubled rf signals give a very sharp and stable 5 kHz frequency difference. Each of the beams is again split

into two by a 50%-beamsplitter mounted on a translation stage, making two pairs of main and local oscillator beams. The main and local oscillator beams are aligned parallel to each other and each pair is focussed by a 75-cm focal length converging lens onto a single spot on the liquid surface. The spots for each of the two pairs of beams are typically separated by a distance of 5 cm. When the frequency of the induced wave is changed the angle between the local oscillators and the main beams must be adjusted

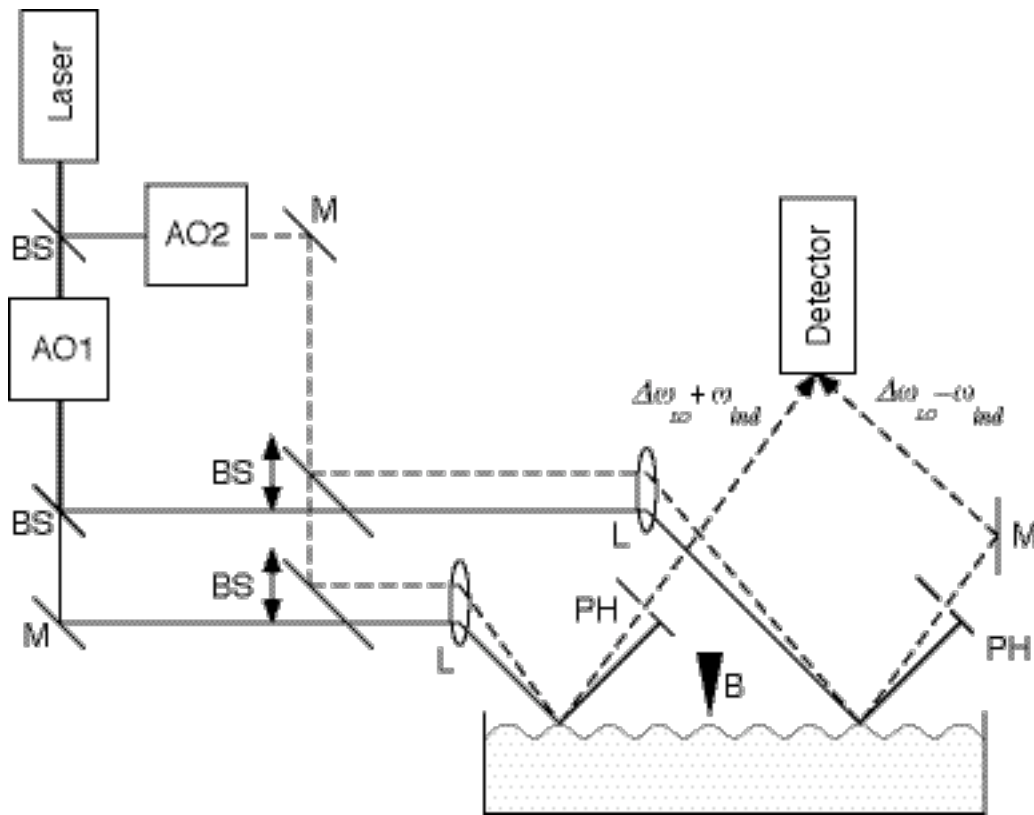


Fig. 5.2. Double-beam Fourier transform heterodyne setup for measuring the spatial damping of capillary waves. Two pairs of probing and local oscillator beams are incident on two positions at the interface separated by a distance of approximately 5 cm. Each pair employs the parallel-beam method discussed in Chapter 2. The frequency of the two local oscillator beams is shifted by  $\Delta \omega_{LO}$ . The two pairs of beams are aligned to have the same scattering angle and are detected by a single photomultiplier tube. The power spectrum of the detector beat signals is then composed of a doublet at  $\Delta \omega_{LO} \pm \omega_{ind}$ . Symbols for the optical components are the same as in Fig. 4.2.

accordingly. This angle can easily be done by adjusting the separation between main and local oscillator beams.

Plane capillary waves are induced by applying a sinusoidally varying voltage ( $\sim 100$  V) to a 7 cm-long blade edge made of stainless steel placed between the two pairs of beams and close to the liquid surface ( $< 0.5$  mm). The frequency of the oscillating voltage is the half frequency of the desired capillary wave frequency. To avoid drift of the capillary wave frequency the oscillating voltage is generated with a Hewlett-Packard 3325-B frequency synthesizer with an oven-controlled time base, which has a stability of  $\pm 5 \times 10^{-8}$ /week. The blade edge is mounted on a horizontal translation stage driven by a dc-motor (Encoder Mike, Oriol), which has  $0.1\text{-}\mu\text{m}$  resolution. The amplitude of the induced capillary wave at the position of the blade can be estimated by comparing the scattered light signal from the induced capillary waves with that from thermally excited capillary waves which an amplitude of approximately 1 nm. Typically we adjusted the amplitude to less than 100 nm, well within the regime of linearized hydrodynamics for capillary waves of  $100\ \mu\text{m}$  wavelength.

The beat signals between the scattered light and the local oscillator beams are recorded with a single photomultiplier tube. The ac component of the detector signal is amplified, and then sampled for 100 msec at a 20-kHz rate. Spectra are obtained by Fourier transforming the digitized waveform and taking the square-root of transformed points.<sup>†</sup> A typical spectrum averaged over twenty waveforms is shown in Fig. 5.3. All spectra contain an intense central<sup>‡</sup> peak caused by elastically scattered stray light, two broad side peaks due to thermally excited capillary waves, and two sharp peaks on top of the

---

<sup>†</sup> It was found that Fourier transform using integer numbers and floating point numbers made no difference for the determination of the spatial damping coefficient. To shorten the transform time, built-in software calculating the square root of the (integer) Fourier amplitude provided by the manufacturer of the interface board was used.

<sup>‡</sup> Central here means at frequency equal to the local oscillator frequency shift. Remember that the origin of the power spectrum of the interfacial fluctuations is shifted by a few kHz.

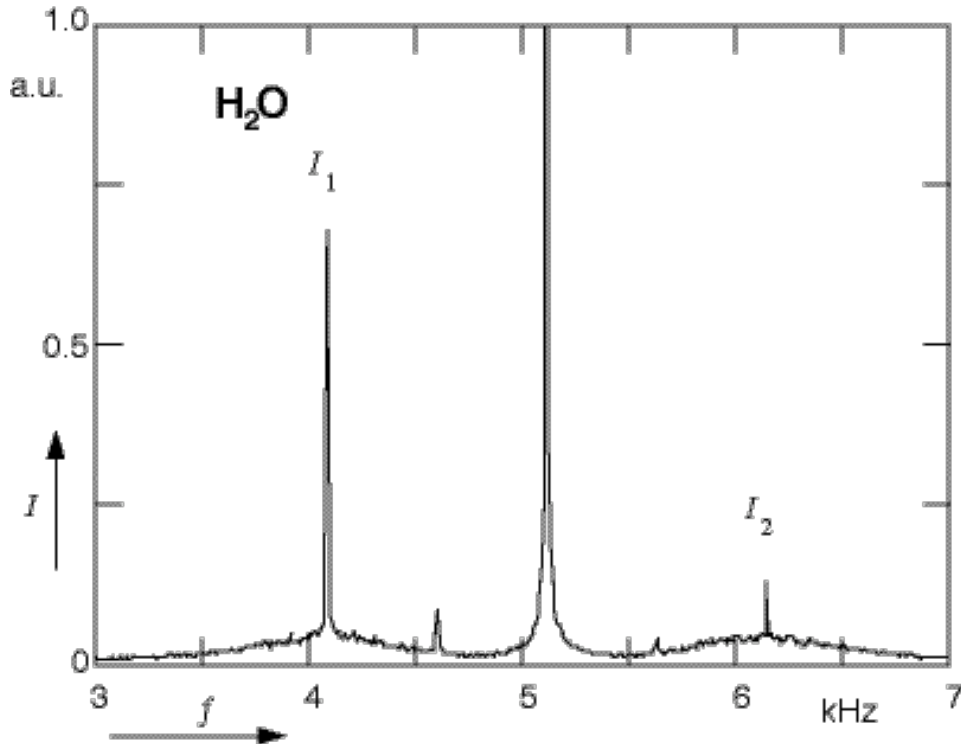


Fig. 5.3. Frequency spectrum of light scattered by induced capillary waves at a water surface. The square root of the power spectrum,  $I$ , which is proportional to the amplitude of the wave, is shown. The data shown represent the average of twenty spectra. The strong central peak near 5.1 kHz is caused by stray light. Two side peaks,  $I_1$  and  $I_2$ , are due to the induced capillary waves at the probing points  $x_1$  and  $x_2$ , respectively. Thermal capillary wave peaks are also visible under the much narrower induced peaks. Two sharp peaks halfway in between the central peak and the induced peaks are due to dc components of the electric signal used to induce the capillary waves.

thermally excited peaks due to the induced capillary waves. The ratio of the heights of the two sharp peaks changes as the blade is moved, and the spatial damping coefficient is directly obtained by measuring the exponential decay of this ratio as a function of distance, see Eq. (5.23).

## §5.4 Results and discussion

### §5.4.1 Clean water surface

To ensure proper functioning of the apparatus, this technique was first applied to

study capillary wave damping at a clean air-water interface. For such an interface the damping is completely determined by the shear viscosity of bulk water, see Eq. (5.12). We have studied capillary waves in the frequency range 500–2500 Hz, and for each frequency, we measured the exponential decay of the excited wave as a function of distance. Fig. 5.4 shows a typical decay of the wave amplitude ratio as a function of

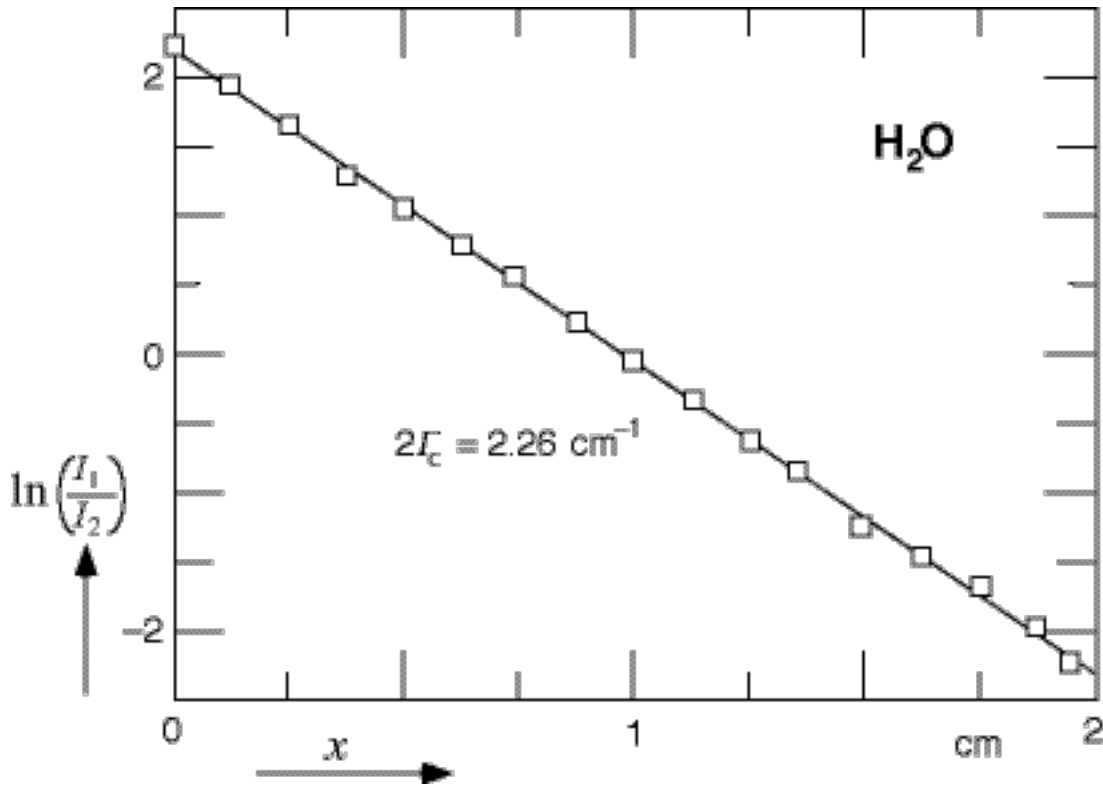


Fig. 5.4. Exponential decay of the induced capillary waves at a clean water surface. The frequency of the induced waves is 1 kHz. The temperature and surface tension are 23°C and 71.2 dyne/cm, respectively. Using this surface tension value, Eq. (5.12) yields the spatial damping coefficient of  $1.10 \text{ cm}^{-1}$ . The measured value is  $1.13 \text{ cm}^{-1}$ .

distance for a frequency of 1 kHz. Each point in this graph represents one (averaged) spectrum as in Fig. 5.3. Notice the excellent exponential decay of the wave amplitude over two orders of magnitude. The slope of the data points yields a spatial damping coefficient

of  $1.13 \text{ cm}^{-1}$  which is in excellent agreement with the theoretically expected value of  $1.10 \text{ cm}^{-1}$ .

The dependence of the spatial damping on the frequency of the induced wave is shown in Fig. 5.5.<sup>†</sup> The solid line represents the theoretically expected value for clean

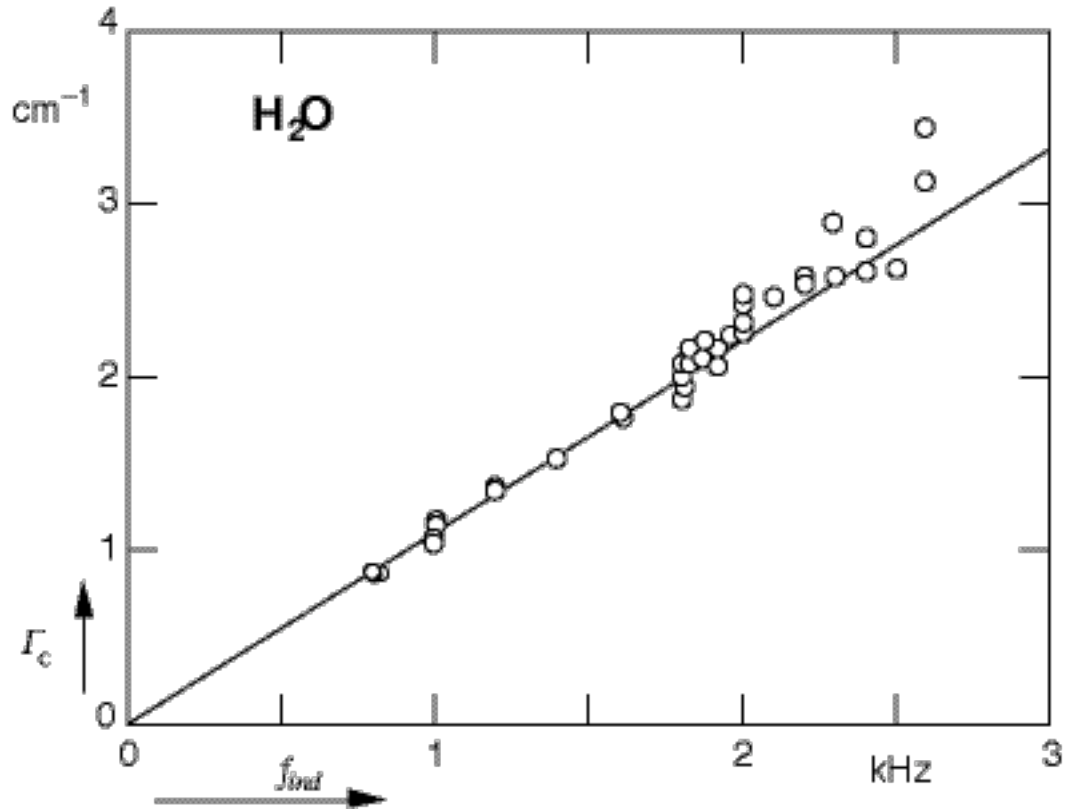


Fig. 5.5. Spatial damping coefficients as a function of frequency for a clean water surface. The circles are the measured damping coefficient, while the solid line is the theoretical value from Eq. (5.12).

water according to Eq. (5.12) using literature values for the mechanically measured static surface tension and shear viscosity of water. As can be seen the agreement is excellent for frequencies up to 2 kHz. At higher frequencies the data points exhibit greater scattering,

<sup>†</sup> Notice that each point in this graph is determined by approximately 20 exponential decay points, as in Fig. 5.4, which in turn each represent the average of 20 Fourier transforms as in Fig. 5.3. Thus, for each point in Fig. 5.5, 400 Fourier transforms of 2000 data points were taken.

most likely because of the increased damping which restricts the measurable range of distances and therefore the signal-to-noise ratio.

These results clearly demonstrate that the double-beam heterodyne spectroscopy is an excellent tool for studying surface wave attenuation. The method also has an enormous sensitivity for surface impurities. When ‘dry high purity’ nitrogen was first used as an atmosphere the spatial damping coefficient values were not reproducible and differed from the theoretical value by a factor of two to four. Agreement between experiment and theory could only be obtained when the ‘dry high purity’ nitrogen was replaced by ‘ultrahigh purity’ nitrogen.<sup>†</sup>

#### **§5.4.2 Monolayer-covered water surface**

When a monolayer of surfactant molecules such as fatty acids, which are composed of a hydrophilic polar head group and a hydrophobic hydrocarbon chain, is spread on a water surface, the monolayer displays a phase behavior similar to that of three-dimensional systems [Adamson 1982; Pallas 1983]. At low surface concentration the surfactant molecules are essentially independent and behave like a two-dimensional ideal gas. As the surface concentration of the surfactant molecule is increased, either by compressing the monolayer or by adding surfactant, the monolayer undergoes a phase transition from a ‘gaseous’ phase to a ‘liquid-expanded’ phase. This liquid-expanded phase exhibits a compressible liquid-like behavior. The average intermolecular distance of the liquid-expanded phase is still much greater than that for bulk liquids. At still higher concentration, the hydrophilic polar heads of the surfactant molecules are closely packed along the water surface and the hydrophobic chains are aligned vertically to the water surface. This third solid-like phase is called ‘liquid-condensed’ and behaves like a gel. As one continues to

---

<sup>†</sup> The increase in damping by impurities in the nitrogen may also explain the observed discrepancy of the asymmetry values in Chapter 4, since ‘dry high purity nitrogen’ was used for these measurements.

increase the surface concentration the monolayer eventually collapses.

We carried out measurements on monolayers of pentadecanoic acid on water at 23 °C at three different capillary wave frequencies (800 Hz, 1000 Hz and 1200 Hz). For each frequency we determined both the surface pressure  $\Pi$  and the spatial damping coefficient  $\Gamma$  as a function of the surface concentration of the pentadecanoic acid  $\gamma$ .

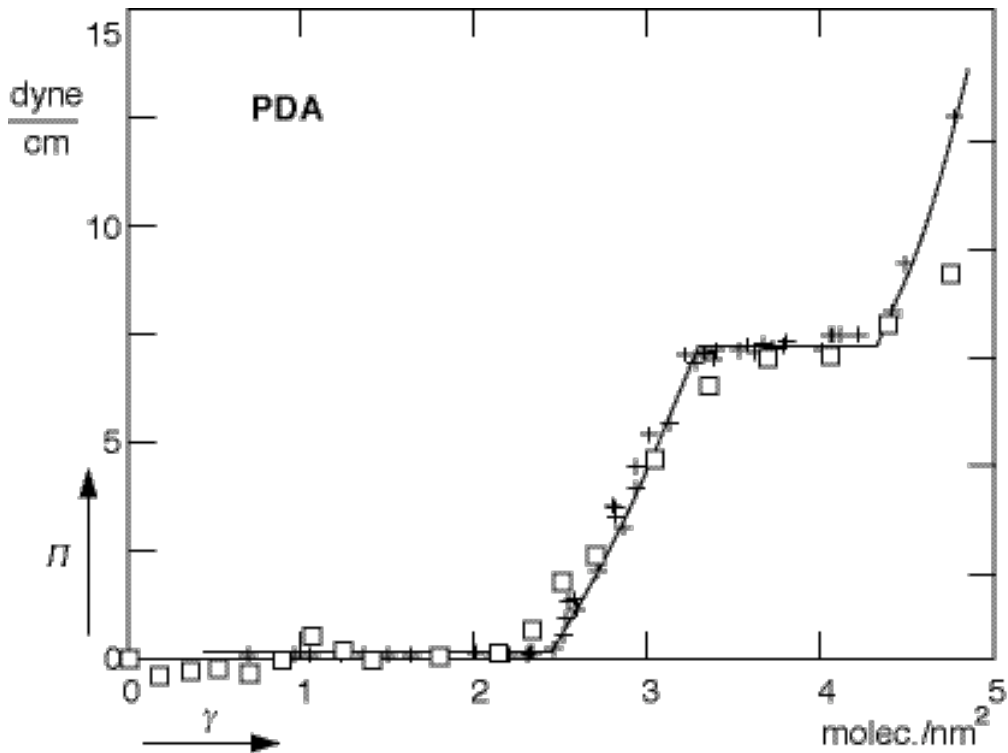


Fig. 5.6  $\Pi$ - $\gamma$  isotherm of a pentadecanoic acid monolayer at 23 °C. The squares represent the measured surface pressure; the vertical crosses, linked by the solid line, are data obtained at 25 °C [Pallas 1983]. The surface concentration was increased stepwise by adding small amounts of a chloroform solution of pentadecanoic acid.

After testing our apparatus on clean water surface, we utilized it to study the effects of surfactant monolayers on capillary wave damping. Fig. 5.6 shows the surface pressure measurements. The isotherm formed by the data points is in good agreement with

published data obtained at 25 °C [Pallas 1983]. The data show that the pentadecanoic acid monolayer undergoes a phase transition from gaseous to liquid-expanded state at a surface concentration around  $\gamma \approx 2.3$  molecules/nm<sup>2</sup>. From 3.2 to 4.3 molecules/nm<sup>2</sup> one has a coexistence between the liquid-expanded and liquid-condensed phases.

Fig. 5.7 shows the corresponding spatial damping coefficient as a function of surface concentration at a frequency of 1 kHz. Each point in this plot is determined by measuring the exponential decay of induced capillary waves as show in Fig. 5.4. At low surface concentration below 1.4 molecule/nm<sup>2</sup> the spatial damping coefficient is nearly

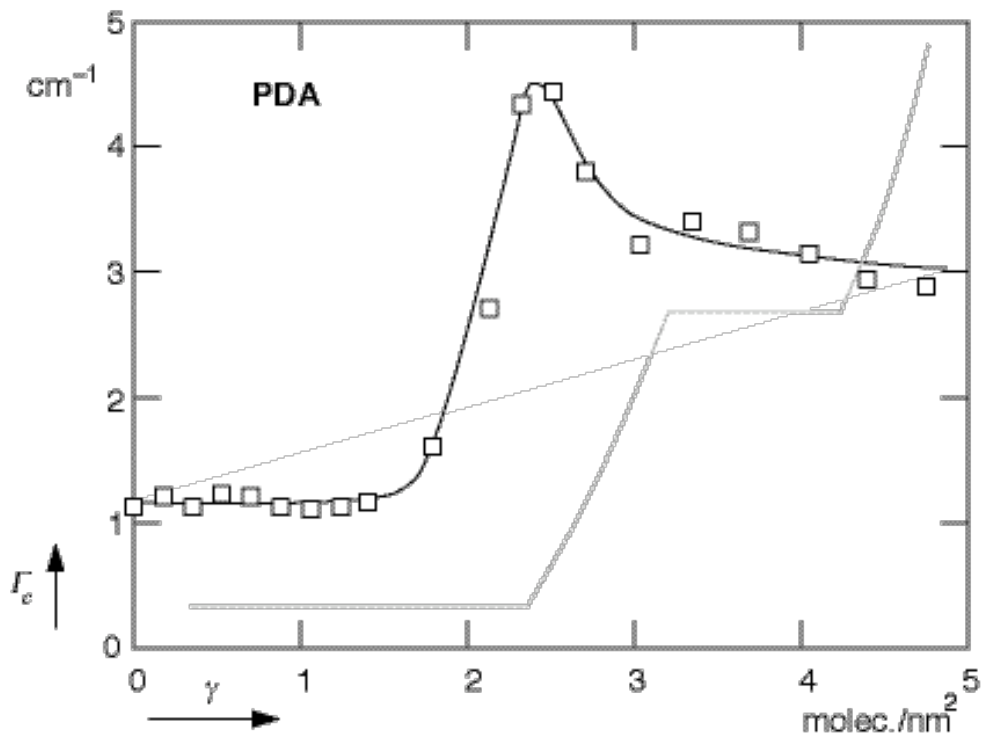


Fig. 5.7 Spatial damping of a water surface covered with a pentadecanoic acid monolayer at  $23 \pm 1^\circ\text{C}$ . The squares are the spatial damping coefficients of induced 1-kHz waves measured by the double-beam heterodyne technique. The solid line is a guide to the eye; the dotted line represents the isotherm shown in Fig. 5.6.

constant and identical to that of a pure water within the experimental error. In this region the monolayer is in the gaseous phase [Pallas 1983]. As the concentration increases to the beginning of the liquid-expanded/gaseous coexistence region ( $\gamma \approx 1.4$  molecule/nm<sup>2</sup>), the spatial damping coefficient shows a sharp increase. A maximum of the damping coefficient occurs when the surface concentration is about  $\gamma \approx 2.4$  molecules/nm<sup>2</sup>. This coincides with the point where the surface pressure begins to increase which marks the end of the coexistence region and the beginning of the homogeneous liquid-expanded phase. As the surface concentration is further increased, the damping coefficient decreases and levels out. The results obtained at capillary wave frequencies of 800 and 1200 Hz exhibit the same behavior, with a maximum at a surface concentration of 2.4 molecules/nm<sup>2</sup>.

A maximum in the damping of capillary waves at a monolayer-covered water surface was predicted by Dorrestein [Dorrestein 1951] and observed [Hansen and Mann 1964]. For pentadecanoic acid a maximum in the temporal damping of capillary waves at the same point in the isotherm has been reported previously [Chen, Sano *et al.* 1986]. Neglecting the dilational surface viscosity  $\kappa$  one obtains the following expression for the spatial damping coefficient, see Eqs. (5.4) and Eq. (5.14),

$$\Gamma = \frac{\omega_c}{v_g} \frac{1 - \xi_0 \theta^{-1/2} + \frac{1}{2} \xi_0^2 \theta^{-3/2}}{1 - 2\xi_0 \theta^{-1/2} + 2\xi_0^2 \theta^{-1}}, \quad (5.26)$$

where  $\xi_0 (= \mathcal{E}_0/\sigma_0)$  is the real part of  $\xi$ . This expression has a maximum when  $\xi_0 \approx \frac{1}{2} \theta$ , for  $\theta \ll 1$ . Thus a maximum in spatial damping should occur when

$$\mathcal{E}_0 \approx \eta \sqrt{\frac{\sigma_0 q_{ind}}{\rho}}. \quad (5.27)$$

Note that  $\mathcal{E}_0$  is the real part of the total dilational modulus  $\mathcal{E}$  which is the sum of the lateral compression modulus  $K$ , the lateral shear modulus  $G$ , and the dilational modulus  $\mathcal{E}_\sigma$ , see Eq. (3.49). If  $K$  and  $G$  are neglected,  $\mathcal{E}_0$  is equal to the real part of  $\mathcal{E}_\sigma$ , see Eq. (3.56). The physical interpretation of this maximum was given by Lucassen and coworkers as a

coupling between the transverse capillary waves and longitudinal waves [Lucassen-Reynders and Lucassen 1969].

The observed maximum in our data, however, cannot correspond to the maximum predicted by Dorrestein. In the gas/liquid-expanded coexistence region the surface pressure remains constant, so according to Eq. (3.41) the real part of  $\mathcal{E}_\sigma$  must be zero when the maximum occurs. If  $\mathcal{E}_\sigma$  is zero, then  $\xi_0 = 0$  and Eq. (5.26) yields a constant value for the damping. Clearly, Dorrestein's analysis with only two real viscoelastic surface parameters, a real dilational modulus  $\mathcal{E}_\sigma$  and a surface tension  $\sigma_0$ , cannot adequately describe the observed behavior of the spatial damping coefficient.

To explain the behavior of the observed damping coefficient, let us assume that the monolayer in the coexistence region is composed of 'mesoscopic' domains of the gaseous and liquid-expanded phases.<sup>†</sup> Let the damping in the gaseous phase domain be  $\Gamma_G$ , that in the liquid-expanded phase domain  $\Gamma_{LE}$ . In the coexistence region, net damping coefficient is then given by

$$\Gamma(X) = (1 - X) \Gamma_G + X \Gamma_{LE} = \Gamma_G + X (\Gamma_{LE} - \Gamma_G), \quad (5.28)$$

where  $X$  is the fraction of the monolayer in the liquid-expanded phase. The dotted line in Fig. 5.8 shows the linear increase in capillary wave damping in the coexistence region based on Eq. (5.28). From the data it is clear that additional damping occurs near the high concentration end of the coexistence region.

Let us propose a very simple model to explain the location of the maximum. Enhanced damping of interfacial waves could occur if the wave motion were to drive the monolayer domains in the liquid-expanded phase back and forth across the phase transition, a process which requires energy. Corrugation of the interface due to the wave motion increases the surface area and therefore reduces the surface concentration. In the

---

<sup>†</sup> Fluorescent microscopy experiments have shown that monolayers of myristic acid in liquid-condensed/liquid-expanded coexistence region are composed of mesoscopic domains of liquid-condensed phase surrounded by liquid-expanded phase [Suresh, Nittmann *et al.* 1988].

coexistence region this could cause a phase transition of (some of) the liquid-expanded phase domains into the gaseous phase. One expects this effect to be most pronounced at the high surface concentration end of the coexistence region where the liquid-expanded regions are largest. This is so because if the dimension of the liquid-expanded domains is much smaller than the wavelength, the wave motion causes an expansion of the gaseous phase domain (without phase transition) because of the much smaller dilational modulus of the gaseous phase. As the concentration is increased beyond the high end of the coexistence region the spatial damping coefficient returns to the value of the liquid-expanded phase. Based on this mechanism a maximum in damping occurs at the lowest concentration for which the entire surface area is covered by the liquid-expanded phase, since changes in area have the largest effect there. The solid line in Fig. 5.8 schematically illustrates the effect of adding such damping due to phase transitions to the damping in Eq. (5.28).

In this model the detailed shape of the maximum would depend on amplitude and frequency of the capillary waves. Further measurements to verify the behavior of the maximum in damping as a function of capillary wave amplitude and frequency are called for. One would also expect a second maximum near the high concentration end of the coexistence region between the liquid-expanded and liquid-condensed phases. While our measurements do not show a second maximum, measurements on the temporal damping of capillary waves on a poly(vinyl acetate) film on a water surface show two maxima, both near phase transitions [Langevin 1981; Kawaguchi, Sano *et al.* 1986]. In the case of the poly(vinyl acetate) film the phase transitions are second order (the slope in the  $\Pi$ - $\gamma$  isotherm changes without a coexistence region) but the arguments for extra damping provided above still hold near a second order phase transition. This suggests that damping measurements

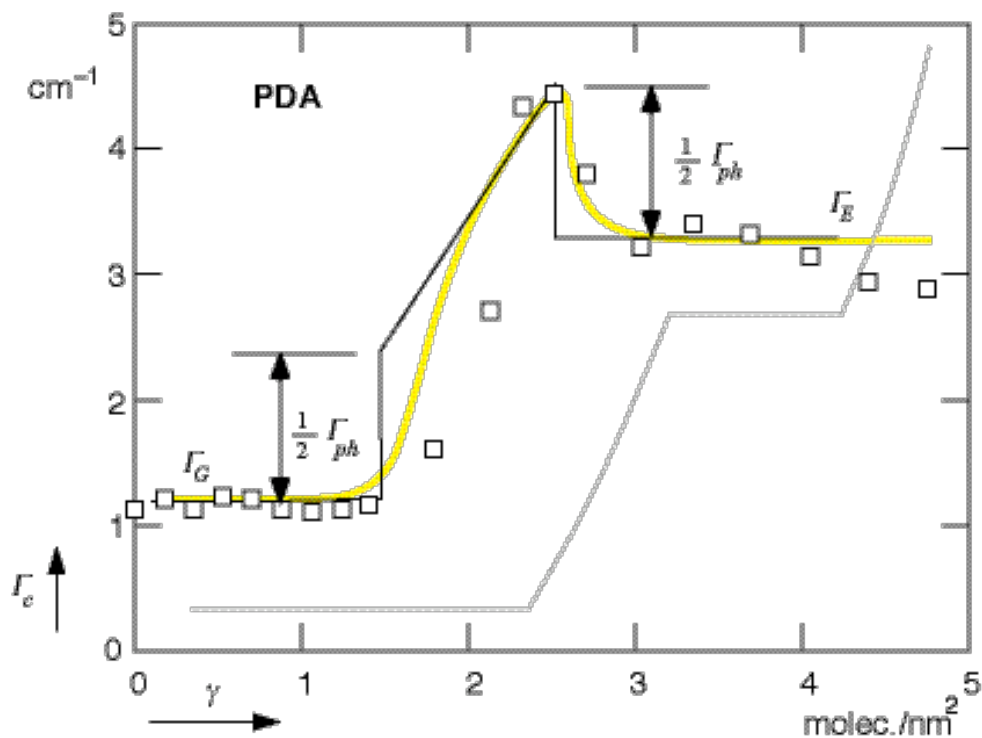


Fig. 5.8 Simple model for damping of capillary waves. The dotted line represents Eq. (5.28) which increases from  $\Gamma_G$  to  $\Gamma_{LE}$  linearly. The enhanced damping due to the phase transition mechanism is illustrated by the solid line. The shaded line is the isotherm in Fig. 5.6.

are a sensitive tool for locating the phase transitions of a monolayer.

In summary, we have carried out direct measurements of the spatial damping coefficient of capillary waves. The measurements require no deconvolution or calibration. The coefficients obtained for a clean water surface at different frequencies are in good agreement with theory. When a monolayer of pentadecanoic acid is spread on a water surface, a maximum in spatial damping is observed at the high surface concentration end of the liquid-expanded/gaseous coexistence region. The occurrence and the position of the maximum can be explained by a simple model in which additional dissipation occurs when the wave motion drives the monolayer across a phase transition.

## Bibliography

- Adamson, A. W. (1982). *Physical Chemistry of Surfaces* (4 ed.), John Wiley & Sons, New York.
- Armstrong, B. H. (1967). *J. Quant. Spectrosc. Radiat. Transfer*, **7**, 61.
- Asch, R. and Ford, N. C. (1973). *Rev. Sci. Instrum.*, **44**, 506.
- Balescu, R. (1975). *Equilibrium and Nonequilibrium Statistical Mechanics*, John Wiley and Sons, New York.
- Bedeaux, D. and Oppenheim, I. (1978). *Physica*, **90A**, 39.
- Bellman, R. E. and Pennington, R. H. (1954). *Quart. Appl. Math.*, **12**, 151.
- Benedek, G. B. (1968). In M. Chrétien, S. Deser and E. P. Gross (Eds.), *Statistical Physics, Phase Transition and Superfluidity* (p. 1), Gordon and Breach Science Publishers, New York.
- Berne, B. J. and Pecora, R. (1976). *Dynamic Light Scattering with Applications to Chemistry, Biology and Physics*, Wiley, New York.
- Beysens, D., Garrabos, Y. and Zakczer, G. (1980). *Phys. Rev. Lett.*, **45**, 403.
- Bland, D. R. (1960). *The Theory of Linear Viscoelasticity*, Pergamon, Oxford.
- Born, M. and Wolf, E. (1975). *Principles of Optics* (5 ed.), Pergamon, Oxford.
- Bouchiat, M. A. and Meunier, J. (1968). *C. R. Acad. Sci. (Paris) B*, **266**, 301.
- Bouchiat, M. A., Meunier, J. and Brossel, J. (1968). *C. R. Acad. Sci. (Paris) B*, **266**, 255.
- Bouchiat, M. A. and Meunier, J. (1971a). *J. Physique*, **32**, 561-571.
- Bouchiat, M. A. and Meunier, J. (1971b). *J. Physique*, **33**, c1-141.
- Bouchiat, M. A. and Langevin, D. (1978). *J. Colloid Interface Sci.*, **63**, 193.
- Bracewell, R. N. (1965). *The Fourier Transform and Its Applications*, McGraw-Hill, New York.

- Bracewell, R. N. (1986). *The Hartley Transform*, Oxford University Press, New York.
- Brown, J. C. (1983). *Am. J. Phys.*, **51**, 1008.
- Buff, F. P. (1952). *Z. Electrochem.*, **56**, 311.
- Byrne, D. and Earnshaw, J. C. (1979). *J. Phys. D*, **12**, 1145.
- Chen, Y.-L., Sano, M., Kawaguchi, M., Yu, H. and Zograf, G. (1986). *Langmuir*, **2**, 349.
- Chen, Y.-L., Kawaguchi, M., Yu, H. and Zograf, G. (1987). *Langmuir*, **3**, 31.
- Chu, B. (1974). *Laser Light Scattering*, Academic Press, New York.
- Chung, D. S., Lee, K. Y. C. and Mazur, E. (1988). *Int. J. Thermophysics*, **9**, 729.
- Chung, D. S., Lee, K. Y. and Mazur, E. (1990). *Phys. Lett.*, **A145**, 348.
- Cottam, M. G. and Maradudin, A. A. (1984). In V. M. Agranovich and R. Loudon (Eds.), *Surface Excitations* (p.1), North-Holland, Amsterdam.
- Cummins, H. Z., Knable, N. and Yeh, Y. (1964). *Phys. Rev. Lett.*, **12**, 150.
- Cummins, H. Z. and Swinney, H. L. (1970). *Prog. Opt.*, **8**, 133.
- Davies, J. T. and Vose, R. W. (1965). *Proc. Roy. Soc. A*, **286**, 218.
- Demtröder, W. (1982). *Laser Spectroscopy*, Springer-Verlag, Berlin.
- Desai, R. and Grant, M. (1986). In C. A. Croxton (Ed.), *Fluid Interfacial Phenomena* (p. 135), John Wiley and Sons, New York.
- Dorrestein, R. (1951). *Pro. Acad. Sci. Amst. B*, **54**, 260. 350.
- Earnshaw, J. C. (1983). *Thin Solid Films*, **99**, 189.
- Earnshaw, J. C. and R. C. McGivern. (1987). *J. Phys. D*, **20**, 82.
- Earnshaw, J. C., McGivern, R. C. and Winch, P. J. (1988). *J. Phys. France*, **49**, 1271.
- Earnshaw, J. C., McGivern, R. C., McLaughlin, A. C. and Winch, P. J. (1990). *Langmuir*, **6**, 649.
- Ferry, J. D. (1961). *Viscoelastic Properties of Polymers*, Wiley, New York.
- Ford, N. C. and Benedek, G. B. (1965). *Phys. Rev. Lett.*, **15**, 649.

- Forrester, A. T., Gudmundsen, R. A. and Johnson, P. O. (1955). *Phys. Rev.*, **99**, 1691.
- Forrester, A. T. (1961). *J. Opt. Soc. Am.*, **51**, 253.
- Fox, R. F. (1982). *J. Phys. Chem.*, **86**, 2812.
- Franklin, B. (1774). *Philos. Trans. R. Soc. London*, **64**, 445.
- Gains, G. L. (1966). *Insoluble Monolayers at Liquid-Gas Interfaces*, Interscience Publishers, New York.
- Gains, G. L. (1977). *J. Colloid Interface Sci.*, **62**, 191.
- Goodrich, F. C. (1961). *Proc. Roy. Soc. Ser. A*, **260**, 481, 490, 503.
- Goodrich, F. C. (1962). *J. Phys. Chem.*, **66**, 1858.
- Grant, M. and Desai, R. (1983). *Phys. Rev.*, **A27**, 2577.
- Groot, S. R. d. and Mazur, P. (1984). *Nonequilibrium Thermodynamics*, Dover, New York.
- Hansen, R. S. and Mann, J. A. (1964). *J. Appl. Phys.*, **35**, 152.
- Hård, S., Hamnerius, Y. and Nilsson, O. (1976). *J. Appl. Phys.*, **47**, 2433.
- Herpin, J. C. and Meunier, J. (1974). *J. Physique*, **35**, 847.
- Jackson, J. D. (1975). *Classical Electrodynamics* (2 ed.), John Wiley & Sons, New York.
- Jacobs, S. F. (1988). *Am. J. Phys.*, **56**, 235.
- John, M. S., Dahler, J. S. and Desai, R. C. (1981). *Adv. Chem. Phys.*, **46**, 279.
- Katyl, R. H. and Ingard, K. U. (1967). *Phys. Rev. Lett.*, **19**, 64.
- Katyl, R. H. and Ingard, K. U. (1968). *Phys. Rev. Lett.*, **20**, 248.
- Kelvin, Lord (1871). *Philos. Mag. Ser. 4*, **42**, 362.
- Kieft, H., Clouter, M. J. and Penny, R. (1984). *Phys. Rev.*, **B390**, 4017.
- Kirkpatrick, T. R., Cohen, E. D. G. and Dorman, J. R. (1982). *Phys. Rev.*, **A26**, 950, 972, 995.
- Kirkwood, J. G. and Buff, F. P. (1949). *J. Chem. Phys.*, **17**, 338.

- Kramer, L. (1971). *J. Chem. Phys.*, **55**, 2097.
- Lamb, H. (1932). *Hydrodynamics* (6 ed.), Dover, New York.
- Landau, L. D. and Lifshitz, E. M. (1959). *Fluid Mechanics*, Addison-Wesley, Reading, MA.
- Landau, L. D. and Lifshitz, E. M. (1986). *Theory of Elasticity* (3 ed.), Pergamon, Oxford.
- Langevin, D. and Bouchiat, M. A. (1971). *C.R. Acad. Sci. Paris Ser. B*, **272**, 1422.
- Langevin, D. (1974). *J. Chem. Soc. Faraday Trans. 1*, **70**, 95.
- Langevin, D. and Greismar, C. (1980). *J. Phys. D*, **13**, 1189.
- Langevin, D. (1981). *J. Colloid Interface Sci.*, **80**, 412.
- Langevin, D., Meunier, J. and Chatenay, D. (1982). In *Surfactants in Solution* (p. 1991), Plenum Press,
- Langevin, D. (1986). *Colloids Surf.*, **21**, 313.
- Lastovka, J. B. and Benedek, G. B. (1966). *Phys. Rev. Lett.*, **17**, 1039.
- Law, B. M., Gammon, R. W. and Sengers, J. V. (1988). *Phys. Rev. Lett.*, **60**, 1554.
- Lee, J. K., Barker, J. A. and Ponnudurai, G. M. (1974). *J. Chem. Phys.*, **60**, 1976.
- Lee, K. Y., Chung, D. S., Rno, S. and Mazur, E. (1989). In *Laser Materials and Laser Spectroscopy* (p. 316), World Scientific, New York.
- Lemonick, M. D. (1986). *Time*, **128**, 94.
- Levich, V. G. (1962). *Physicochemical Hydrodynamics*, Prentice-Hall, Englewood Cliffs, NJ.
- Lifshitz, E. M. and Pitaevskii, L. P. (1980). *Statistical Physics Part 2*, Pergamon, Oxford.
- Loudon, R. (1984). In V. M. Agranovich and R. Loudon (Eds.), *Surface Excitations* (p. 589), North-Holland, Amsterdam.
- Lu, G. (1989). PhD Thesis, Harvard University.
- Lucassen, J. (1981). In E. H. Lucassen-Reynders (Ed.), *Anionic Surfactants* (p. 217), Marcel Dekker, New York.

- Lucassen-Reynders, E. H. and Lucassen, J. (1969). *Advan. Colloid Interface Sci.*, **2**, 347.
- Lucassen-Reynders, E. H. (1981). In E. H. Lucassen-Reynders (Ed.), *Anionic Surfactants* (p. 173), Marcel Dekker, New York.
- Mandel, L. (1963). *Prog. Opt.*, **2**, 181.
- Mandelstam, L. I. (1913). *Ann. Phys. (Lpz.)*, **41**, 609.
- Mann, J. A. and Hansen, R. S. (1963). *J. Colloid Sci.*, **18**, 757.
- Mayer, E. (1969). Ph.D. Thesis, University of Delaware.
- Mayer, E. and Eliassen, J. D. (1971). *J. Colloid Interface Sci.*, **37**(1), 228.
- Mazur, E. and Chung, D. S. (1987). *Physica*, **147A**, 387.
- Mazur, E., Chung, D. S. and Lee, K. Y. (1989). In M. Feld, A. Mooradian and J. Thomas (Eds.), *Laser Spectroscopy IX* (p. 216), Academic Press, Cambridge.
- Nelson, D. (1985). unpublished review.
- Newman, S. B. and Lee, W. M. (1958). *Rev. Sci. Instrum.*, **29**, 785.
- Olson, G. L. and Roth, J. A. (1988). *Mat. Sci. Reprints*, **3**, 1.
- Pallas, N. R. (1983). Ph.D. Thesis, Clarkson College of Technology.
- Physics Today*, (1984). **37**, entire volume.
- Pike, E. R. and Jakeman, E. (1974). *Adv. Quant. Elect.*, **2**, 1.
- Pouchelon, A., Meunier, J., Langevin, D., Chatenay, D. and Cazabat, A. M. (1980). *Chem. Phys. Lett.*, **76**, 277.
- Pouchelon, A., Meunier, J., Langevin, D. and Cazabat, A. M. (1980). *J. Physique Lett.*, **41**, L239.
- Rayleigh, Lord (1890). *Proc. Roy. Soc., London*. **47**, 364.
- Ronis, D., Procaccia, I. and Oppenheim, I. (1979). *Phys. Rev.*, **A19**, 1324.
- Ronis, D. and Putterman, S. (1980). *Phys. Rev.*, **A22**, 773.
- Rowlinson, J. S. (1979). *J. Stat. Phys.*, **20**, 197.

- Rowlinson, J. S. and Widom, B. (1982). *Molecular Theory of Capillarity*, Clarendon Press, Oxford.
- Satten, S. and Ronis, D. (1982). *Phys. Rev.*, **A26**, 940.
- Schwartz, D. K., Schlossman, M. L., Kawamoto, E. H., Kellog, G. J. and Pershen, P. S. (1990). *Phys. Rev.*, **A41**, 5687.
- Scott, J. C. (1978). In A. R. Hall and N. Smith (Ed.), *History of Technology* (p. 163), Mansell, London.
- Shih, L. B. (1984). *Rev. Sci. Instrum.*, **55**, 716.
- Sneddon, I. N. and Berry, D. S. (1958). In *Handbuch der Physik* Vol. 6 (p. 1), Springer-Verlag, Berlin.
- Sohl, C. H., Miyano, K. and Ketterson, J. B. (1978). *Rev. Sci. Instrum.*, **49**, 1464.
- Sohl, C. H. and Miyano, K. (1979). *Phys. Rev.*, **A20**, 616.
- Stenvot, C. and Langevin, D. (1988). *Langmuir*, **4**, 1179.
- Stokes, G. G. (1847). *Cambridge Trans.*, **8**, 37.
- Stone, J. A. (1973). M. Ch. E. Thesis, Villanova University,
- Stone, J. A. and Rice, W. J. (1977). *J. Colloid Interface Sci.*, **61**, 160.
- Suresh, K. A., J. Nittmann and F. Rondelez. (1988). *Europhys. Lett.* **6**, 437.
- Tabor, D. (1980). *J. Colloid Interface Sci.*, **75**, 240.
- Thominet, V., Stenvot, C. and Langevin, D. (1988). *J. Colloid Interface Sci.*, **126**, 54.
- Tiersten, H. F. (1969). *J. Appl. Phys.*, **40**, 770.
- Tremblay, A.-M. S., Arai, M. and Siggia, E. D. (1981). *Phys. Rev.*, **A23**, 1451.
- van der Waals, J. D. (1893). *Verhandel. Konink. Akad. Wetten. Amsterdam (Sect. 1)*, **1**, 56.
- van der Zwan, G., Bedeaux, D. and Mazur, P. (1981). *Physica*, **107A**, 491.
- Velasco, R. and García-Moliner, F. (1979). *Phys. Scripta*, **20**, 111.
- Vrij, A. (1968). *Advan. Colloid Interface Sci.*, **2**, 39.

Wu, E. S. and Webb, W. W. (1973). *Phys. Rev.*, **A8**, 2077.

Yariv, A. (1989). *Quantum Electronics* (3 ed.), John Wiley and Sons, New York.

Yeh, Y. and Cummins, H. Z. (1964). *Appl. Phys. Lett.*, **4**, 176.